8306723

Liaw, Yueh-ping

THE EFFECTS OF CHANNEL TORTUOSITY ON ELECTROMAGNETIC RADIATIONS FROM LIGHTNING RETURN STROKES

The University of Oklahoma PH.D. 1982

University
Microfilms
International 300 N. Zeeb Road, Ann Arbor, MI 48106

THE UNIVERSITY OF OKLAHOMA

GRADUATE COLLEGE

THE EFFECTS OF CHANNEL TORTUOSITY ON ELECTROMAGNETIC RADIATIONS FROM LIGHTNING RETURN STROKES

A DISSERTATION

SUBMITTED TO THE GRADUATE FACULTY

in partial fulfillment of the requirements for the

degree of

DOCTOR OF PHILOSOPHY

BY

YUEH-PING LIAW

Norman, Oklahoma

1982

THE EFFECTS OF CHANNEL TORTUOSITY ON ELECTROMAGNETIC RADIATIONS FROM LIGHTNING RETURN STROKES

APPROVED BY

W. David Rust

David Brasel

DISSERTATION COMMITTEE

ACKNOWLEDGEMENTS

Many people and several institutions have given me support and assistance during the course of this research. I am very grateful to the members of my supervisory committee for their helpful suggestions and encouragement. In particular, I would like to express my sincerest appreciation to Dr. David Rust for his continuing support, unusual patience, and overall guidance; many hours of telephone conversations plus seemingly endless shuttle mails have finally made this dissertation a reality. Special thanks are due to Dr. Richard Fowler for his kind assistance and intellectual inspiration during the initial stage of this research. I am deeply indebted to Dr. William Beasley and Dr. Martin Uman of the University of Florida Lightning Research Laboratory for providing their data and indispensable assistance during the final, crucial stage of this study. Most of the computer work was performed at the Argonne National Laboratory with technical assistance rendered by my husband, Dr. J. R. Liaw. Computer time at ANL was made possible by Dr. Marvin Wesely of the Atmospheric Physics Section through a guest thesis appointment. Discussions with Dr. Paul Krehbiel of New Mexico Institute of Mining and Technology about the fast antenna system were most useful; the slow and fast antennas were borrowed from Dr. Marx Brook of NMIMT. The acoustic system and data digitization facilities were provided by Dr. Arthur Few of Rice University. Dr. Donald

MacGorman of the National Severe Storms Laboratory guided me through the acoustic ray tracing technique for channel reconstruction. I also appreciate the help in data reduction provided by fellow students: Malcolm MacNiven, Launa Maier, David Gaede, Kevin Cameron, and Douglas Mach. Editorial assistance from Dr. Richard Guzman of North Central College, the excellent typing work of Mary Lou Vanderwall, and the drafting by Joan Kimpel are also appreciated. This research has been supported in part by the National Severe Storms Laboratory/NOAA, the Severe Storms and Local Weather Research Office of NASA, the Atmospheric Science Program of the National Science Foundation, and the Division of Educational Programs of ANL.

ABSTRACT

The analysis of radiations from a lightning return stroke requires both its channel geometry and the current waveform that propagates along the channel. Due to the lack of simultaneous measurements on lightning channel geometry and radiated waveforms, analysis and interpretation in the past have been performed mostly with simplified channel geometries such as a linear vertical channel. Although the impacts of channel tortuosity on radiated waveforms have been addressed in a few simulation studies, such exercises remain as gedanken experiments lacking real field data to support their assertions.

The main objective of this research has been to gain insight into the effects of channel tortuosity on the radiated electric field waveforms. Both theoretical investigations and experimental observations were conducted. In the theoretical part, an algorithm has been developed for solving numerically Maxwell's equations applicable to lightning return strokes. This algorithm was implemented in a computer code called EMFIELD. Extensive testing and validation of this code were performed by comparing results with existing solutions in the literature. A study was then conducted to gain basic understanding of the impacts of channel tortuosity on calculated electric field waveforms using artificial channel geometries and two different return stroke current models.

In the experimental part, two independent sources of data were used for analysis. The first set of data was obtained at the National Severe Storms Laboratory where channel geometries of two lightning flashes were reconstructed from acoustic data. The second set was supplied by the Lightning Research Laboratory of the University of Florida where channel geometries of two lightning flashes were reconstructed from two-station photographs. It was found that the greatest advantage of two-station photography is its ability to provide fine structure in the channel geometry outside the cloud; while the acoustic ray tracing technique has the advantage of providing channel structure within the cloud but does not contain fine details. Electric field changes associated with these lightning flashes were analyzed using the EMFIELD code and the reconstructed channels with the modified current model of Lin et al. By comparison of the calculated and measured electric field waveforms for reconstructed tortuous and equivalent linear channels, the impacts of channel tortuosity are observed.

From both theoretical investigations and experimental observations, it is concluded that the magnitude of the effect due to tortuosity is highly dependent upon the current model and the range to the lightning flash. Even though the current waveform is simple and smooth in the compound exponential transmission line model, the calculated electric field reflects clearly the tortuosity of the channel. On the contrary, the effect of channel tortuosity is smaller when the more complex model of Lin et al. is used. Even in this case, however, the impact is still quite significant, especially at large ranges and if the tortuosity occurs in the lower portion of the channel.

TABLE OF CONTENTS

		Page
ACKNOWLEDGEMENTS		iii
ABSTRACT		v
LIST OF TABLES		x
LIST OF ILLUSTRATIONS		xi
CHAPTER		
I.	INTRODUCTION	1
	1.1 Historical Survey	1
	1.2 Lightning Phenomena	2
	1.3 Recent Studies of Return Stroke Models	7
	1.4 Scope of This Research	10
II.	INSTRUMENTATION AND DATA PROCESSING	15
	2.1 Acoustic System and Channel Reconstruction	15
	2.1.1 Experimental Setup	15
	2.1.2 Lightning Channel Reconstruction	19
	2.2 Measurements of Lightning Electric Field Changes	27
III.	THEORETICAL ANALYSIS OF ELECTROMAGNETIC FIELD CHANGES DURING LIGHTNING RETURN STROKES	32
	3.1 Maxwell's Equations and Lightning Return Strokes	32
	3.2 Mathematical Algorithm and Numerical Solutions	33
	3.2.1 Vector Potential	35
	3.2.2 Magnetic Field	38
	3.2.3 Scalar Potential	40
	3.2.4 Electric Field	42

TABLE OF CONTENTS (Cont'd.)

		Page
	3.3 Computer Code Development and Verification	43
	3.3.1 Numerical Stability and Solution Accuracy . .	44
	3.3.2 Benchmark Problems Set 1: LeVine and Meneghini	51
	3.3.3 Benchmark Problem Set 2: Master et al. . . .	53
IV.	EFFECTS OF CHANNEL TORTUOSITY ON THE CALCULATED ELECTRIC FIELD DURING RETURN STROKES	62
	4.1 Introduction	62
	4.2 Designs of Simple Channel Tortuosity	64
	4.3 Results	68
	4.3.1 Compound Exponential Transmission Line Model	68
	4.3.2 Modified Return Stroke Model of Lin et al. .	73
	4.4 Study Using Complex Channel Geometry	79
	4.5 Conclusions	83
V.	COMPARISON OF CALCULATED VERSUS MEASURED ELECTRIC FIELD CHANGES USING RECONSTRUCTED CHANNEL GEOMETRIES	85
	5.1 Introduction	85
	5.2 Analysis of University of Florida Data	86
	5.2.1 Channel Reconstruction from Two-Station TV Data	86
	5.2.2 Comparison of Measured and Calculated Electric Fields	94
	5.3 Analysis of NSSL Data	99
	5.3.1 Antenna Circuit Response to an Electric Field Change	99
	5.3.2 Comparison of Measured and Calculated Electric Fields	102
	5.4 Calculated Return Stroke Charge Transfer	112
VI.	CONCLUSIONS AND RECOMMENDATIONS	116
	6.1 Conclusions	116
	6.2 Recommendations for Future Research	119
REFERENCES	. . . .	121

TABLE OF CONTENTS (Cont'd.)

Page

APPENDICES

I. RAY TRACING METHODOLOGY 125

IIA. THE LISTING OF EMFIELD CODE 129

IIB. IBM JCL AND SAMPLE INPUT 148

IIC. FLOW CHART OF EMFIELD 150

LIST OF TABLES

Table		Page
2.1	Five Selected Storms with Thunder Data Digitized at Rice University	21
2.2	Sixteen Multistroke Cloud-to-Ground Flashes with Matching Thunder Signals	22
2.3	The Model Atmosphere Used in Ray Tracing Analysis for June 8, 1979	24
4.1	Coordinates of the 17 Simple Tortuous Channels	65
4.2	Calculated Times and Associated Parameters for 17 Channel Geometries Using Compound Exponential Transmission Line Model	74
4.3	Calculated Times and Associated Parameters for 17 Channel Geometries Using Modified Model of Lin et al. . .	80
5.1	Measured Azimuth Angles, Distances from Electric Field Sensor, and the Reconstructed Channel Coordinates for Flash GNV1	92
5.2	Measured Azimuth Angles, Distances from Electric Field Sensor, and the Reconstructed Channel Coordinates for Flash GNV2	93
5.3	Calculated Charge Transferred by Return Strokes	114

LIST OF ILLUSTRATIONS

Figure		Page
1.1	The luminous features of a cloud-to-ground lightning flash	6
1.2	Block diagram of the research plan	13
2.1	Locations of the microphone array and the electric field sensors	17
2.2	Schematic diagram of the thunder data recording system	18
2.3	Channel geometry reconstructed from acoustic data for NSSL flash 9	25
2.4	Channel geometry reconstructed from acoustic data for NSSL flash 10	26
2.5	Schematic diagram of the electric field sensor and the associated measurement system	28
2.6	Slow antenna output for NSSL flash 9	30
2.7	Slow antenna output for NSSL flash 10	31
3.1	Depiction of a lightning return stroke and its image	34
3.2	Six neighboring points around the field point	39
3.3	The compound exponential current waveform for benchmark problem set 1	46
3.4	Calculated radiation waveforms with the compound exponential current model using 3 sets of mesh sizes	47
3.5	The effect of field point range on calculated radiation waveforms	48
3.6	The effect of propagation speed on calculated radiation waveforms	49

LIST OF ILLUSTRATIONS (Cont'd.)

Figure		Page
3.7	The effect of current rise time on calculated radiation waveforms.	50
3.8	The analytical solutions and channel geometries for benchmark problem set 1	52
3.9	Reproduced channel geometries and calculated electric fields using the EMFIELD code for benchmark problem set 1.	54
3.10	Total current and its three components at ground in the modified current model of Lin, et al.	55
3.11	Electric fields at ground and above ground calculated for benchmark problem set 2 by Master et al.	58
3.12	Modified current model of Lin et al. used in EMFIELD solutions for benchmark problem set 2.	59
3.13	Calculated electric fields using the EMFIELD code for benchmark problem set 2	60
4.1.a	Simple channel geometries designed for this study.	66
4.1.b	Simple channel geometries designed for this study (continued).	67
4.2	Reference case for compound exponential current model	69
4.3.a	Calculated electric fields using compound exponential current model for designed tortuous channels	70
4.3.b	Calculated electric fields using compound exponential current model for designed tortuous channels (continued).	71
4.3.c	Calculated electric fields using compound exponential current model for designed tortuous channels (continued).	72
4.4	Reference case for the modified current model of Lin et al.	75
4.5.a	Calculated electric fields using the modified current model of Lin et al. for designed tortuous channels	76
4.5.b	Calculated electric fields using the modified current model of Lin et al. for designed tortuous channels (continued).	77

LIST OF ILLUSTRATIONS (Cont'd.)

Figure		Page
4.5.c	Calculated electric fields using the modified current model of Lin et al. for designed tortuous channels (continued).	78
4.6	Calculated electric fields using two current models for simulated tortuous channels	82
5.1	Relative locations and viewing angles of the multistation TV camera network	88
5.2	Reproduction of TV images of flash GNV1.	90
5.3	Reproduction of TV images of flash GNV2.	91
5.4	Calculated and measured electric field changes for flash GNV1.	95
5.5	Calculated and measured electric field changes for flash GNV2.	97
5.6	Calculated and measured electric field changes for flash NSSL9, R2.	103
5.7	Calculated and measured electric field changes for flash NSSL9, R4.	104
5.8	Calculated and measured electric field changes for flash NSSL9, R5.	105
5.9	Another possible acoustic sources reconstructed from thunder data for NSSL flash 9.	107
5.10	Calculated and measured electric field changes for flash NSSL10, R4.	109
5.11	Calculated and measured electric field changes for flash NSSL10, R5.	110

THE EFFECTS OF CHANNEL TORTUOSITY ON ELECTROMAGNETIC RADIATIONS FROM LIGHTNING RETURN STROKES

CHAPTER I

INTRODUCTION

1.1 Historical Survey

Lightning is one of nature's oldest wonders. For many thousands of years, the flight of thunderbolts was universally thought to be a manifestation of the power and wrath of the gods. Many of the fabulous legends and freak folklores told, with terror and respect, enchanting stories about lightning and thunder. The lack of understanding has added many mythical features to lightning, which can be found in various religions and cultures throughout the primitive and civilized world (Viemeister, 1972). To many people of ancient civilizations, lightning also has actually encompassed such things as decision making and political affairs. Even today, the eagle on the back of our dollar bill still clinches a bundle of lightning arrows in its claws, a legacy of the early Greek belief that lightning was the weapon of Zeus, father of all gods, for peace and justice.

Yet common as these stories are, the understanding of lightning phenomena is still not very satisfactory and far from complete. No true understanding about lightning was achieved before the seventeenth century, when scientists in Europe began their electrical experiments. Friction machines for generating static electricity and Leyden jars for charge storage opened the doors for investigating many interesting phenomena, such as the nature of electrical charges, the electrical properties of materials, and the sparks in high-voltage discharges. It was Benjamin Franklin who suspected and proved that thunderclouds are electrified, and he also proposed lightning rods for building protection (Cohen, 1941). Since then, a wealth of scientific information about lightning has been accumulated, and with the advancement of modern science and technology, considerable progress in understanding the nature of lightning has been achieved.

1.2 Lightning Phenomena

Lightning is a very complex natural phenomenon and has a full range of properties that usually cannot be observed in a controlled laboratory environment (Fowler, 1976). There are several reasons for this state of affairs. First, the atmospheric conditions change dynamically during lightning as opposed to the relatively static and uniform air conditions prevailing during laboratory sparks. Second, the electric field between cloud and earth is not uniform and usually is irregular in contrast to the controllable field magnitude and electrode geometry in laboratory sparks. Third, basic parameters such as current, voltage, wave propagation speed, electron-ion density, and radiation spectra of lightning are very difficult to measure directly unlike those in laboratory sparks. Finally, laboratory sparks have a complete outer circuit, which is balanced and can be monitored, while in lightning, the governing global circuit from ionsphere to thundercloud and then to earth is not known and cannot easily be monitored. Therefore, lightning investigations are mostly phenomenological observations and classifications. Explanation of some very basic questions, such as cloud electrification, lightning initiation and channel tortuosity, etc., are still not complete. As to ball lightning, bead lightning, and the incredible "bolt from the blue," these events occur rarely and are barely understood today. In the following paragraphs, a summary describing the general lightning phenomena will be presented.

Lightning has been observed in snowstorms, sandstorms, in the clouds over erupting volcanos, and near nuclear explosions, but the most common generator of lightning is thunderstorms. Two general conditions must exist in order for lightning to occur in thunderclouds: (1) the overall electric field within the thundercloud due to cloud electrification processes must be sufficiently strong (10 to 50 kV/m), and (2) there must be some place within the cloud where the electric field exceeds 300 kV/m. A field strength of 300 kV/m is insufficient to cause a breakdown by itself; breakdown fields are probably achieved by corona emissions from precipitation, which serve to concentrate the field in a very small region. Theoretical studies indicate that two or three successive corona streamers can produce a field of 1 MV/m over a distance of about 2 - 3 m (Griffiths and Phelps, 1976). Fields at the tip of this streamer thus are intense enough to cause the breakdown to self-propagate and subsequently develop into a complete lightning channel.

Lightning in a thunderstorm can take place between a cloud and the surrounding air (air discharge), within a cloud (intracloud discharge), between two clouds (cloud-to-cloud discharge), and between a cloud and the earth (cloud-to-ground discharge). Since cloud-to-ground discharges are the most favorable for observation, as well as of practical importance regarding property damage and threat to life, they have been the subjects of great interest and continuous investigation. In this research, only cloud-to-ground lightning flashes will be studied.

A typical cloud-to-ground flash (Uman, 1969) lasts about 0.2 s. It starts with a preliminary low-current discharge called the stepped leader. The stepped leader usually develops from a region of concentrated negative charge and moves downward below the cloud base in steps 50 to 100 m long. With each step, a portion of the cloud's charge is lowered and deposited along the path, leaving a conductive channel behind. The next step then can progress from the tip of the previous leader channel. Each step takes roughly 1 μs, and there is a pause of about 50 μs between steps. When the stepped leader is about one or two step lengths from the ground, the electric field near the ground is highly intensified by the charge induced on the ground. This is sufficient to cause upward-moving discharges originating from elevated pointed objects on the ground. When one of these discharges meets the downward-propagating leader tip, a complete conducting channel between the cloud and ground is formed; hence a very bright return stroke is initiated. This return stroke is a high-current wavefront, which travels up the ionized channel created by the stepped leader. The velocity of this first return stroke has been observed to be 1/2 to 1/10 the speed of light. It lasts about 100 μs, and the average current is 20 kA. Figure 1.1 shows a typical cloud-to-ground lightning flash as would be recorded by a camera with moving film (Uman, 1969). After the first return stroke, if additional charge is made available by junction processes, which appear to drain more charges from other regions of the cloud, the flash may have additional strokes. After the additional charge has moved to the channel top, a continuous (instead of stepped) dart leader may follow the original channel, deposit charge along the channel as before, and initiate a second return stroke. This leader-stroke process may be repeated in the same channel several times, with each stroke being separated by 40 ms or so. Most of the subsequent return strokes are without branches or with very few. Dart leaders propagate faster and more smoothly than the stepped leaders because the air in the channel is still hot and ionized, which makes its resistance smaller. Sometimes, the dart leader changes into a stepped leader midway on its way to the ground because the lower part of the original channel is insufficiently ionized due to a long interstroke duration (>100 ms). This kind of leader is referred to as a dart-stepped leader. It will often initiate a stroke similar to the first, i.e., highly branched and having a relatively bright channel.

If a lightning flash occurs a short distance away, we may hear thunder. A true understanding of thunder generation was not established until the twentieth century. However, a number of important questions still need further research. The explanation now being generally accepted by the scientific community (Few, 1975) is as follows. The passage of lightning current abruptly dissociates, ionizes, and heats

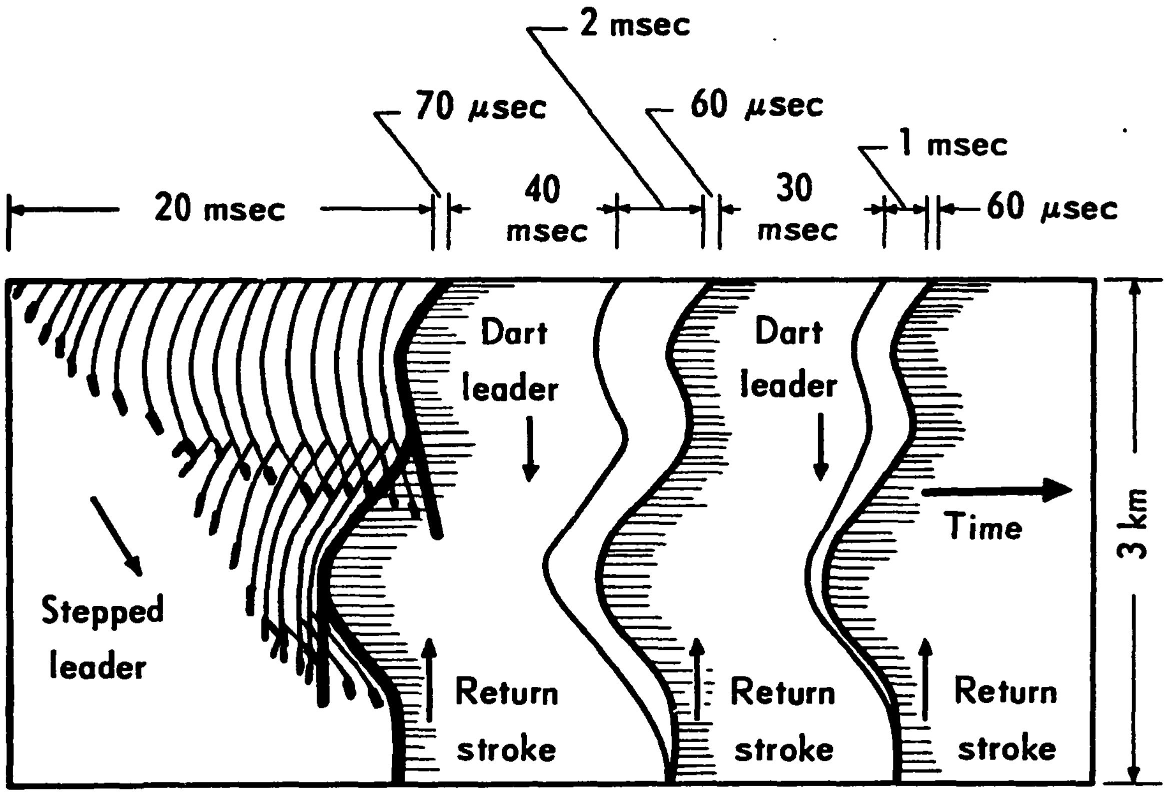

Figure 1.1 The luminous features of a cloud-to-ground lightning flash as recorded by a camera with moving film (after Uman, p.6, 1969).

the air along the channel. This results in a sudden increase of temperature and pressure, causing the air to expand rapidly. The explosion of the heated air causes shock waves that, after traveling a short distance, decay into acoustic waves. A number of factors influence the frequency and amplitude of thunder heard by an observer. The amount and rate of energy input into a channel, the distance and orientation of the channel to the observer, reflections from buildings or terrain, and atmospheric conditions can all affect the perceived sound. Since lightning is an extended, tortuous acoustic source, these parameters will vary for different channel segments, resulting in the variations in amplitude and frequency that are called rumbling. It is possible to reconstruct the geometry of the lightning channel by using an array of microphones to record the acoustic waveforms of thunder (Few, 1970). The details of the channel reconstruction technique used in this thesis will be discussed further in Chapter II.

1.3 Recent Studies of Return Stroke Models

The electric current in the return stroke is one of the most important parameters in the study of lightning discharges. For scientists, a detailed knowledge of lightning current can be used to derive some very basic information about the lightning flash, such as its charge, energy, radiated electric and magnetic fields, and many other related parameters. For engineers, a knowledge of the waveform and amplitude of the current can provide them sufficient information to help solve the problems of lightning protection. Recent research has also indicated that lightning discharges are closely related to the acid rain problems caused by air pollutions in industrial metropolitan areas. It has been speculated that the contribution to the acidity of rain from the production of nitric oxides due to lightning discharges in the atmosphere could be far greater than that of anthropogenic sources (Chameldes, et al., 1976; Hill and Rinker, 1981).

According to Uman (1980), there are three different types of mathematical modeling of return stroke currents, each containing different degrees of physical complexity. The most basic return stroke model attempts to predict the channel current as a function of time and height in terms of equations of continuity of mass, energy, and momentum and the Maxwell equations which govern the electrodynamic behavior of the plasma. This return stroke model requires a detailed knowledge of physical parameters of the channel, such as ionization and recombination coefficients of air and its thermodynamic and electromagnetic properties (Nasser, 1971). An electron fluid model of the breakdown wave propagation has been developed and tested for laboratory sparks by several investigators. In particular, Fowler (1976) and his co-workers established an electron fluid theory that included a photoionization process, which is important in the breakdown wave propagation. Their solutions in general fitted reasonably well with available experimental data. However, the question of just how important the photoprocess is remains to be solved, and the solutions of the electron fluid equations in cylindrical tubes or other more general geometries require much more additional work. This approach has also been investigated recently by Strawe (1979).

The second type of modeling involves mathematical description of the return stroke channel as an R-L-C electric circuit of a transmission line. It assumes that all of the basic processes involved in the lightning channel can be modeled as lumped parameters of the circuit elements, which are allowed to vary with time and height (Price and Pierce, 1977; Little, 1978, 1979). Limited success has been achieved using this model to derive the general characteristics of the lightning current and the resulting electromagnetic field. The major difficulty with this model is the determination of the input parameters, which are often selected more or less arbitrarily in order to match the observed data.

The third type of modeling is based on a totally pragmatic approach to the problem. First, an empirical model of return stroke current is established using measured data; then the electric and magnetic fields are calculated and compared with the measurements. This process can be iterated in many ways to improve overall consistency. The two most commonly used models of this type are the Bruce-Golde model (Bruce and Golde, 1941; Dennis and Pierce, 1964) and the transmission line model (Wagner, 1960; Wagner and Hileman, 1961; Uman and McLain, 1969, 1970; Uman et al. 1973, a,b). In the Bruce-Golde model, a double exponential expression of the form

$$I = I_o\,[\exp(-at) - \exp(-bt)] \tag{1.1}$$

is used. The inherent assumption underlying this model is that the current amplitude is constant at any instant along the channel below the return stroke wavefront. In the transmission line model, the current waveform is allowed to propagate at a finite speed. Lin et al. (1980) did an extensive evaluation and compared these two models with data obtained simultaneously at two Florida stations. It was found that both of these models were inadequate to describe their experimental data. They then proposed a new return stroke model, which yielded good approximations to their measured two-station field data. In all of their calculations, a straight vertical channel was used, and a constant return stroke velocity was assumed. The technique of Lin et al. requires considerable efforts of trial and error in order to find an acceptable current model for each individual return stroke. This model is not uniquely defined, since it uses several arbitrary parameters. Thus different sets of currents and charges might be found that produce the same fields as those measured. Furthermore, their derived currents showed a very sharp initial peak and a following dip that has not been observed in any measurements. Since all these techniques have deficiencies, further investigations and refinements of return stroke models are still needed.

1.4 Scope of this Research

The study of lightning return strokes in the past has been generally confined to either very simple or artificially assumed channel geometries. This is due to the lack of complete and consistent experimental data on one hand, and the limitations of analytical solutions to the electromagnetic field changes on the other. However, with the development of several advanced lightning mapping systems in recent years (Few, 1974; Hill, 1977; Taylor, 1977), it is now possible to reconstruct more realistic channel geometries, and then evaluate the return stroke models by solving Maxwell's equations using numerical techniques for such a complex system.

In this research, the channel geometry for several lightning return strokes will be reconstructed from two independent sets of experimental data. The first set was obtained at the National Severe Storms Laboratory (NSSL) at Norman, Oklahoma in Spring 1979, and the second set was provided by the Lightning Research Laboratory at the University of Florida. Lightning data from NSSL were acquired simultaneously with three major detection systems: (1) a microphone array for recording thunder data, (2) a fast antenna (Brook and Kitagawa, 1962) for measuring electric field change waveforms during return strokes, and (3) a slow antenna (Brook and Kitagawa, 1962) for recording the gross electric field changes during the lightning flash. Television video records of lightning flashes were also taken whenever possible. Atmospheric conditions were obtained from Rawinsonde data and a surface meteorological network that measures wind velocity, pressure, temperature, and humidity. A number of other sensors were also used by cooperating scientists to provide additional information. Two 10-cm Doppler radars provided the overall storm structure (Doviak et al., 1979). A dual-station wide-band VHF mapping system (Taylor, 1977) provided the gross feature of the discharge sources, and a crossed-loop lightning location system (Krider, et al., 1976) provided the ground strike points within 200 km. Lightning data from the University of Florida were obtained simultaneously with two detection systems: (1) a multistation video system for recording lightning pictures and (2) a sensor for measuring electric field waveforms during return strokes.

Based on the best lightning channel geometry reconstructed, several return strokes will be analyzed and evaluated by comparing the calculated electric field changes with the measured field data. The effect of channel tortuosity on the field measurement will be addressed in detail. A self-explanatory block diagram which depicts the entire research plan is shown in Figure 1.2.

This research emphasizes several important features that are not found all together in other studies:

1. Numerical solutions instead of analytical solutions of Maxwell's equations will be performed. This will greatly enhance the mathematical rigor in dealing with a complex problem and allow a more realistic as well as a more complete modeling of the actual lightning event.

2. A computer code based on the numerical algorithm for solving the Maxwell's equations for lightning return stroke will be developed. Confidence in the computer code will be established by comparing results with existing solutions from other independent sources.

3. A study will be conducted to acquire a basic understanding of the impacts of various channel geometries on the calculated electric field waveforms using different return stroke models.

4. An actual channel geometry reconstructed from experimental data will be used instead of a vertical straight line or some artificially assumed channels. The impacts of channel tortuosity in lightning electric field changes will be examined extensively.

5. The antenna circuit response to the electric field waveform of return strokes will be analyzed, and the relationship between

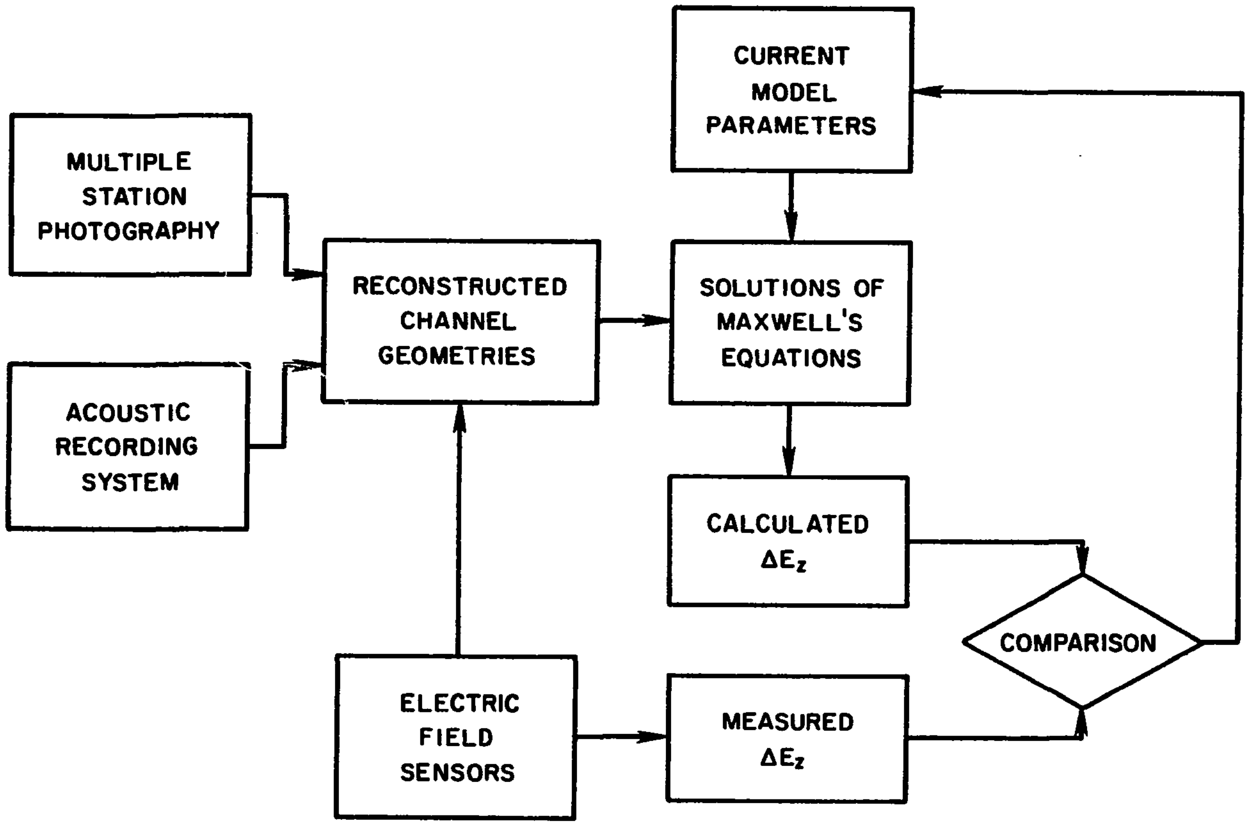

Figure 1.2 Block diagram of the research plan.

measured output voltage and the electric field at the sensing plate will be derived.

6. Calculated electric field waveforms will be compared with the measurements inferred from the fast antenna data. A total consistency among the channel reconstruction, electric field changes, and the return stroke current model will be sought, and the results assessed.

CHAPTER II

INSTRUMENTATION AND DATA PROCESSING

2.1 Acoustic System and Channel Reconstruction

2.1.1 Experimental Setup

The techniques of lightning acoustic data acquisition and processing for this research were originated and developed by Few et al., (1967), Few (1968, 1969), Teer (1972, 1973), Few and Teer (1974), and MacGorman (1978). Equipment and technical assistance were provided by Professor A. A. Few of Rice University during the course of this research.

The measurement system consists of an array of four Globe 100 C microphones. The pressure sensitive element of the Globe microphone is a circular, parallel-plate capacitor formed by a thin, aluminized mylar film that is stretched close to a perforated metal plate. Behind the plate is a chamber containing air at atmospheric pressure. Fluctuations of air pressure impinging on the mylar film cause changes in the capacitance of the chamber; these changes in turn cause output voltage variations proportional to the magnitude of the air pressure fluctuations. The microphones have very high sensitivity, and the frequency response is essentially flat to within 3 dB over the range from 0.1 Hz to 500 Hz. The microphones were laid out in a square with sides of 50 m. The center of the square was located at a distance of 211 m southwest of the electric field measurement system as shown in Figure 2.1. Each microphone was set on a dirt pile about a half meter high to prevent flood damage. The heights of dirt piles were carefully surveyed and adjusted so that all four microphones were at the same height. A schematic diagram of the thunder data recording system is shown in Figure 2.2. The signal from each microphone was transmitted by cable to an array control box. The control box provided power to the microphones from five lead acid batteries. The output signals were transmitted by cable from the control box to a data control panel inside the Storm Electricity Building (SEB) which served as the central base. The data control panel allows the operator to adjust the gains (from 1 to 100) to maintain adequate signal levels without saturation. It could also filter out low frequency noise from the strong winds, which are common in Oklahoma storms. Signals from all four microphones were recorded simultaneously on an SE Labs 7000 M 14-channel analog tape recorder along with other measurements, such as slow antenna, fast antenna, corona current, and an IRIG B format time code from a Systron-Donner 8152 time code generator synchronized with radio station WWV. Acoustic signals were also recorded on a Honeywell 906C oscillograph recorder along with slow antenna data and time. These oscillograph data printed instantly and provided not only immediate information during the course of data acquisition but also a complete permanent visual record for later analysis. The analog waveforms recorded on the tape recorder were later digitized at Rice University through a Raytheon 10-bit analog-to-digital converter

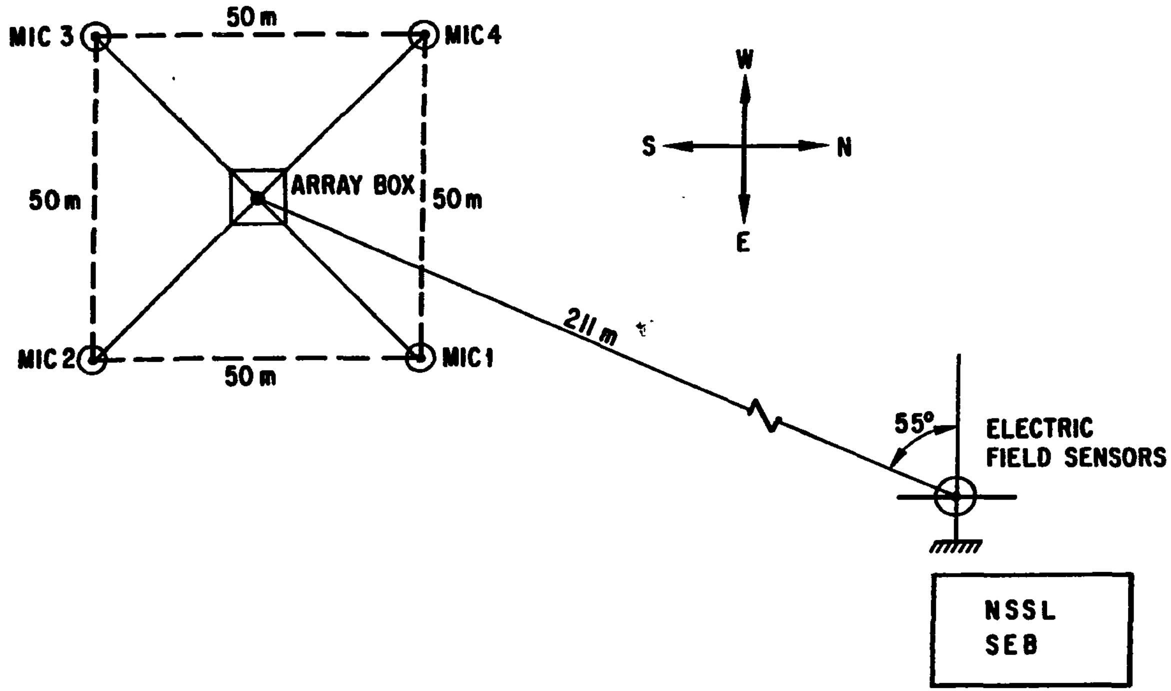

Figure 2.1 Locations of the microphone array and the electric field sensors.

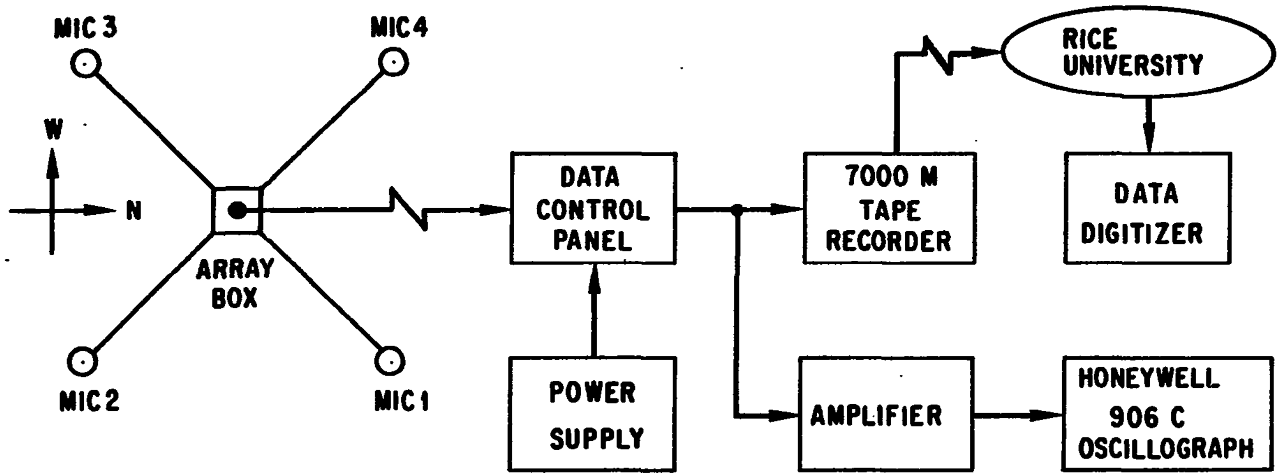

Figure 2.2 Schematic diagram of the thunder data recording system.

at a sampling rate of 2000 points per second. These digitized acoustic data were then used to reconstruct channel geometry.

The geometry of lightning channels can be reconstructed by a ray tracing technique using acoustic data obtained with an array of microphones. The theory and techniques for ray tracing have been developed by Few (1970), Teer (1972, 1973), Few and Teer (1974) and MacGorman (1977, 1978). The feasibility of this technique has been demonstrated by these authors, and its accuracy has also been investigated in detail. It was found that the large scale features of lightning channels could be reconstructed reasonably well as judged by photographs and by consistency checks from arrays separated 1 ~ 2 km. The accuracy of the reconstructed channel geometry depends on the temperature and wind velocity as a function of altitude; errors of 10% for high altitude sources and 25% for sources near the horizon might occur in adverse conditions. However, by using supportive data on wind and temperature profiles, the estimated errors can be reduced to 5% (MacGorman, 1978), which is considered sufficient for this research. A summary of ray tracing techniques excerpted from the work of these authors is presented in Appendix I.

2.1.2 Lightning Channel Reconstruction

One of the major objectives of this research is to compare the measured electric field waveforms with model calculations using reconstructed channel geometry. It is essential to have good quality thunder and electric field data obtained simultaneously. Recognizing the fact that nature does not always cooperate and equipment has limits, one has to go through many tedious and time-consuming processes to sort out and screen the raw data. After examining all the oscillograph data taken at NSSL in the Spring and Summer of 1979, five storms were selected as potential candidates for further investigation, and the associated thunder data were digitized using existing facilities designed for this purpose at Rice University. The date and time of these five storms are listed in Table 2.1. A total of 284 cloud-to-ground flashes within a range of 25 km were indicated by the lightning locator data; among those flashes, some did not have good thunder signals, some saturated the acoustic system or electric field sensors, and several possibly good data were missed during tape changes. During the mature stage of a thunderstorm, intense lightning activity is usually observed; and it is quite common to have several flashes within one minute. In this case, the thunder signals cannot be distinguished from each other or associated with a particular flash, and this renders the acoustic signals useless. Only 16 flashes were found to have matching slow antenna field changes and thunder signals during screening of all the oscillograph records. Table 2.2 contains pertinent information and the digital tape file record numbers of these 16 flashes.

The next step in the data screening process was to scrutinize electric field waveforms from the fast antenna by replaying the analog tape data into a transient waveform analyzer, which displayed the waveform on an oscilloscope. Flashes with unusable return stroke waveforms were rejected. These waveforms could be the result of instrument saturation, superposition of several lightning activities such as intra-cloud discharges or other cloud-to-ground flashes at different distances

TABLE 2.1. Five Selected Storms with Thunder Data Digitized at Rice University

Date	Time (CST)	Number of Flashes*
May 2, 1979	22:17:50 - 23:01:00	49
May 20, 1979	16:54:42 - 17:43:16	50
May 28, 1979	19:11:10 - 19:26:00	40
June 6, 1979	16:34:00 - 18:15:52	97
June 8, 1979	15:19:40 - 16:32:30	48

*Number of cloud-to-ground flashes within 25 km as indicated by lightning locator.

TABLE 2.2. Sixteen Multistroke Cloud-to-Ground Flashes with Matching Thunder Signals

Flash Number	Date	File Number	Time (CST)	Record Number of Field Changes	Record Number of Starting Thunder	Record Number of Ending Thunder
1	June 6, 1979	0457	1706:13	2968	2980	3230
2	June 6, 1979	0457	1708:26	3505	3510	3750
3	June 6, 1979	0557	1721:55	2699	2705	2905
4	June 6, 1979	0557	1724:44	3380	3390	3640
5	June 6, 1979	0757	1748:32	1135	1183	1417
6	June 6, 1979	0757	1755:54	2916	2953	3191
7	June 6, 1979	0857	1806:51	1557	1567	1833
8	June 6, 1979	0857	1812:59	3046	3050	3290
9	June 8, 1979	0359	1537:41	1679	1685	1954
10	June 8, 1979	0359	1541:28	2592	2602	2802
11	June 8, 1979	0459	1549:41	604	610	850
12	June 8, 1979	0459	1553:11	1452	1460	1700
13	June 8, 1979	0559	1610:26	1537	1550	1780
14	June 8, 1979	0559	1610:27	1540	1560	1800
15	May 28, 1979	0348	1920:34	2280	2290	2590
16	May 28, 1979	0348	1924:05	3131	3140	3340

arriving at the fast antenna simultaneously. Nine out of the 16 flashes appeared to have usable return stroke waveforms. Flashes 9 and 10 are both multiple-stroke events and have good quality waveforms. Flashes 13 and 14 are also multistroke events with good quality waveforms; however, there is some ambiguity and difficulty in the channel reconstruction because these two flashes occurred within 1 s of each other so the thunder data overlap. The remaining five flashes have waveform data of marginal quality and therefore will not be analyzed further. After going through the complete data screening process, flashes 9 and 10 were finally selected as samples to be analyzed in detail. Lightning channel geometries were reconstructed from the acoustic data, using the ray tracing technique discussed in Appendix I. The computer codes used for channel reconstruction were developed by MacGorman (1978) and implemented on the NSSL SEL computer.

A model had to be made to describe the atmospheric conditions for the times of the flashes that were to be reconstructed acoustically. The model parameters were obtained from data taken at stations located at Norman, Oklahoma City, and Chickasha. Temperature and wind profiles of the atmosphere at NSSL were obtained by averaging the data from the three stations. The resulting atmospheric model is shown in Table 2.3. The reconstructed channel geometries for flashes 9 and 10 are shown in Figures 2.3 and 2.4 respectively. More discussions on the reconstructed channels will follow in Chapter V.

TABLE 2.3. The Model Atmosphere Used in Ray Tracing Analysis for June 8, 1979

Layer	Altitude (m)	Temperature (°C)	Wind Speed (m/s)	Wind Direction (degree)*
1	0.0	18.8	4.0	0.0
2	339.0	17.8	9.5	60.0
3	659.0	16.5	8.0	120.0
4	1639.0	12.9	4.5	4.0
5	2139.0	11.2	7.8	8.0
6	4139.0	3.3	15.0	18.5
7	5139.0	-2.0	18.0	24.0
8	7139.0	-15.0	22.5	37.0
9	8939.0	-28.0	27.0	34.0
10	10889.0	-41.8	26.8	33.0
11	11439.0	-46.5	34.1	31.5
12	13939.0	-64.5	33.1	30.5
13	15639.0	-75.5	8.4	30.0

*The direction of the wind is measured clockwise from north.

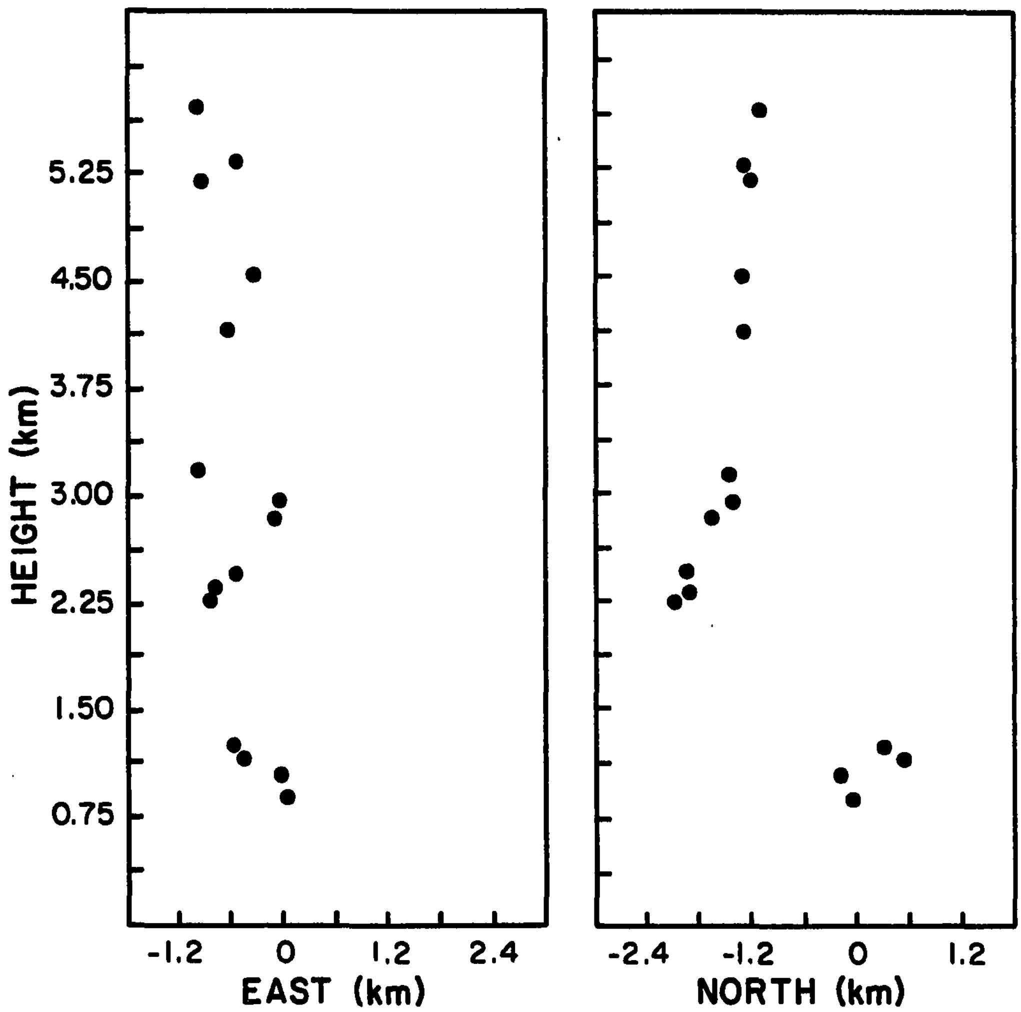

Figure 2.3 Channel geometry reconstructed from acoustic data for NSSL flash 9, 8 June 79, 1537:41 CST. The origin is located at the ground strike point.

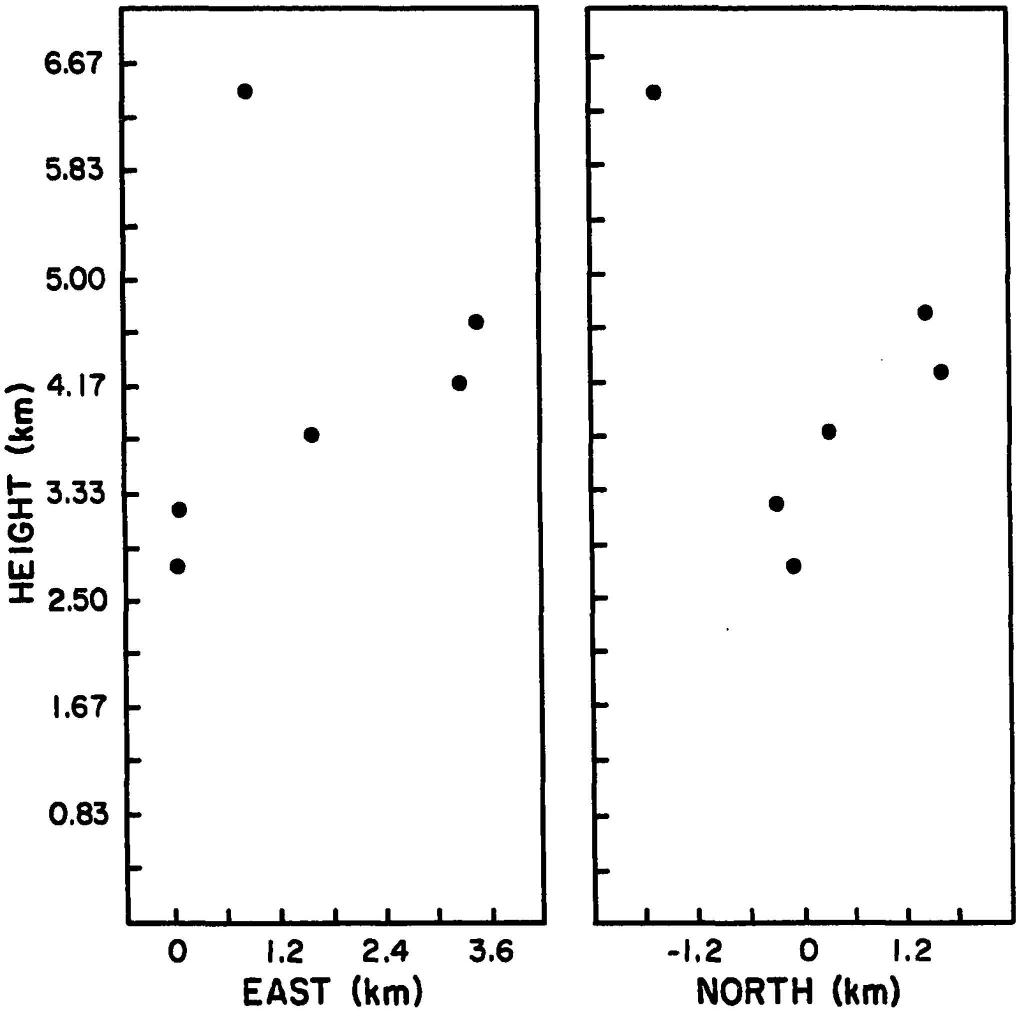

Figure 2.4 Channel geometry reconstructed from acoustic data for NSSL flash 10, 8 June 79, 1541:28 CST. The origin is located at the ground strike point.

2.2 Measurements of Lightning Electric Field Changes

The changes in the electric field at the earth's surface during lightning were measured with two field change sensors. The slow antenna was used to record the gross features observed in the lightning electric field change, such as its magnitude, polarity, number of strokes in a flash, and to identify whether a discharge was cloud-to-ground or intracloud. The fast antenna was used to delineate the detailed structure of the rapidly occurring field changes during a return stroke, such as its waveform, rise time and decay time, etc. The measurement technique was originally developed by Kittagawa and Brook (1960), and since then many circuit components have been replaced by modern high performance electronic products such as FET operational amplifiers, IC circuits, etc. These improvements of the fast antenna system have made this measurement technique a very powerful tool in modern lightning research (Brook, 1972).

Both antennas were installed near the microphone array as shown in Figure 2.1. The slow and fast antennas are physically identical and consist of an insulated round flat plate antenna of area A ($0.073\ m^2$) mounted 1.7 m above the ground on a metal post with the antenna surface parallel to the ground. The antenna is connected to an operational amplifier with appropriate gain control. A schematic diagram is shown in Figure 2.5. The operational amplifier is configured as a charge amplifier, which has the advantage of maintaining the antenna potential at virtual ground; therefore, the capacitance between the antenna and ground does not affect the field measurement. The surface charges induced on the sensing plate by the lightning electric

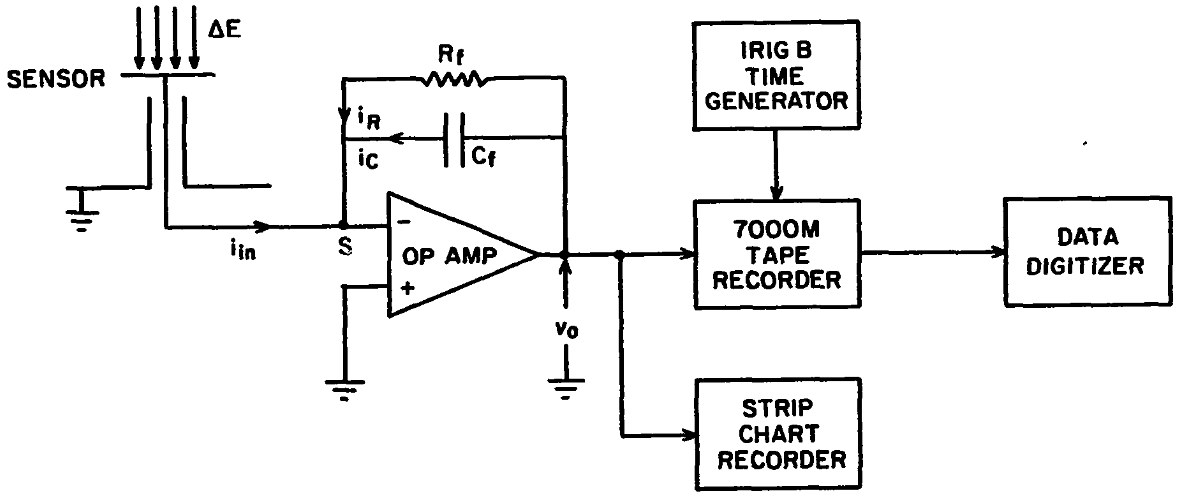

Figure 2.5 Schematic diagram of the electric field sensor and the associated measurement system.

field flows into the operational amplifier at the summing point. The amplified output voltage $V_o(t)$ will be compared with the calculated electric field changes in Section 5.3.2.

In the slow antenna, the R_fC_f time constant of the feedback loop was set at 10 s, which is much longer than the time duration of a lightning flash (typically <0.5 s). Figures 2.6 and 2.7 show the slow antenna outputs for flashes 9 and 10 respectively. Both flashes have field changes indicative of multistroke cloud-to-ground discharges (Kittagawa and Brook, 1960). The rapid, positive changes are due to the return strokes. Flash 9 has five distinguishable return strokes, and flash 10 has at least 6 return strokes. The trend of the leader field changes just before the return strokes (Uman, 1968) indicates that flash 9 occurred very close to the sensors while flash 10 occurred at a greater distance. This is confirmed by acoustic channel reconstruction results that indicate flash 9 occurred at a range of 2.35 km and flash 10 at 12.6 km.

In the fast antenna, the R_fC_f time constant of the feedback loop was set at 100 μs. The fast antenna data are used to study the details of the waveform of the electric field during a return stroke and other short time events (typically ~200 μs). Detailed analysis of the fast antenna output waveforms will be presented in Chapter V along with theoretical results.

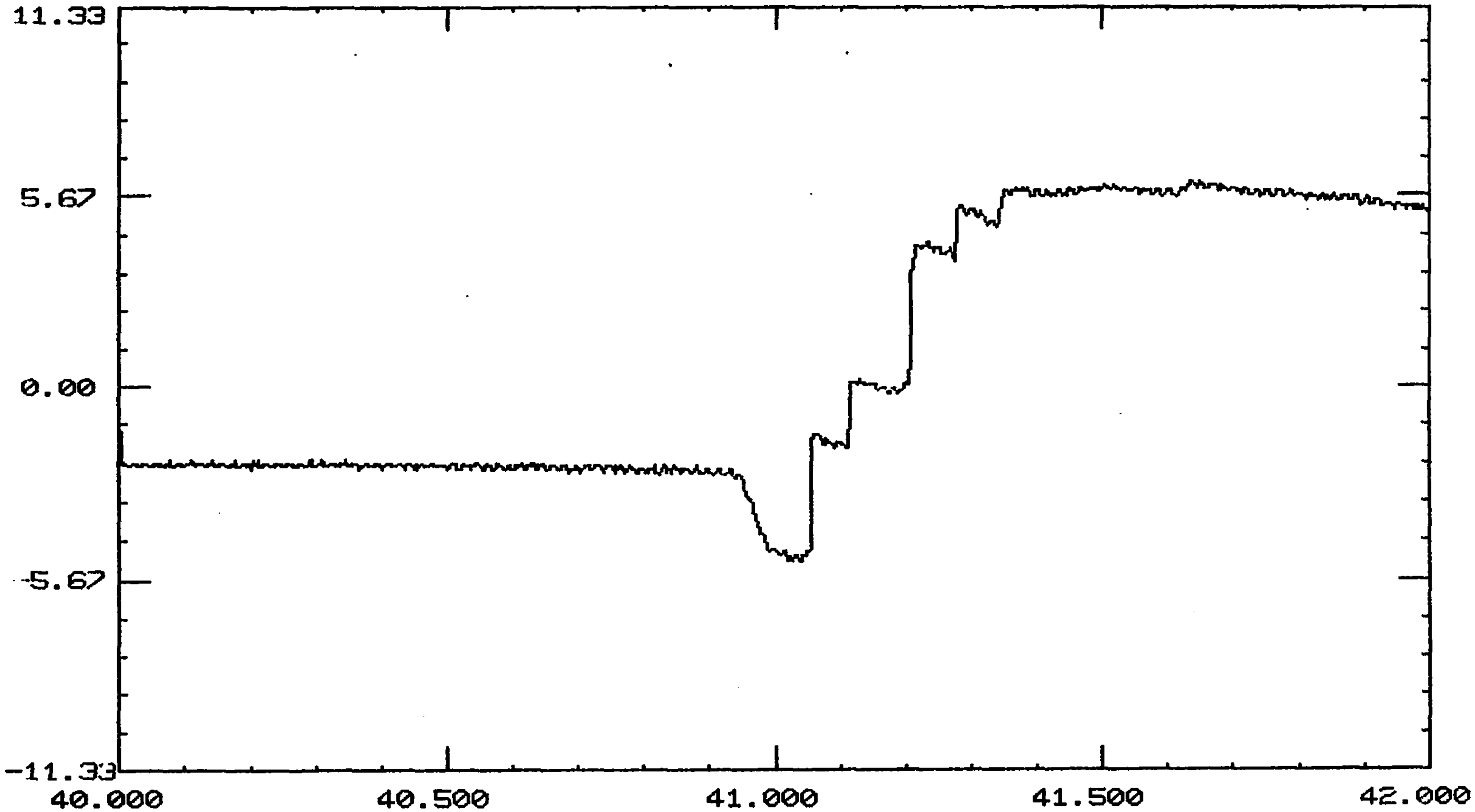

Figure 2.6 Slow antenna output for NSSL flash 9. The time axis is labelled in seconds after 1437 CST.

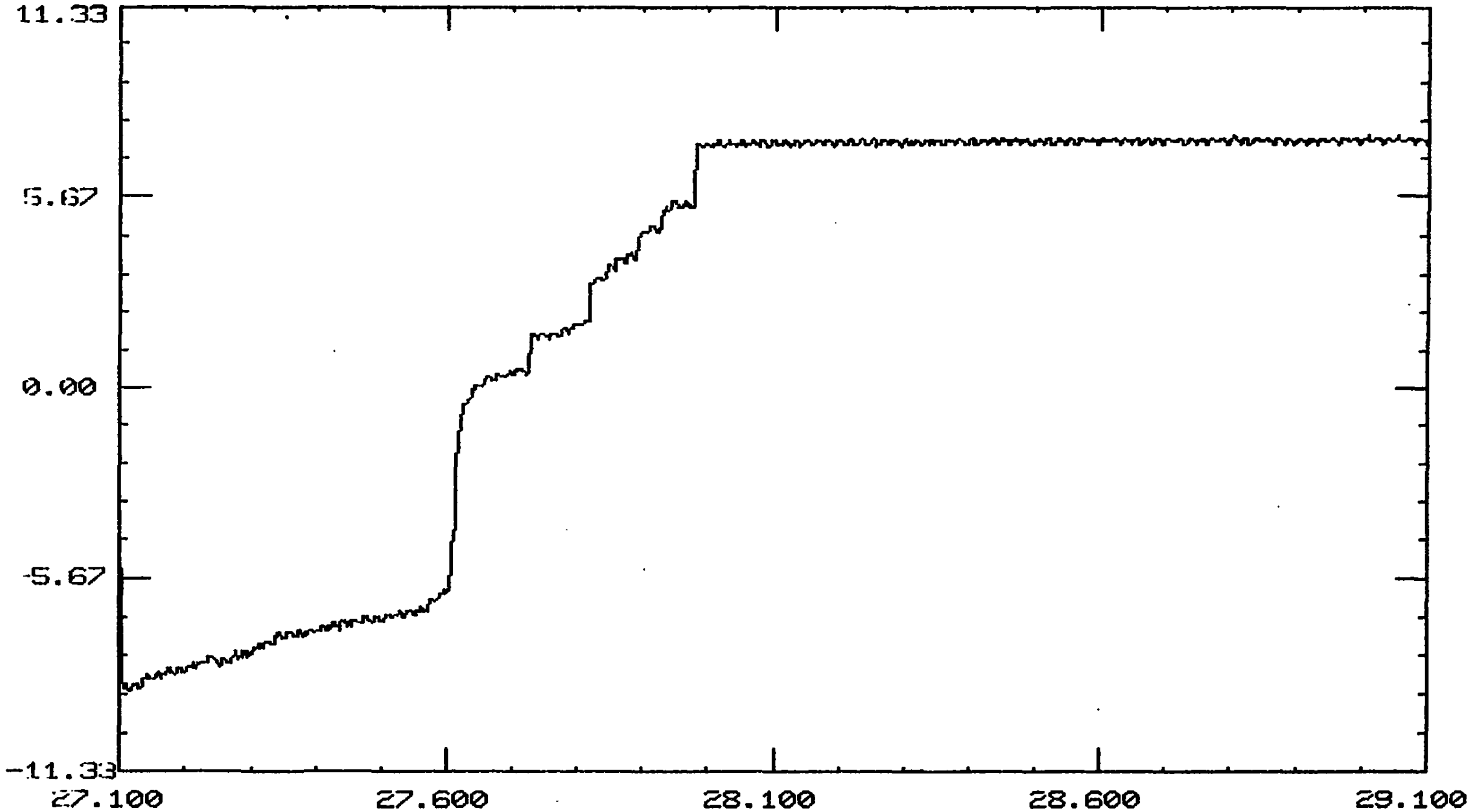

Figure 2.7 Slow antenna output for NSSL flash 10. The time axis is labelled in seconds after 1541 CST.

CHAPTER III

THEORETICAL ANALYSIS OF ELECTROMAGNETIC FIELD CHANGES DURING LIGHTNING RETURN STROKES

3.1 Maxwell's Equations and Lightning Return Strokes

The general equations which govern the electromagnetic field changes in the atmosphere during lightning return strokes are Maxwell's equations

$$\vec{E} = -\vec{\nabla}\phi - \frac{\partial \vec{A}}{\partial t} \tag{3.1}$$

$$\vec{B} = \vec{\nabla} \times \vec{A} \tag{3.2}$$

where the scalar potential ϕ is given by

$$\phi(\vec{r}, t) = \frac{1}{4\pi\varepsilon_o} \int_{v'} \frac{\rho\left(\vec{r}', t - \frac{R}{c}\right)}{R} d\vec{r}' \tag{3.3}$$

and the vector potential $\vec{A}$ is given by

$$\vec{A}(\vec{r}, t) = \frac{\mu_o}{4\pi} \int_{v'} \frac{\vec{J}\left(\vec{r}', t - \frac{R}{c}\right)}{R} d\vec{r}' \tag{3.4}$$

with the requirement that

$$\vec{\nabla} \cdot \vec{A} + \frac{1}{c^2}\frac{\partial \phi}{\partial t} = 0 \tag{3.5}$$

In the above equations, ρ is the electric charge density, $\vec{J}$ is the current density, c is the speed of light in free space, ε_o and μ_o are the permittivity and the permeability of free space respectively, and R is the distance between the source point $\vec{r}'$ and the field point $\vec{r}$. The retarded time, $\tau = t - \frac{R}{c}$, is the time required for the radiation from the source point to propagate to the field point. The integrations are carried out through the local source distribution volume v' containing charge within a thunderstorm.

The electromagnetic field changes during lightning return strokes can be obtained by solving Maxwell's equations, provided that the source distributions are given and the initial conditions and boundary values are specified for a given geometry. However, in reality, only a few limited cases with very simple geometry permit complete analytical solutions (McLain and Uman, 1971). The reasons are primarily twofold: one is that the source distributions are not known precisely, and the other is that the channel geometry is complicated (MacGorman, 1978). Therefore, a numerical method is considered the most appropriate approach to study lightning (LeVine and Meneghini, 1978). Although it does not yield solutions in closed forms, the usage of a numerical method does allow a more realistic lightning channel geometry to be used, and it adapts quite easily to various assumptions for the source distributions.

3.2 Mathematical Algorithm and Numerical Solutions

The lightning return stroke is assumed to occur in free space above a perfectly conducting ground plane as shown schematically in Figure 3.1. The return stroke current pulse $\vec{I}$ is propagating upward along the channel as shown. The sensing instrument is located at the field point $\vec{r}$.

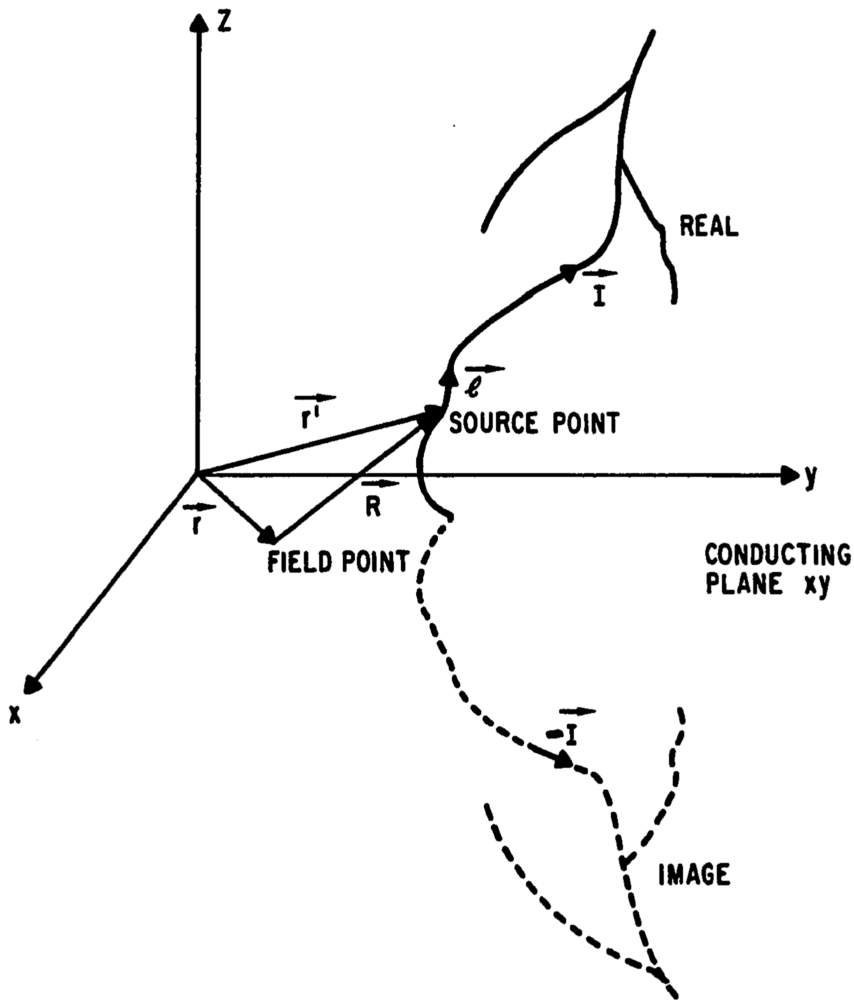

Figure 3.1 Depiction of a lightning return stroke and its image. The origin is the center of the acoustic system, and the electric field sensor is located at the field point. The real current $\vec{I}$ is propagating up the channel.

According to the boundary condition, the scalar potential ϕ must be equal to zero everywhere on the ground. This can be most easily achieved by using the method of images. In Figure 3.1, the mirror image of the real channel is constructed with the dotted lines, along which an image current pulse $-\vec{I}$ is propagating downward. The solutions of Maxwell's equations can be obtained from both the real and the image current sources. In the following sections, a mathematical algorithm suitable for computer implementation is developed to obtain the electromagnetic fields of interest.

3.2.1 Vector Potential

Since a current pulse is propagating along the lightning channel, the current density $\vec{J}$ in Equation 3.4 can be replaced by a current pulse $\vec{I}$, and the volume integral becomes a line integral. Hence

$$\vec{A}(\vec{r}, t) = \frac{\mu_o}{4\pi} \int_{\ell} \frac{\vec{I}\left(\vec{r}', t - \frac{R}{c}\right)}{R} d\vec{\ell} \tag{3.6}$$

where $R = \left|\vec{r} - \vec{r}'\right|$ is the distance from the source point to the field point and $d\vec{\ell}$ is along the channel $\vec{\ell}$. The channel is divided into N segments, and the integration is approximated by summation (Fröberg, 1964). The resulting expression is

$$\vec{A}(\vec{r}, t) \cong \frac{\mu_o}{4\pi} \sum_{i} \frac{\vec{I}_i(\vec{r}_i', \tau_i)}{R_i} \Delta\ell_i \tag{3.7}$$

where $\Delta\ell_i$ is the length of the i-th segment and $\tau_i = t - \frac{R_i}{c}$ is the retarded time.

The length of each segment $\Delta\ell_i$ should be chosen such that $\frac{\Delta\ell_i}{v}$ is sufficiently small in order to achieve reasonable accuracy for the approximation in Equation 3.7, where v is the propagation speed of the current pulse along the channel. Although the accuracy of the numerical solutions improves with decreasing segment length, the computer time increases. Therefore, the ultimate choice is a balance between the solution accuracy and the computing cost. More discussions will be given later in Section 3.3.

The summation in Equation 3.7 is over all i such that

$$\frac{R_i}{c} + \frac{L_i}{v} \leq t \tag{3.8}$$

where L_i is the total length of the channel from the ground to the i-th segment which has been traveled by the current pulse, i.e.,

$$L_i = \sum_{j=1}^{i} \left[(x'_j - x'_{j-1})^2 + (y'_j - y'_{j-1})^2 + (z'_j - z'_{j-1})^2\right]^{1/2} \tag{3.9}$$

A unit vector $\hat{\ell}_i$ along the channel is defined by

$$\hat{\ell}_i = \frac{d\vec{\ell}_i}{\left|d\vec{\ell}_i\right|} \cong \frac{1}{\Delta\ell_i} \left\{(x'_i - x'_{i-1})\ \hat{i} + (y'_i - y'_{i-1})\ \hat{j} + (z'_i - z'_{i-1})\ \hat{k}\right\} \tag{3.10}$$

Since the current pulse $\vec{I}$ is propagating along the direction $\hat{\ell}_i$, therefore

$$\vec{I}_i(\vec{r}'_i, \tau_i) = I_i(\vec{r}'_i, \tau_i)\ \hat{\ell}_i \tag{3.11}$$

By substituting Equation 3.10 into Equation 3.11 for $\hat{\ell}_i$, the current becomes

$$\vec{I}_i(\vec{r}_i', \tau_i) = \left\{ \frac{I_i(\vec{r}_i', \tau_i)}{\Delta\ell_i} (x_i' - x_{i-1}') \right\} \hat{i}$$

$$+ \left\{ \frac{I_i(\vec{r}_i', \tau_i)}{\Delta\ell_i} (y_i' - y_{i-1}') \right\} \hat{j} \tag{3.12}$$

$$+ \left\{ \frac{I_i(\vec{r}_i', \tau_i)}{\Delta\ell_i} (z_i' - z_{i-1}') \right\} \hat{k}$$

This can also be written as

$$\vec{I}_i(\vec{r}_i', \tau_i) = I_{xi}(\vec{r}_i', \tau_i)\, \hat{i} + I_{yi}(\vec{r}_i', \tau_i)\, \hat{j} + I_{zi}(\vec{r}_i', \tau_i)\, \hat{k} \tag{3.13}$$

with each component defined as

$$I_{xi}(\vec{r}_i', \tau_i) = \frac{I_i(\vec{r}_i', \tau_i)}{\Delta\ell_i} (x_i' - x_{i-1}') \tag{3.13a}$$

$$I_{yi}(\vec{r}_i', \tau_i) = \frac{I_i(\vec{r}_i', \tau_i)}{\Delta\ell_i} (y_i' - y_{i-1}') \tag{3.13b}$$

$$I_{zi}(\vec{r}_i', \tau_i) = \frac{I_i(\vec{r}_i', \tau_i)}{\Delta\ell_i} (z_i' - z_{i-1}') \tag{3.13c}$$

Substituting Equation 3.12 into Equation 3.7, the components of the vector potential are obtained:

$$A_x(\vec{r}, t) \simeq \frac{\mu_o}{4\pi} \sum_i \frac{I_{xi}(\vec{r}_i', \tau_i)}{R_i} \Delta\ell_i \tag{3.14a}$$

$$A_y(\vec{r}, t) \simeq \frac{\mu_o}{4\pi} \sum_i \frac{I_{yi}(\vec{r}_i', \tau_i)}{R_i} \Delta\ell_i \qquad (3.14b)$$

$$A_z(\vec{r}, t) \simeq \frac{\mu_o}{4\pi} \sum_i \frac{I_{zi}(\vec{r}_i', \tau_i)}{R_i} \Delta\ell_i \qquad (3.14c)$$

Notice that in the above equations the summations are over all i that satisfy Equation 3.8. Furthermore, the summation must include current source contributions from both the real and the image channels.

3.2.2 Magnetic Field

According to Equation 3.2, the magnetic field $\vec{B}$ can be obtained from

$$\vec{B} = \vec{\nabla} \times \vec{A} = \begin{vmatrix} \hat{i} & \hat{j} & \hat{k} \\ \frac{\partial}{\partial x} & \frac{\partial}{\partial y} & \frac{\partial}{\partial z} \\ A_x & A_y & A_z \end{vmatrix}$$

$$= \left\{ \frac{\partial A_z}{\partial y} - \frac{\partial A_y}{\partial z} \right\} \hat{i} + \left\{ \frac{\partial A_x}{\partial z} - \frac{\partial A_z}{\partial x} \right\} \hat{j} + \left\{ \frac{\partial A_y}{\partial x} - \frac{\partial A_x}{\partial y} \right\} \hat{k} \qquad (3.15)$$

In order to facilitate numerical solutions, the partial derivative can be approximated by a finite difference formula (Fröberg, 1964)

$$\frac{\partial A_z}{\partial y} \simeq \frac{\Delta A_z}{\Delta y} \simeq \frac{A_z(x_0, y_1, z_0) - A_z(x_0, y_{-1}, z_0)}{y_1 - y_{-1}} \qquad (3.16)$$

Equation 3.16 is the central difference for the partial derivative of A_z with respect to y at the point $\vec{r}_0 = (x_0, y_0, z_0)$ as shown in Figure 3.2. Similar expressions can be derived for other partial derivatives.

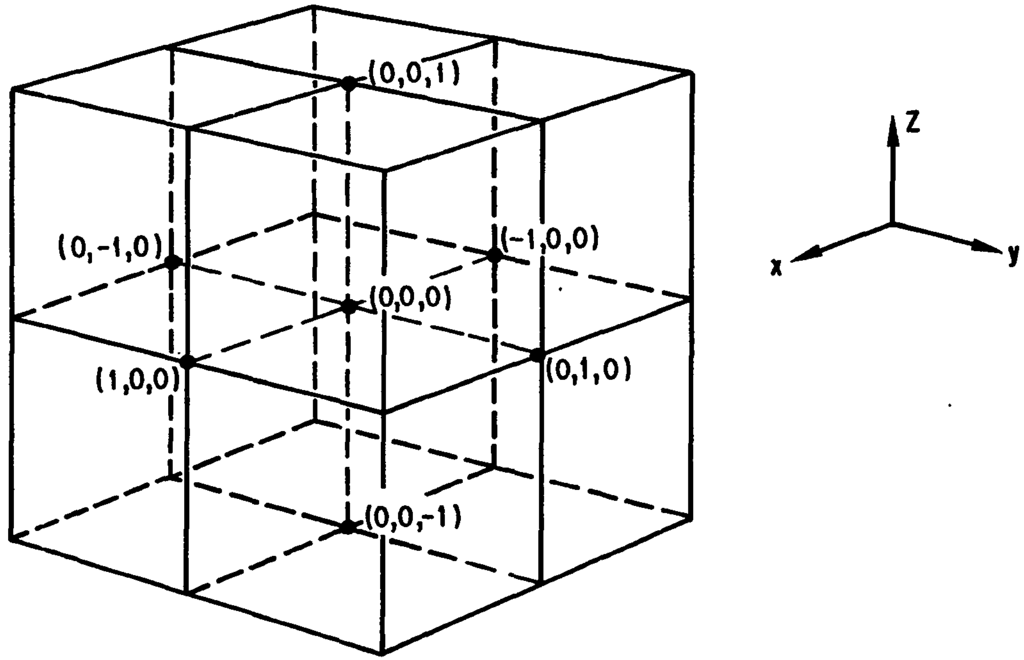

Figure 3.2 Six neighboring points around the field point. For example, in order to calculate $\vec{B}$ field at (0, 0, 0), the values of $\vec{A}$ field at the six neighboring points shown are needed.

Therefore the components of the magnetic field can be calculated from the following expressions

$$B_x(\vec{r}_0, t) \cong \left\{ \frac{A_z(x_0, y_1, z_0; t) - A_z(x_0, y_{-1}, z_0; t)}{(y_1 - y_{-1})} \right\}$$

$$- \left\{ \frac{A_y(x_0, y_0, z_1; t) - A_y(x_0, y_0, z_{-1}; t)}{(z_1 - z_{-1})} \right\} \qquad (3.17a)$$

$$B_y(\vec{r}_0, t) \cong \left\{ \frac{A_x(x_0, y_0, z_1; t) - A_x(x_0, y_0, z_{-1}; t)}{(z_1 - z_{-1})} \right\}$$

$$- \left\{ \frac{A_z(x_1, y_0, z_0; t) - A_z(x_{-1}, y_0, z_0; t)}{(x_1 - x_{-1})} \right\} \qquad (3.17b)$$

$$B_z(\vec{r}_0, t) \cong \left\{ \frac{A_y(x_1, y_0, z_0; t) - A_y(x_{-1}, y_0, z_0; t)}{(x_1 - x_{-1})} \right\}$$

$$- \left\{ \frac{A_x(x_0, y_1, z_0; t) - A_x(x_0, y_{-1}, z_0; t)}{(y_1 - y_{-1})} \right\} \qquad (3.17c)$$

In order to calculate $\vec{B}(\vec{r}_0, t)$, one needs to calculate the vector potential $\vec{A}$ at six neighboring field points.

3.2.3 Scalar Potential

According to Equation 3.5

$$\frac{\partial \phi}{\partial t} = -c^2 \vec{\nabla} \cdot \vec{A}$$

If both sides are integrated from 0 to t, one gets

$$\phi(\vec{r}_0, t) - \phi(\vec{r}_0, 0) = -c^2 \int_0^t \vec{\nabla} \cdot \vec{A} \, dt' \qquad (3.18)$$

The integration on the right-hand side can be approximated by an equivalent summation. This is done by subdividing the time t into M intervals. Each time interval $\Delta t_j = \frac{t}{M}$ should be chosen such that it is much less than the time required for the radiation from the current source to reach the field point. Therefore Δt_j should be selected according to the range between the field point and the lightning channel. Also Δt_j should be of the same order of magnitude as $\frac{\Delta \ell_i}{v}$, which was discussed in Section 3.2.1.

The integrand in Equation 3.18 at any time t_j can be written as

$$(\vec{\nabla} \cdot \vec{A})_j = \left(\frac{\partial A_x}{\partial x} + \frac{\partial A_y}{\partial y} + \frac{\partial A_z}{\partial z}\right)_j \tag{3.19}$$

Using the same finite difference approximation for the partial derivatives as before, the above equation becomes

$$(\vec{\nabla} \cdot \vec{A})_j \cong \left\{\frac{A_x(x_1, y_0, z_0; t_j) - A_x(x_{-1}, y_0, z_0; t_j)}{(x_1 - x_{-1})}\right\}$$

$$+ \left\{\frac{A_y(x_0, y_1, z_0; t_j) - A_y(x_1, y_{-1}, z_0; t_j)}{(y_1 - y_{-1})}\right\}$$

$$+ \left\{\frac{A_z(x_0, y_0, z_1; t_j) - A_z(x_0, y_0, z_{-1}; t_j)}{(z_1 - z_{-1})}\right\}$$

Here again, one needs to know the vector potential $\vec{A}$ at six neighboring points in order to obtain $(\vec{\nabla} \cdot \vec{A})_j$. Finally, the scalar potential ϕ at $\vec{r}_0$ is calculated from

$$\phi(\vec{r}_0, t) = \phi(\vec{r}_0, 0) - c^2 \sum_{j=1}^{M} (\vec{\nabla} \cdot \vec{A})_j \, \Delta t_j \tag{3.21}$$

where $\phi(\vec{r}_0, 0)$ is the initial value of the scalar potential just before the onset of the lightning return stroke.

3.2.4 Electric Field

According to Equation 3.1, the electric field change during a lightning return stroke is given by

$$\vec{E} = -\vec{\nabla}\phi - \frac{\partial \vec{A}}{\partial t}$$

$$= \left\{ -\frac{\partial \phi}{\partial x} - \frac{\partial A_x}{\partial t} \right\} \hat{i} + \left\{ -\frac{\partial \phi}{\partial y} - \frac{\partial A_y}{\partial t} \right\} \hat{j} + \left\{ -\frac{\partial \phi}{\partial z} - \frac{\partial A_z}{\partial t} \right\} \hat{k} \tag{3.22}$$

Again using finite difference approximations for the partial derivatives, one can calculate the electric field components at $\vec{r}_0$ as follows:

$$E_x(\vec{r}_0, t) = -\left\{ \frac{\phi(x_1, y_0, z_0; t) - \phi(x_{-1}, y_0, z_0; t)}{(x_1 - x_{-1})} \right\} - \left\{ \frac{A_x(x_0, y_0, z_0; t_1) - A_x(x_0, y_0, z_0; t_{-1})}{(t_1 - t_{-1})} \right\} \tag{3.23a}$$

$$E_y(\vec{r}_0, t) = -\left\{ \frac{\phi(x_0, y_1, z_0; t) - \phi(x_0, y_{-1}, z_0; t)}{(y_1 - y_{-1})} \right\} - \left\{ \frac{A_y(x_0, y_0, z_0; t_1) - A_y(x_0, y_0, z_0; t_{-1})}{(t_1 - t_{-1})} \right\} \tag{3.23b}$$

$$E_z(\vec{r}_0, t) = - \left\{\frac{\phi(x_0, y_0, z_1; t) - \phi(x_0, y_0, z_{-1}; t)}{(z_1 - z_{-1})}\right\}$$

$$- \left\{\frac{A_z(x_0, y_0, z_0; t_1) - A_z(x_0, y_0, z_0; t_{-1})}{(t_1 - t_{-1})}\right\} \quad (3.23c)$$

Notice that in order to obtain $\vec{E}(\vec{r}_0, t)$, one needs to calculate ϕ at six neighboring points plus $\vec{A}$ at two different time steps.

3.3 Computer Code Development and Verification

Based on the mathematical algorithms and numerical solutions discussed in previous sections, a FORTRAN IV computer code called EMFIELD was developed to calculate electromagnetic field changes during lightning return strokes. This code was initially developed for the SEL computer at NSSL and later revised for implementation on the IBM 370/3033 computers at Argonne National Laboratory (ANL). A detailed flow chart, a complete listing, and sample input instructions of the EMFIELD code are given in Appendix II.

This code allows a user to input the lightning channel geometries and return stroke current models. The user also chooses the length of the channel segment $\Delta\ell$ for integration, the time interval Δt for field evaluation, and the distance (Δx, Δy, Δz) between neighboring field points for spatial derivatives. The code calculates the z-component of the electric field. Plotting capability using the DISSPLA proprietary software package (1978) is also provided for the user to obtain graphic outputs for both channel geometries and electric field waveforms.

Extensive tests have been conducted with this code with two main objectives in mind. The first objective is to establish confidence in this code by comparing the results with other calculations in the literature. The second objective is to gain more insight into the fundamental characteristics of the models for lightning return strokes by varying model parameters systematically.

3.3.1 Numerical Stability and Solution Accuracy

The mathematical algorithm adapted in the EMFIELD code involves numerical integration and differentiation. The stability and accuracy of solutions are dictated by the mesh sizes of time and space. The channel segment length $\Delta \ell$ is used in the integration of the current pulse propagating along the lightning channel. The distance (Δx, Δy, Δz) between the field point and its six neighboring points are used in the evaluation of $\vec{\nabla} \cdot \vec{A}$ and $\vec{\nabla}\phi$. The time step size Δt is used in the integration of $\vec{\nabla} \cdot \vec{A}$ and the differentiation of $\vec{A}$. It is expected that the finer the mesh sizes are, the better the solution accuracy will be. However, since the amount of computation time increases rapidly as the mesh sizes decrease, careful selection of optimal mesh sizes must be made in order to keep the computing cost at a reasonable level and still obtain acceptable solutions.

A simple problem, originally solved by LeVine and Meneghini (1978), was chosen for this test. The lightning channel is assumed to be a vertical straight line 6 km long over a conducting ground plane. The current pulse propagates up the channel with the speed of light, and its waveform is described by a compound exponential model,

$$I(t) = I_0 \, [e^{-\alpha t} - e^{-\beta t}] + I_1 \, [e^{-\delta t} - e^{-\delta t}] \qquad (3.24)$$

where, for a typical return stroke, the parameters are $\alpha = 2.0 \times 10^4 \ s^{-1}$, $\beta = 2.0 \times 10^5 \ s^{-1}$, $\delta = 1.0 \times 10^3 \ s^{-1}$, $\delta = 2.0 \times 10^4 \ s^{-1}$, $I_0 = 30$ kA, and $I_1 = 2.5$ kA (Uman, 1969). This current waveform is shown in Figure 3.3.

Calculations of the electric field at a field point 1 km from the channel with three sets of different mesh sizes were performed, and the results are shown in Figure 3.4. Quite large oscillations are observed in the case of coarse mesh sizes ($\Delta t = 0.5$ µs, $\Delta \ell = 20$ m, $\Delta z = 5$ m). These oscillations are caused by the inaccuracy of numerical integration and differentiation involved in the calculation. As shown in the same figure, these oscillations are reduced to small ripples when the mesh intervals are reduced to medium sizes ($\Delta t = 0.1$ µs, $\Delta \ell = 10$ m, $\Delta z = 3$ m). At fine mesh sizes ($\Delta t = 0.05$ µs, $\Delta \ell = 5$ m, $\Delta z = 3$ m), the oscillations are completely suppressed, and the solution becomes a smooth curve as it should be. The computing time roughly doubles when $\Delta \ell$ or Δt reduces to half its size. For the case of medium mesh size in Figure 3.4, it took 3 min of CPU time on ANL's IBM 3330 computer.

Numerical stability and solution accuracy are further influenced by the range between the field point and the channel, the speed of current propagation, and the waveform of the current model. These can be seen in Figures 3.5, 3.6, and 3.7 where all cases were calculated with medium mesh sizes except Δz was changed to 5 m. It will be seen later that when the current rise time is very short, as in the model of Lin et al. (1980), further reduction in $\Delta \ell$ is necessary.

Selection of the spatial mesh (Δx, Δy, Δz) is somewhat tricky. The mesh cannot be too large because it will yield inaccurate results

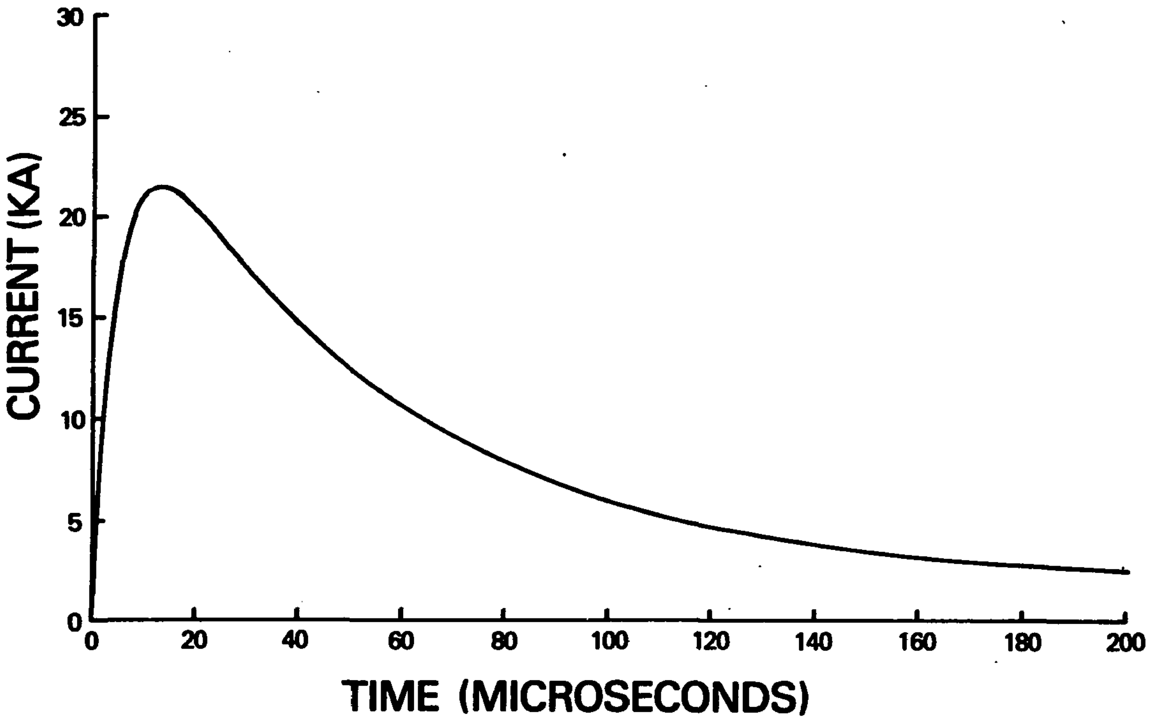

Figure 3.3 The compound exponential current waveform for benchmark problem set 1 (after LeVine and Meneghini, 1978).

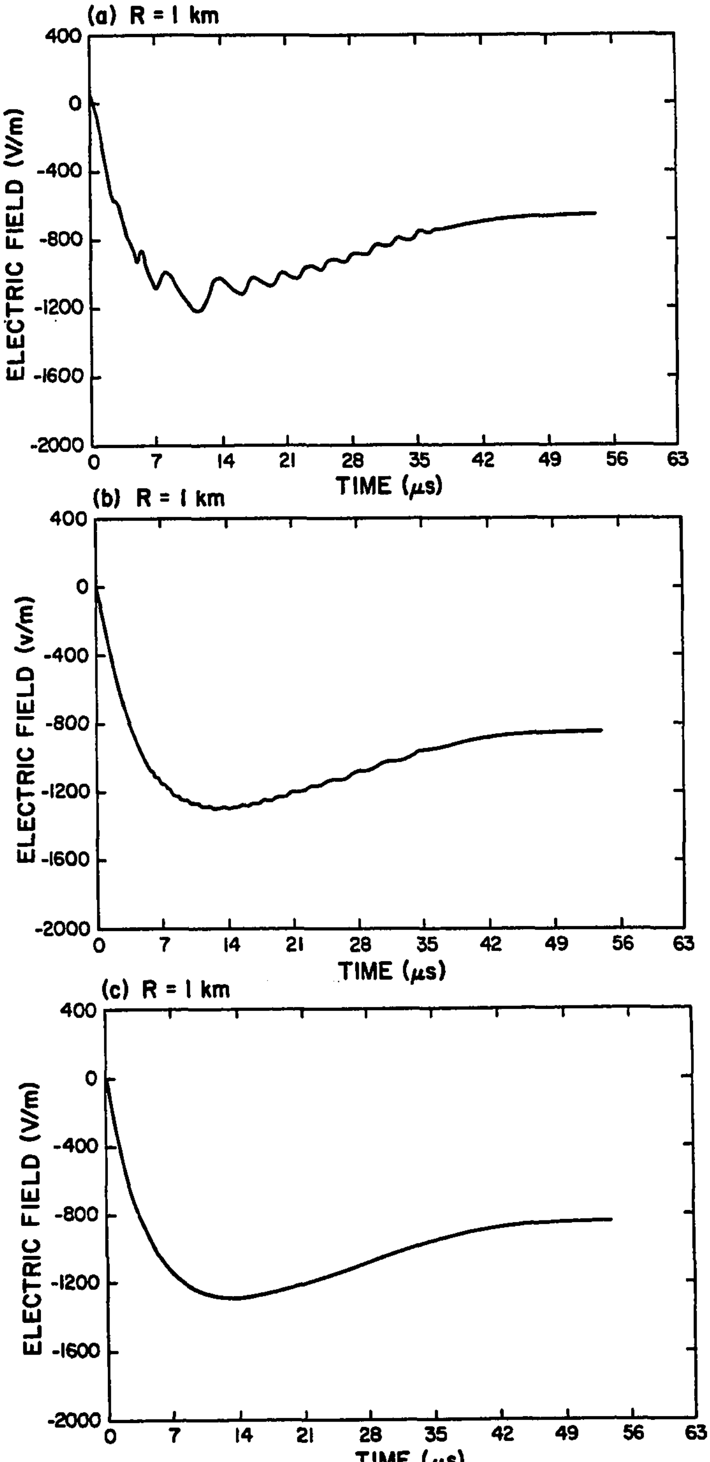

Figure 3.4 Calculated radiation waveforms with the compound exponential current model using 3 sets of mesh sizes: a) Large mesh ($\Delta t = 0.5$ μs, $\Delta \ell = 20$ m, $\Delta z = 5$ m); b) Medium mesh ($\Delta t = 0.1$ μs, $\Delta \ell = 10$ m, $\Delta z = 3$ m); c) Fine mesh ($\Delta t = 0.05$ μs, $\Delta \ell = 5$ m, $\Delta z = 3$ m)

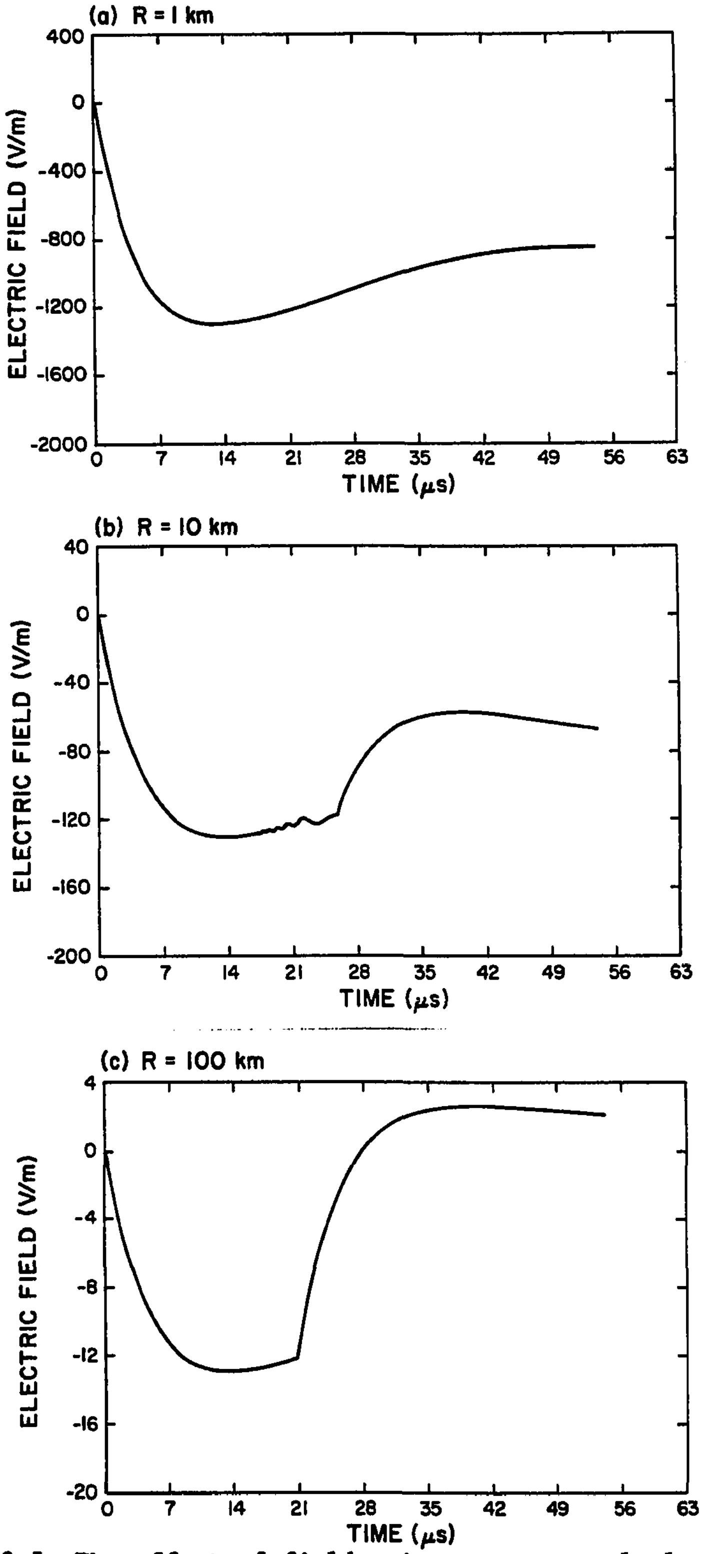

Figure 3.5 The effect of field point range on calculated radiation waveforms using medium mesh sizes at three ranges: a) R = 1 km, b) R = 10 km, and c) R = 100 km.

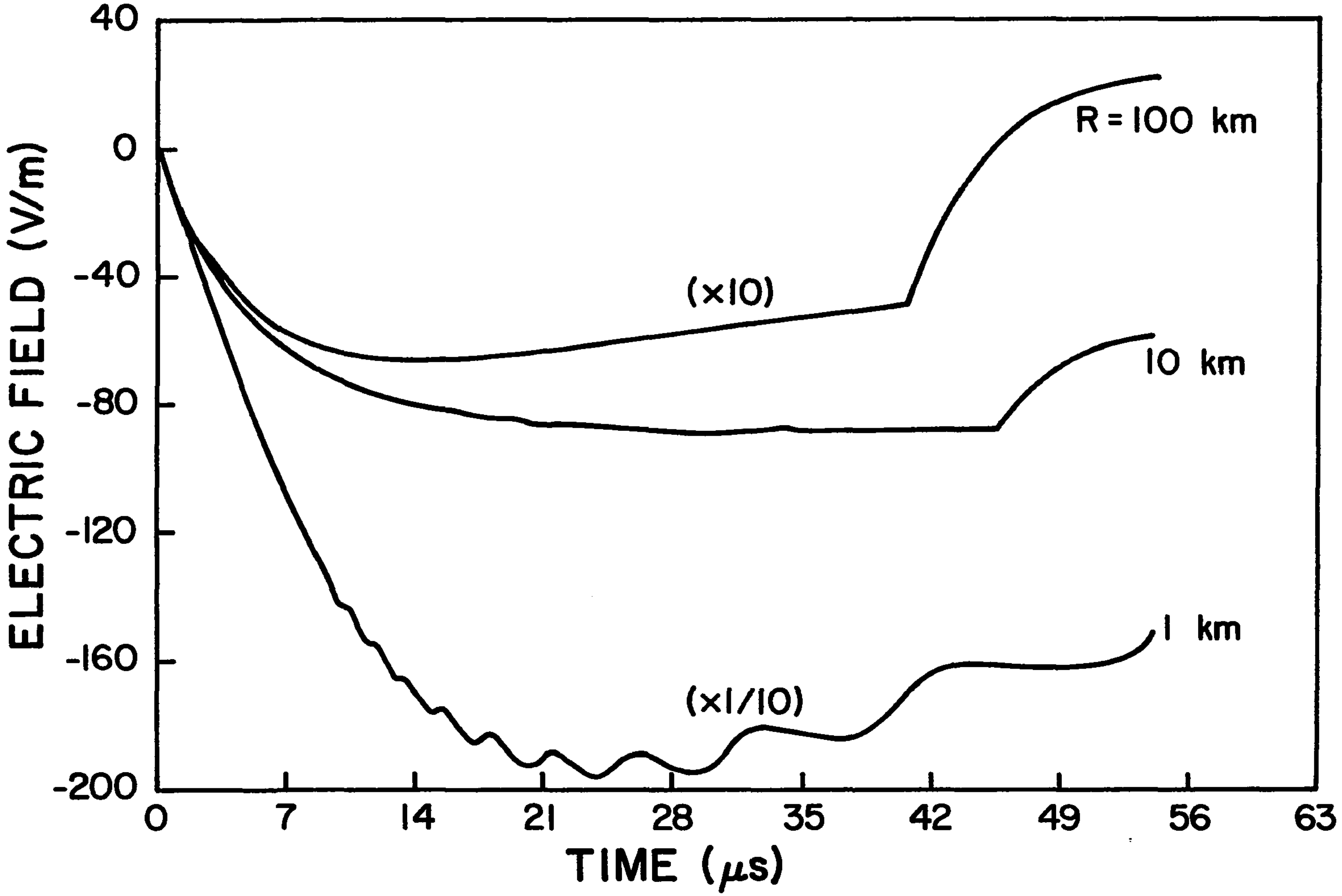

Figure 3.6 The effect of propagation speed on calculated radiation waveforms using medium mesh sizes and v = c/2. A vertical scaling factor of 1/10 and 10 is used to show the result for R = 1 km and R = 100 km, respectively. The actual value has been multiplied by the scaling factor and then plotted.

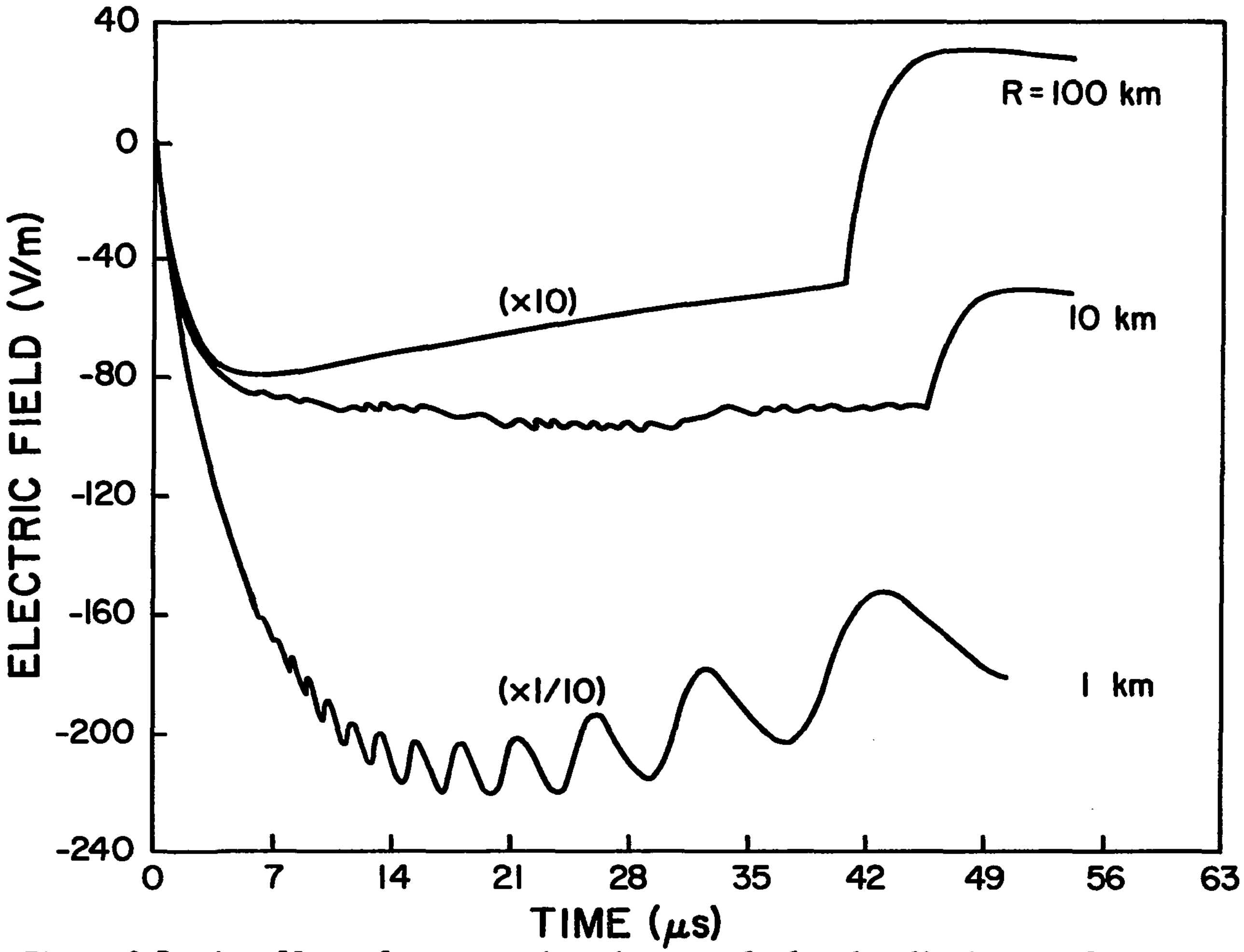

Figure 3.7 The effect of current rise time on calculated radiation waveforms using medium mesh sizes and the current rise time is reduced to half of its original value.

for differentiation. On the other hand, it cannot be made too small because the vector potential $\vec{A}$ and the scalar potential ϕ at two neighboring points will have almost equal values. Since the IBM 3330 system can only keep 14 significant figures, it is possible that when two nearly identical numbers are substracted, the result will be very inaccurate. When the spatial mesh size was smaller than a certain minimum value, step jumps in the calculated electric field were found. Therefore, it is prudent to consider all the variables discussed here in order to select a set of optimal mesh sizes for a given problem.

3.3.2 Benchmark Problem Set 1: LeVine and Meneghini

In order to verify the EMFIELD code, two problems solved by LeVine and Meneghini (1978) were chosen as benchmarks. The first one is the example in Section 3.3.1 used for the numerical stability and accuracy analyses. The second one is the same as the first except the channel geometry is tortuous instead of straight. Exact solutions of the electric fields radiated by an arbitrarily oriented current-carrying filament over a conducting ground plane were presented by them. In their solutions, no mathematical approximations were made, and the final results exist in closed form in terms of elementary functions. The solutions satisfy both Maxwell's equations and the necessary boundary conditions. Therefore, the validity of the EMFIELD code can be demonstrated by comparison of the numerical results with the exact solutions. Figure 3.8 shows the channel geometries and the exact solutions of the electric fields for these two problems taken directly from LeVine and Meneghini. The physical interpretation of these results will be

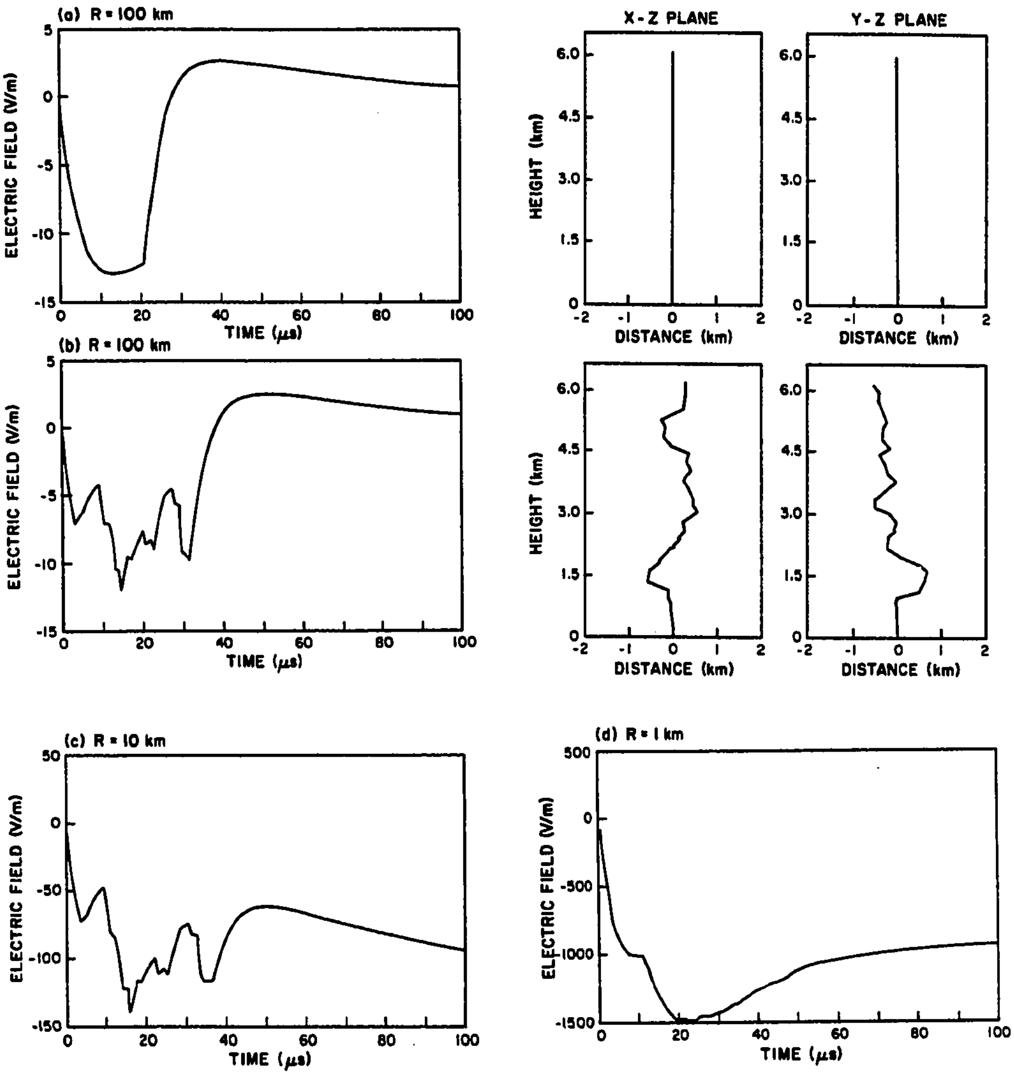

Figure 3.8 The analytical solutions of radiated electric fields and their corresponding channel geometries for benchmark problem set 1 (after LeVine and Meneghini, 1978). R is the range from the field point to the ground strike point. The top panel pertains to a straight channel, and the lower two panels pertain to a torturous channel.

deferred until Chapter IV. Figure 3.9 shows the equivalent numerical solutions obtained from EMFIELD. Note that the tortuous channel geometry used in the numerical calculations was reproduced as closely as possible from Figure 3.8. Although minor differences exist in this second benchmark solution, in essence, total agreement is found between the two methods.

3.3.3 Benchmark Problem Set 2: Master et al.

In order to reproduce the electric and magnetic fields measured simultaneously at two ground stations, Lin et al. (1980) introduced a new lightning return stroke model, which is much more complex than the compound exponential transmission line model used previously. Their model is composed of three separate current components: (1) a short-duration upward-propagating pulse of current $I_b(z, t)$ with constant amplitude, waveshape, and velocity associated with the electrical breakdown at the return stroke wavefront, (2) a uniform current I_u that may already be flowing (leader current) or may start to flow soon after the return stroke begins; and (3) a corona current $I_c(z, t)$ caused by the radially inward and then downward movement of the charge initially stored in the corona sheath around the leader channel. An example of these three current components for a typical subsequent return stroke is illustrated in Figure 3.10. The salient features of a breakdown pulse current are the following: it increases from 0 to 3 kA in 1.0 μs, is followed by a fast transition to a peak value of 14.9 kA at 1.1 μs, and is down to half value at 3.8 μs and zero at 40 μs. The breakdown pulse current propagates upward with a speed $v = 1 \times 10^8$ m/s. The uniform

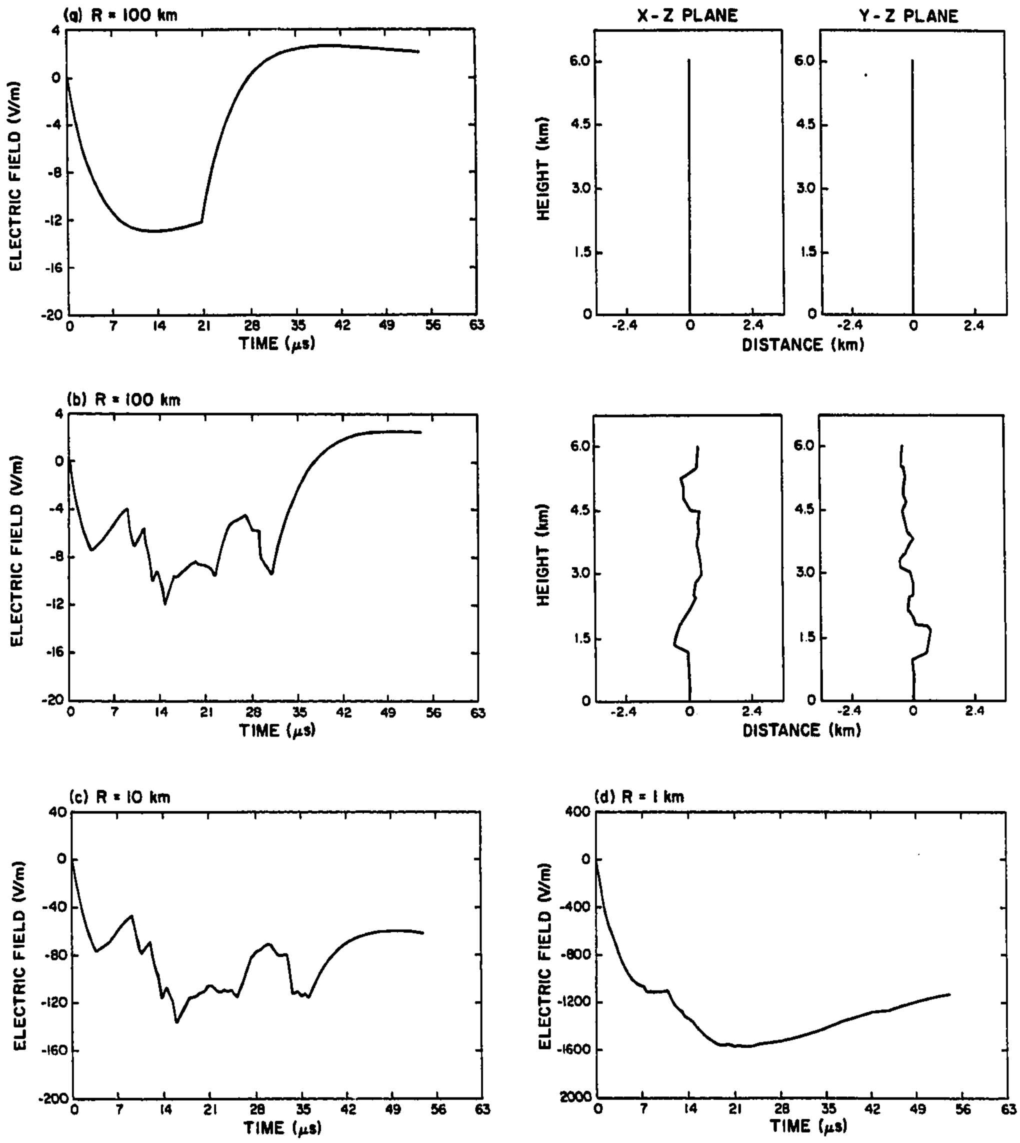

Figure 3.9 Reproduced channel geometries and calculated electric fields using the EMFIELD code for benchmark problem set 1.

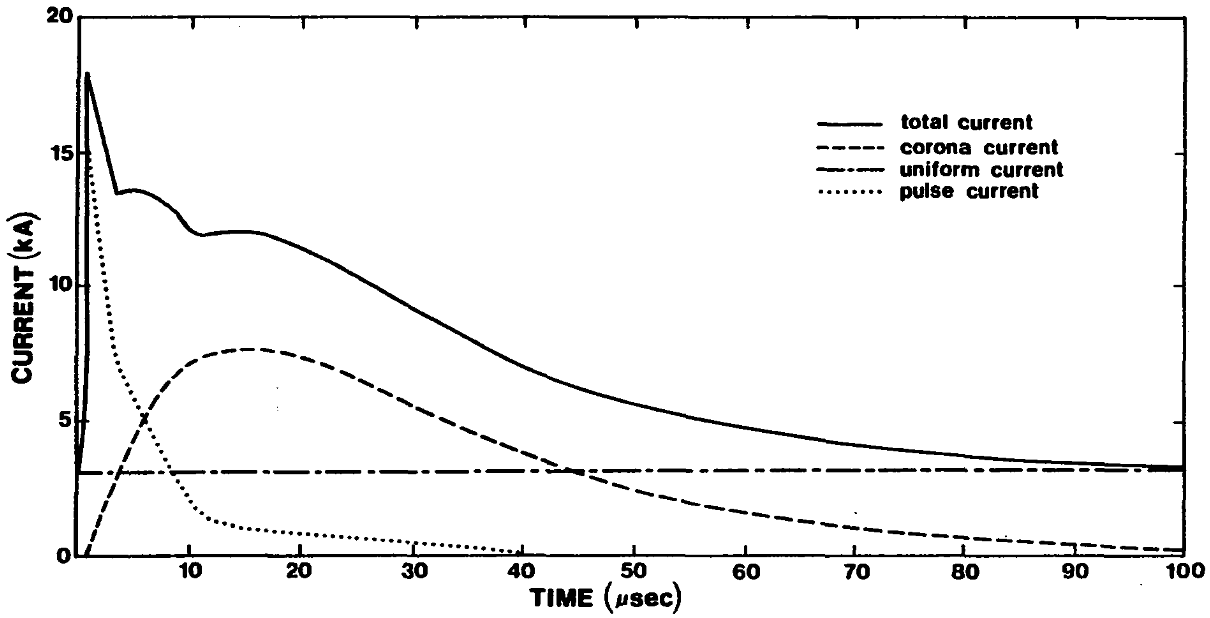

Figure 3.10 Total current and its three components at ground in the modified current model of Lin, et al. for a typical subsequent return stroke (after Master et al., 1981).

current is assumed to be 3.1 kA in this example. The corona current injected per meter of channel at z' is

$$I_c\ (z',\ t) = I_1\ e^{-z'/\lambda}\ (e^{-\alpha' t} - e^{-\beta' t}) \tag{3.25}$$

where $I_1 = 21$ A/m, $\lambda = 1.5$ km, $\alpha' = 10^5\ s^{-1}$, $\beta' = 3 \times 10^6\ s^{-1}$, and t is the time after the corona current is turned on by the peak breakdown pulse wavefront. The corona current at a height z due to all corona sources above it is calculated by integrating I (z', t) with respect to z' from z to H. The result is:

$$I_c\ (z,\ t) = \frac{I_1}{\frac{\alpha}{v} + \frac{\alpha}{c} - \frac{1}{\lambda}}\ e^{-\alpha'\ (t - t_{on} - \frac{z}{c})} \left[e^{(\frac{\alpha'}{v} + \frac{\alpha'}{c} - \frac{1}{\lambda})\ z_m} - e^{(\frac{\alpha'}{v} + \frac{\alpha'}{c} - \frac{1}{\lambda})\ z} \right] - \frac{I_1}{\frac{\beta}{v} + \frac{\beta}{c} - \frac{1}{\lambda}}\ e^{-\beta'\ (t - t_{on} + \frac{z}{c})} \left[e^{(\frac{\beta'}{v} + \frac{\beta'}{c} - \frac{1}{\lambda})\ z_m} - e^{(\frac{\beta'}{v} + \frac{\beta'}{c} - \frac{1}{\lambda})\ z} \right] \tag{3.26}$$

where $z_m = \dfrac{t - t_{on} + \frac{z}{c}}{\frac{1}{v} + \frac{1}{c}}$ is the maximum height above which there is no corona current source, and t_{on} (= 1.1 μs) is the time interval between the initiation of corona current and the peak of the breakdown pulse current.

The original model of Lin et al. (1978) predicts a field change of opposite polarity to that of the initial field when the breakdown pulse reaches the top of the channel. This "mirror image" field change is rarely observed, and it may not be realistic.

Furthermore, Jorden and Uman (1980) have shown that initial-peak luminosity in subsequent strokes varies markedly with height, decreasing to half value about 1 km above ground. Therefore, Master et al. (1981) subsequently proposed a modification to the original model by allowing the breakdown pulse current to decrease with height above the ground. Thus in this benchmark problem set, the amplitude of the breakdown pulse current is assumed to decrease exponentially with height at exactly the same rate as the corona current. The channel is assumed to be a vertical straight line of length 7.5 km in all cases here. Figure 3.11 shows the results of four calculated vertical electric fields for a typical subsequent return stroke using the modified current model of Lin et al.

In order to facilitate the numerical calculations of the benchmark problems shown in Figure 3.11 using EMFIELD, the breakdown pulse current is modeled analytically as a double exponential waveform

$$I_b (z, t) = I_0 e^{-z/\lambda} [e^{-\alpha t} - e^{-\beta t}] \tag{3.27}$$

with $I_0 = 25$ kA, $\alpha = 3.2 \times 10^5$ s^{-1}, $\beta = 2 \times 10^6$ s^{-1}, and $\lambda = 1.5$ km. These were chosen to yield a waveform closely matching the original current waveshape. This waveform rises to its peak value of 14.81 kA by 1.09 μs and decays to half-peak value at 3.8 μs. At 40 μs it is only 70 mA. The corona current and the uniform current are exactly those shown in Figure 3.10. The equivalent current model used for the benchmark problems are shown in Figure 3.12. Notice that there is a small difference in the breakdown current in Figures 3.10 and 3.12. Figure 3.13 shows the results obtained with EMFIELD for the four vertical electric fields corresponding to those shown in Figure 3.10. Although

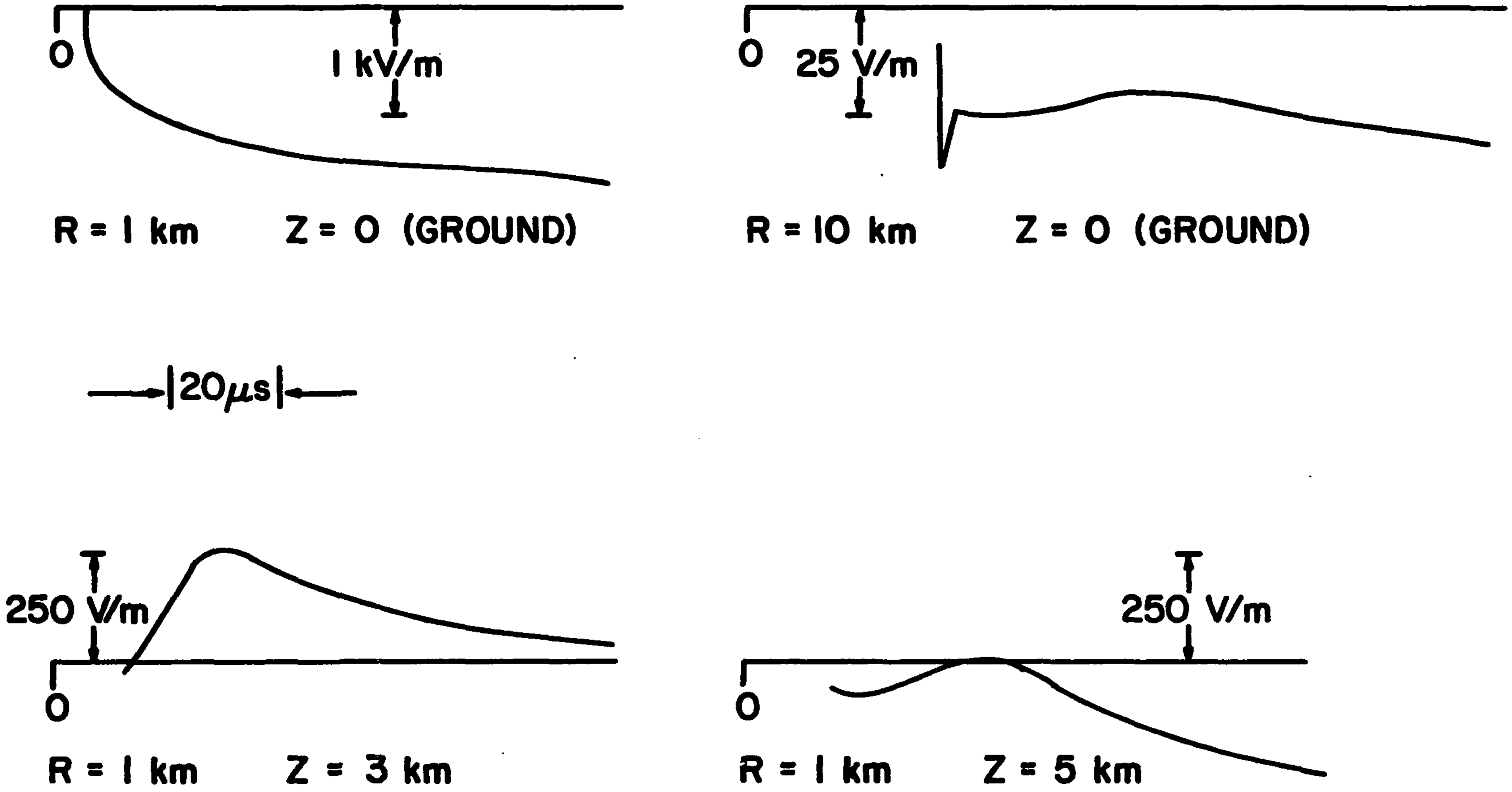

Figure 3.11 Electric fields at ground and above ground calculated for benchmark problem set 2 by Master et al. (1981).

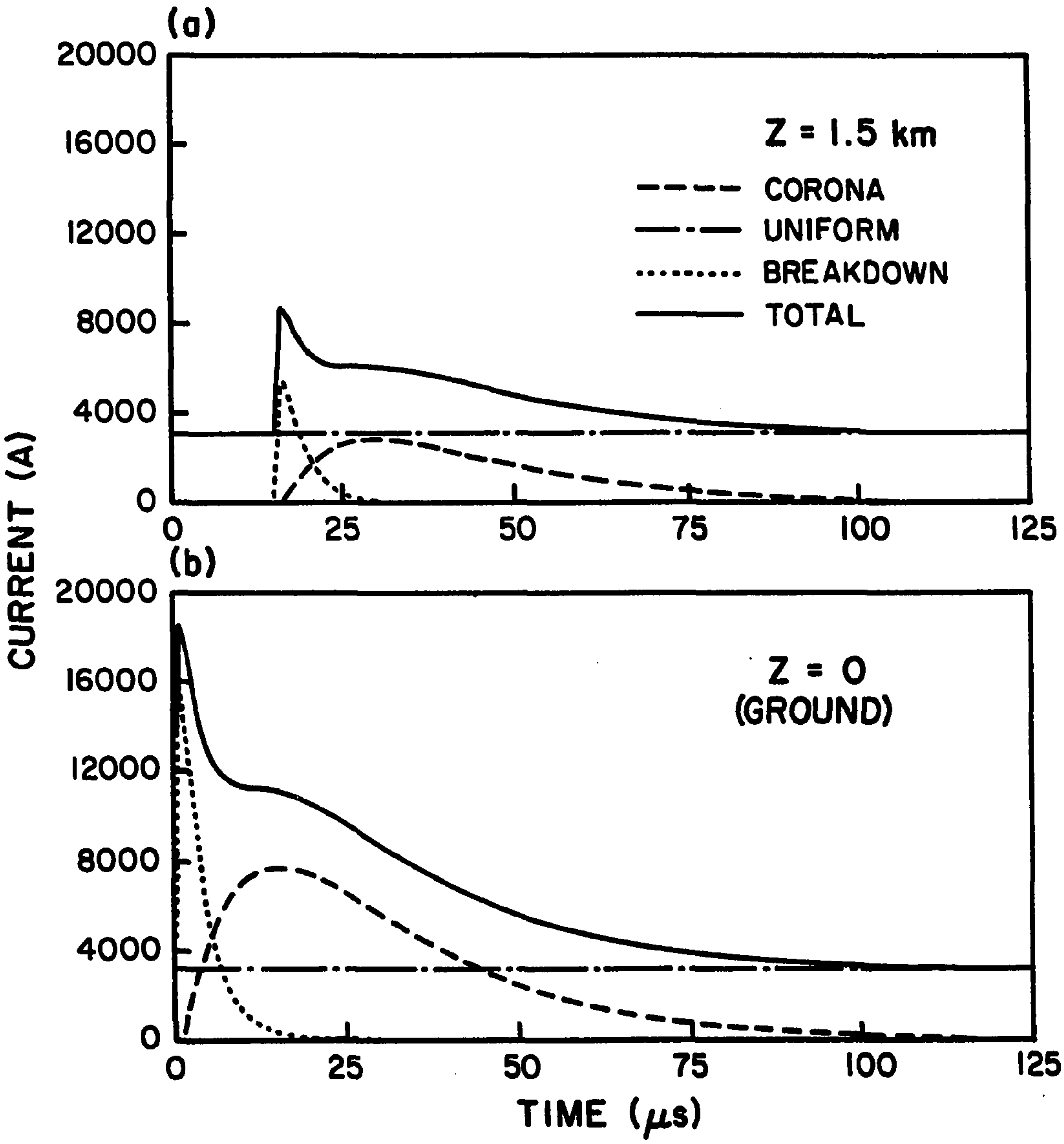

Figure 3.12 Modified current model of Lin et al. used in EMFIELD solutions for benchmark problem set 2. Total current and its three components are shown for two heights: a) Z = 1.5 km above ground, b) Z = 0 km.

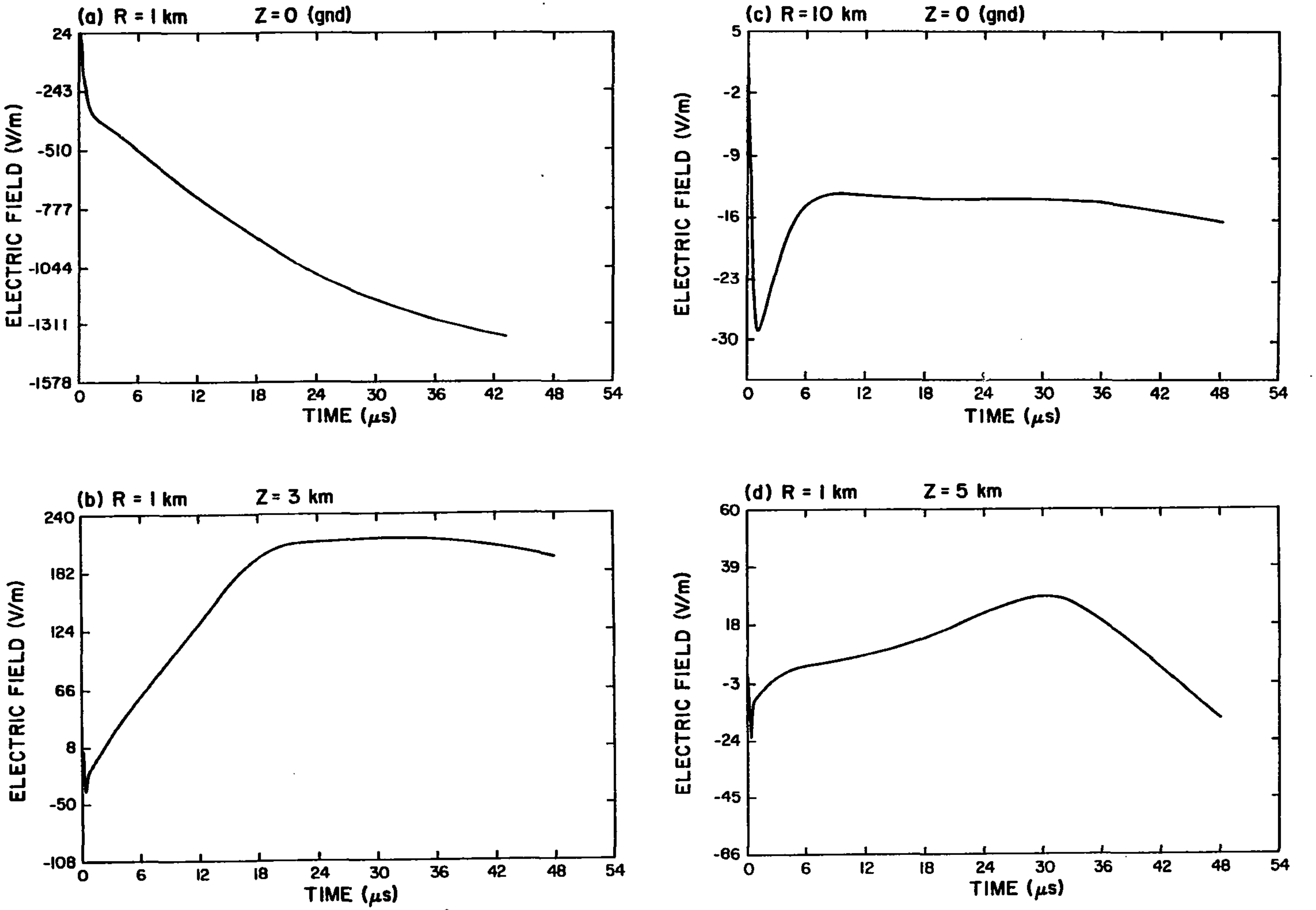

Figure 3.13 Calculated electric fields for benchmark problem set 2 using the EMFIELD code.

some minor mismatch between the results in Figures 3.11 and 3.13 can be seen and are due to the small difference between the breakdown currents, the overall agreement is excellent.

The validity of EMFIELD code is thus firmly established by these two sets of benchmark calculations. The versatility of this code makes it a very powerful tool for analyzing return stroke current models and the associated electromagnetic fields. The code is now ready to be used to study the impact of channel tortuosity on the electromagnetic fields radiated by lightning.

CHAPTER IV

EFFECTS OF CHANNEL TORTUOSITY ON THE CALCULATED ELECTRIC FIELD DURING RETURN STROKES

4.1 Introduction

Most analyses of electromagnetic radiations from lightning discharges have assumed simple lightning paths, such as linear or cylindrical vertical columns between the cloud and ground (Bruce and Golde, 1941; Uman and McLain, 1969; Lin et al., 1980). Such an idealized channel geometry simplified the analysis considerably, but the results have provided the basis for discussions of breakdown processes and modeling of return stroke currents. However, it is a common observation that the paths of lightning channels are almost always erratic and tortuous. Photographic evidence of this may be seen in Salanave (1980). Although calculations based on a linear channel can explain quite successfully the gross feature of some selective measured data, the failure of the model is expected in cases where the channel is very tortuous.

The erratic nature of the lightning path has been analyzed statistically by Hill (1968). The results indicate that a typical cloud-to-ground lightning channel appears to have the broad characteristic of a random walk problem in which the step length is a constant and the median direction is fixed. Hill used segment lengths of 5 to

70 m and total channel lengths of 1 to 4.3 km, and obtained a mean absolute value of the change in channel direction of approximately 16°. His conclusions imply that an average lightning path is generally tortuous and that higher frequency radiations will be generated by the rapidly oscillating horizontal component of current in a tortuous channel than by a vertical component in a linear channel.

More recently, a Monte Carlo simulation has been developed by LeVine and Meneghini (1978) to model radiations from lightning return strokes. The simulation employs a piecewise linear model for the channel and contains the assumption of a current pulse that propagates along the channel at constant speed. The simulation has been used to study the effect of tortuosity on the electric field radiated from return strokes. It was found that tortuosity tends to make the radiated waveforms less similar to the current pulse waveshape. The effect of tortuosity in the frequency domain is an increase in high frequency energy, and in the time domain it causes increased fluctuations in the electric field waveform. The magnitude of the increase in high frequency radiation depends on the mean length of the elements comprising the channel.

Even though the current model used by LeVine and Meneghini is simple and smooth (see Figure 3.3), the calculated ΔE waveform, when a tortuous channel is used, exhibits fine structure, which is comparable to that of a selected waveform for a first return stroke recorded at Kennedy Space Center. It is interesting to note that their approach is in great contrast to the one used by Lin et al. (1980). In order to fit two station field data obtained in Florida, Lin et al.

developed a complex current model using a simple, straight vertical channel. Each of these two approaches has its own merits, but they seem to have contradicted to each other. In order to adequately describe an actual radiated ΔE waveform that depends on both channel tortuosity and the current, it is important first to understand clearly the effects of tortuosity on calculated ΔE waveforms from different current models. A study incorporating simplified channel tortuosity was designed and conducted specifically for this purpose.

4.2 Designs of Simple Channel Tortuosity

All channel shapes designed for this study are simple deviations from a vertical line. The basic reason for using these designs is to gain an understanding of the impacts of the channel tortuosity by comparing the calculated electric field from both tortuous and vertical channels. Table 4.1 lists the coordinates of the seventeen simple, tortuous channels. Figure 4.1 illustrates the 17 channel geometries with the observer, i.e. the field point or measurement site, located on the x-axis at ranges R_0 of 1, 10, and 100 km from the ground strike point. All the tortuous channels are assumed to turn at a height of 3 km, with either the channel top or the turning point displaced horizontally by 3 km. An exception to these horizontal displacements and to a maximum height of 6 km is the double, vertical channel (ZD) whose top is at 12 km.

In an attempt to resolve the issues resulting from the work of LeVine and Meneghini and that of Lin et al., two current models were tested in this study. The first one is the compound exponential

TABLE 4.1. Coordinates for Ground Points, Turning Points, and Channel Tops of 17 Simple, Tortuous Channels. The 17 Simple Channels Reduce to 12 When Symmetry is Considered Symmetrical Channels are Shown in ( ).

Channel Type	Ground Point (km)			Turning Point (km)			Channel Top (km)		
	x	y	z	x	y	z	x	y	z
XP	0.0	0.0	0.0	-3.0	0.0	3.0	0.0	0.0	6.0
XM	0.0	0.0	0.0	3.0	0.0	3.0	0.0	0.0	6.0
YP(YM)	0.0	0.0	0.0	0.0	3.0 (-3.0)	3.0	0.0	0.0	6.0
XPYP(XPYM)	0.0	0.0	0.0	-3.0	3.0 (-3.0)	3.0	0.0	0.0	6.0
XMYM(XMYP)	0.0	0.0	0.0	3.0	-3.0 (3.0)	3.0	0.0	0.0	6.0
ZD	0.0	0.0	0.0	-	-	-	0.0	0.0	12.0
ZHXP	0.0	0.0	0.0	0.0	0.0	3.0	-3.0	0.0	6.0
ZHXM	0.0	0.0	0.0	0.0	0.0	3.0	3.0	0.0	6.0
ZHYP(ZHYM)	0.0	0.0	0.0	0.0	0.0	3.0	0.0	3.0 (-3.0)	6.0
XPZT	0.0	0.0	0.0	-	-	-	-3.0	0.0	6.0
XMZT	0.0	0.0	0.0	-	-	-	3.0	0.0	6.0
YPZT(YMZT)	0.0	0.0	0.0	-	-	-	3.0 (-3.0)	0.0	6.0

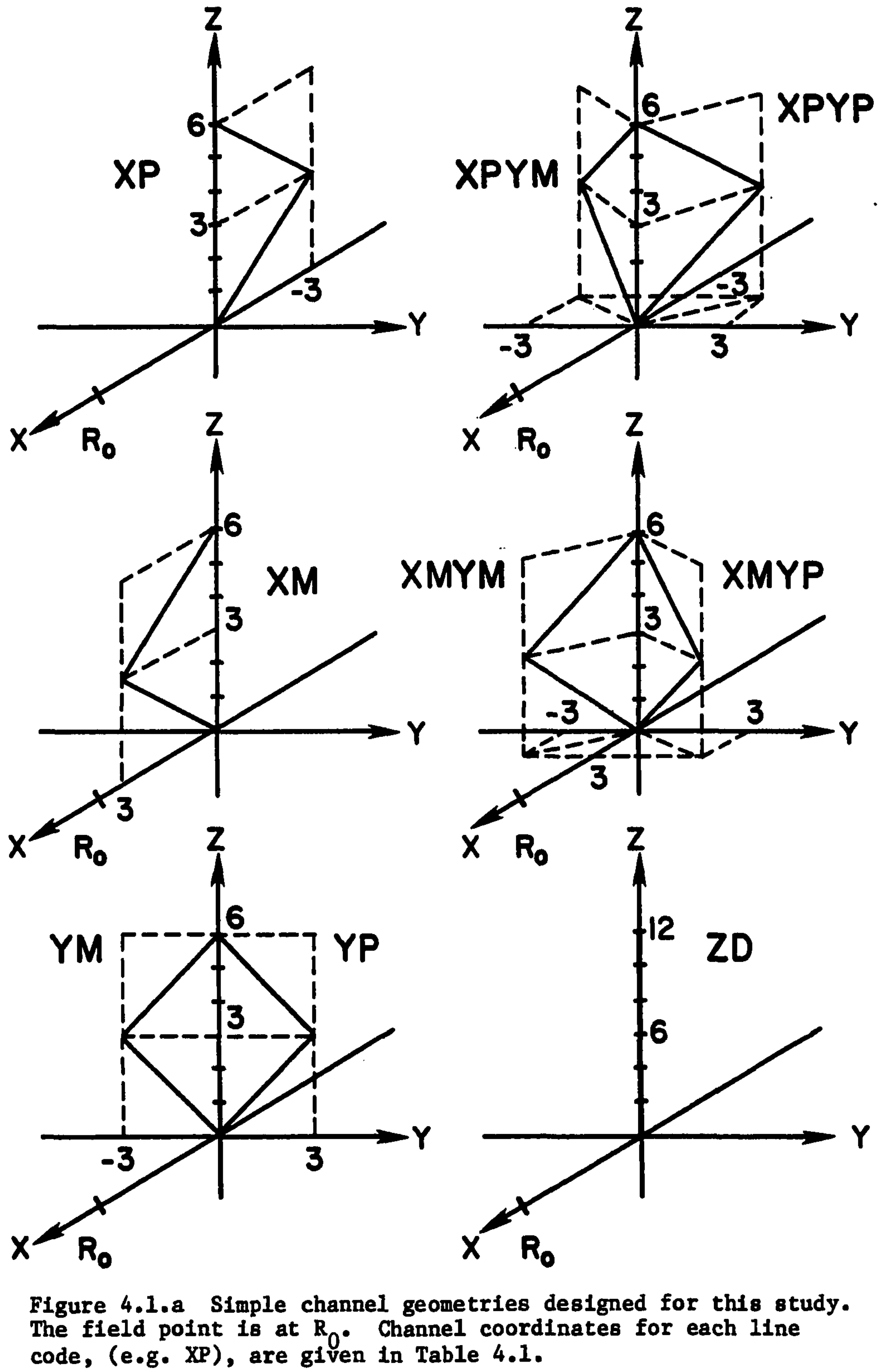

Figure 4.1.a Simple channel geometries designed for this study. The field point is at R_0. Channel coordinates for each line code, (e.g. XP), are given in Table 4.1.

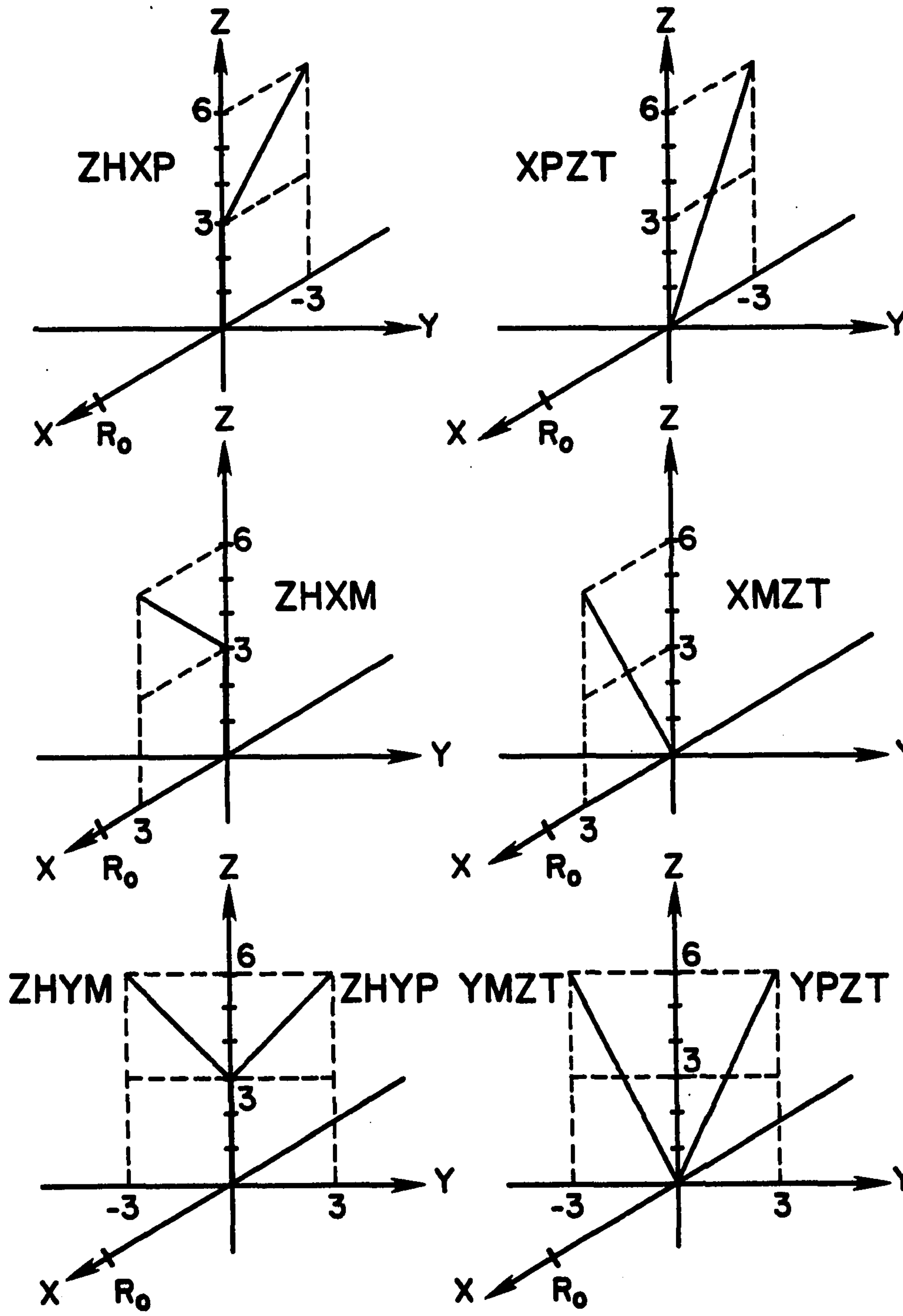

Figure 4.1.b Simple channel geometries designed for this study. The field point is at R_0. Channel coordinates for each line code, (e.g. ZHXP), are given in Table 4.1.

transmission line model, which was discussed in the first benchmark problem (Figure 3.3). The second current model is the one described in the second benchmark problem (Figure 3.11). These two current models are characteristically different and were applied to 12 channel geometries (computations for the other five, symmetrical counterparts were not done). Radiated waveforms were calculated with the EMFIELD code.

4.3 Results

4.3.1 Compound Exponential Transmission Line Model

For this current model, the mesh sizes used in all calculations with EMFIELD were $\Delta t = 0.1$ μs, $\Delta \ell = 10$ m, and $\Delta z = 5$ m. Figure 4.2 shows the results of the reference case where the channel geometry is a vertical straight line 6 km high. Electric field waveforms at 1 km and 100 km are shown with a vertical scaling factor of 1/10 and 10, respectively. Results for the designed tortuous channels are shown in Figure 4.3.

According to the derivations in Chapter III, two abrupt changes in the calculated waveforms are associated, respectively, with the turning point at R_1 or the channel top at R_2 at times given by

$$t_1 = \frac{\ell_1}{v} + \frac{R_1}{c} - \frac{R_0}{c} \tag{4.1}$$

and

$$t_2 = \frac{\ell_2}{v} + \frac{R_2}{c} - \frac{R_0}{c} \tag{4.2}$$

where ℓ_1 is the channel length from the ground to the turning point, ℓ_2 is the channel length from ground to the channel top, R_1 is the distance

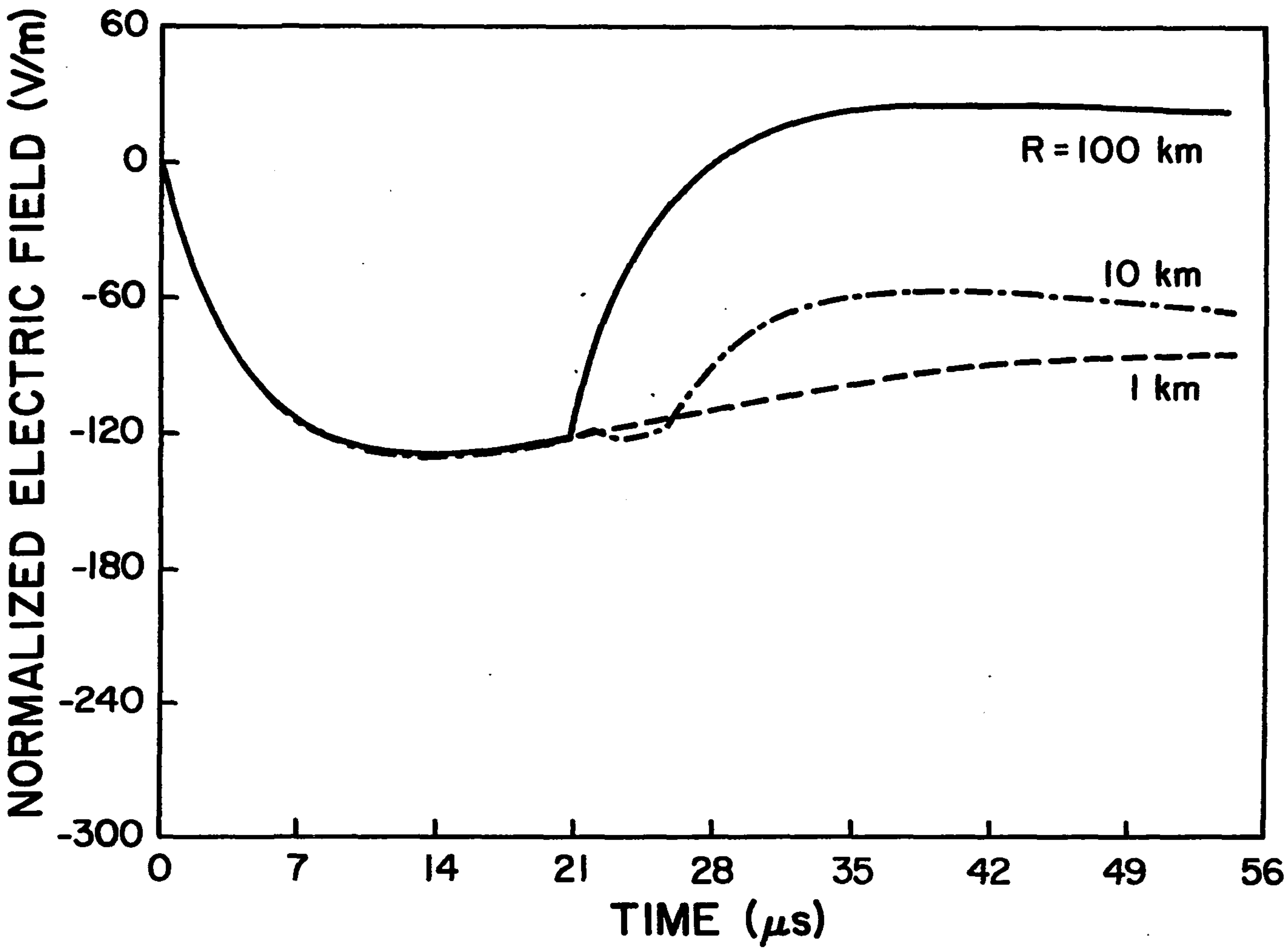

Figure 4.2 Reference case for compound exponential transmission line current model: calculated electric fields for a vertical channel 6 km high. A vertical scaling factor of 1/10 and 10 is used to show the electric fields at R = 1 km and R = 100 km, respectively.

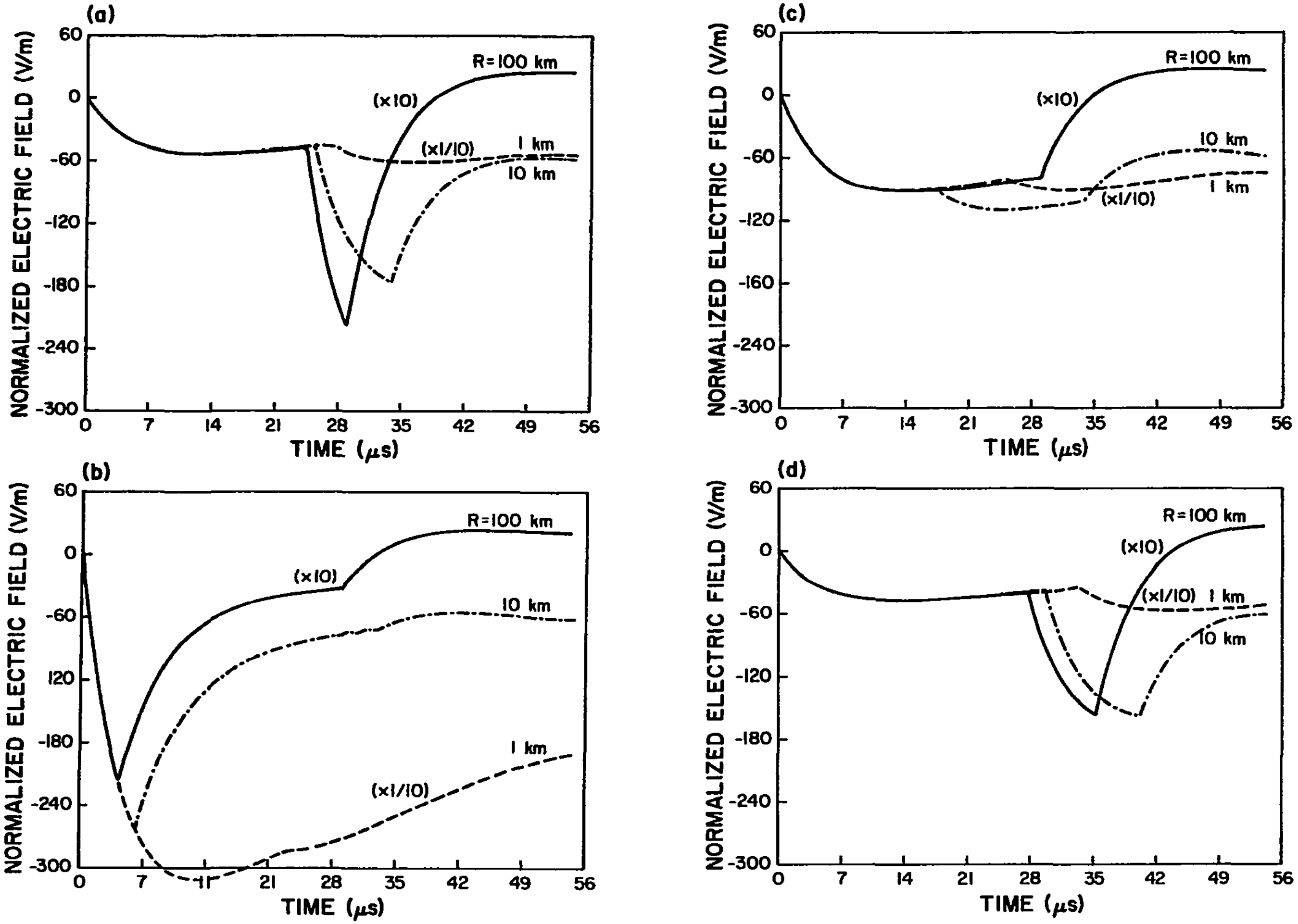

Figure 4.3.a Calculated electric fields for designed tortuous channels using compound exponential current model. a) XP, b) XM, c) YP(YM), and d) XPYP(XPYM).

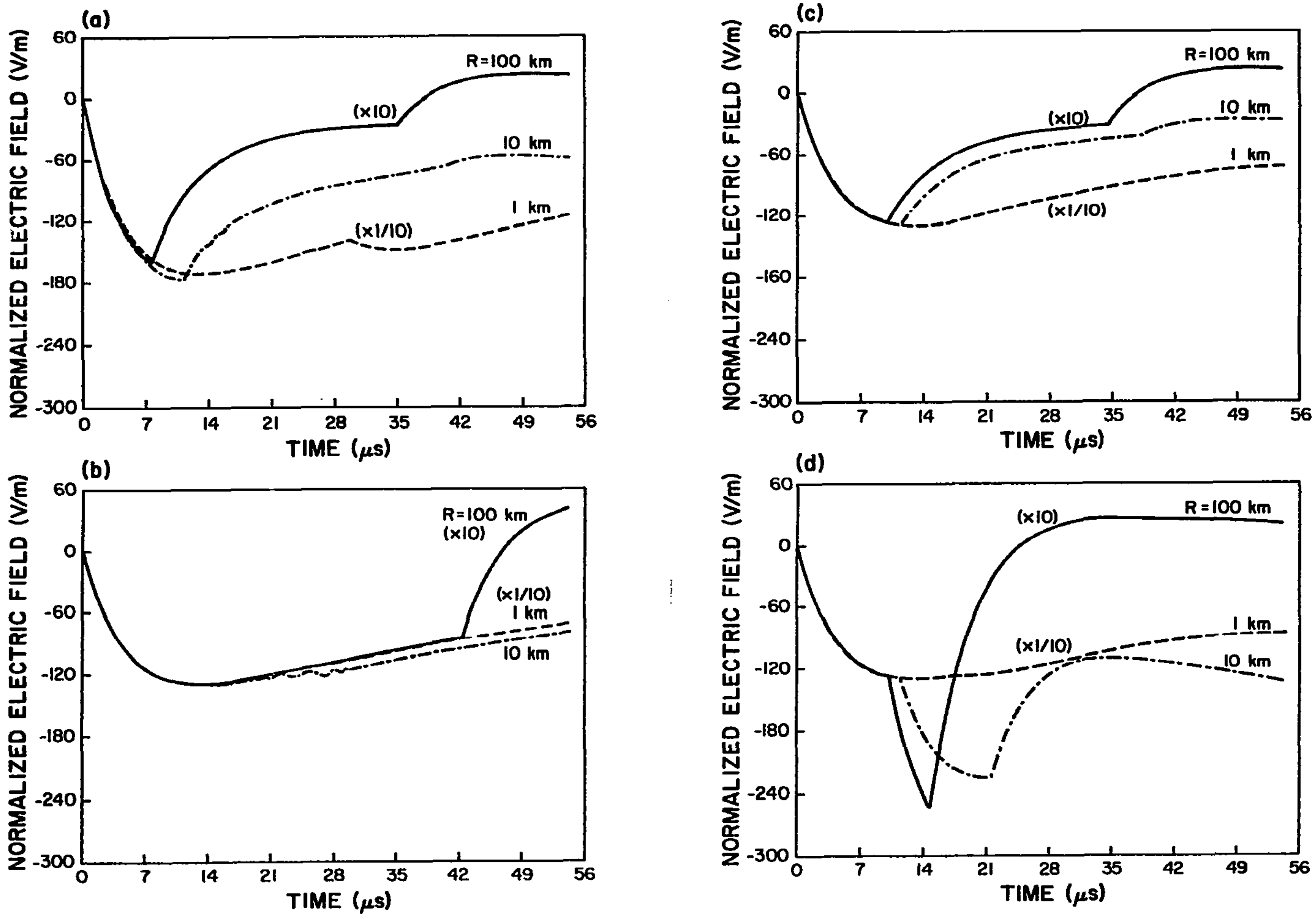

Figure 4.3.b Calculated electric fields for designed tortuous channels using compound exponential current model. a) XMYM(XMYP), b) ZD, c) ZHXP, and d) ZHXM.

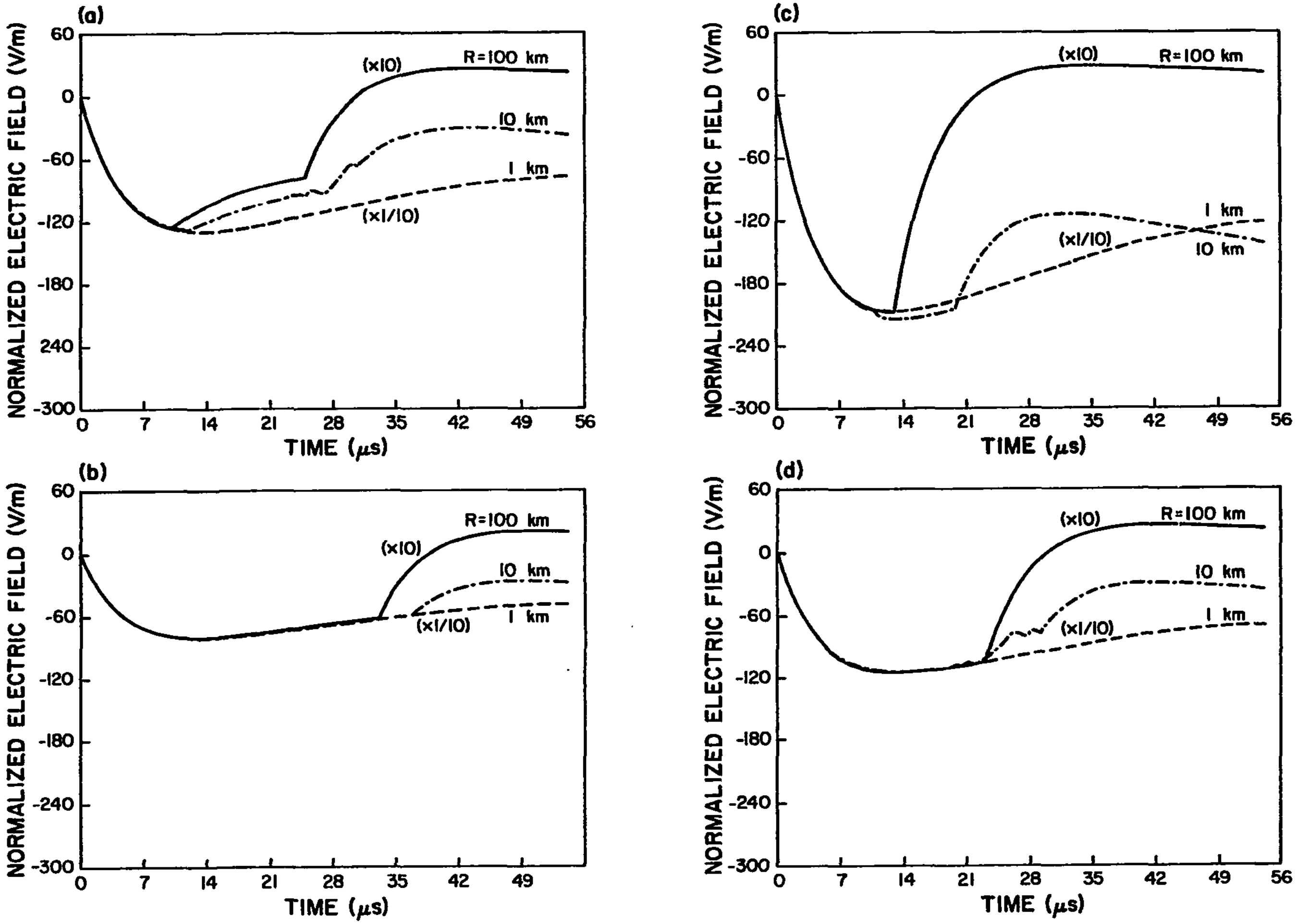

Figure 4.3.c Calculated electric fields for designed tortuous channels using compound exponential current model. a) ZHYP(ZHYM), b) XPZT, c) XMZT, and d) YPZT(YMZT).

from the turning point to the field point, R_2 is the distance from the channel top to the field point, and R_0 is the distance from the ground strike point to the field point. For this current model, the return stroke current wavefront is assumed to propagate with the speed of light. Table 4.2 shows the calculated times (t_1, t_2) and associated parameters (ℓ_1, ℓ_2, R_1, R_2) for the 17 channel geometries. Abrupt changes in the calculated waveforms corresponding to these times are indeed observed in Figure 4.3.

By comparing the waveforms from the tortuous channel and the vertical reference channel, one can see significant effects due to channel tortuosity. Both the magnitude and waveshape of the calculated electric field depend on and are indicative of channel geometry. The interpretation of rise and decay times of the waveforms become ambiguous for the tortuous channels. The magnitude of the calculated field generally increases if the channel turns toward the field point, and vice versa. At close range, channel tortuosity has a smaller effect than at greater distances. This is due to the fact that close by the field is predominately electrostatic, and at long distance, the radiation field dominates.

4.3.2 Modified Return Stroke Model of Lin et al.

For the modified current model of Lin et al., the mesh sizes used in EMFIELD calculations were $\Delta t = 0.35\ \mu s$, $\Delta \ell = 2$ m, and $\Delta z = 10$ m. Figure 4.4 shows the results of the reference case where the channel geometry is a vertical straight line of 6 km high. Results for the same tortuous channels used previously are shown in Figure 4.5. Electric

TABLE 4.2. Calculated Times, t_1 and t_2, and Associated Parameters for 17 Channel Geometries Using Compound Exponential Transmission Line Model ($v = c = 3 \times 10^8$ m/s)

Channel Type	ℓ_1 (km)	ℓ_2 (km)	$R_0 = 1$ km				$R_0 = 10$ km				$R_0 = 100$ km			
			R_1 (km)	R_2 (km)	t_1 (μs)	t_2 (μs)	R_1 (km)	R_2 (km)	t_1 (μs)	t_2 (μs)	R_1 (km)	R_2 (km)	t_1 (μs)	t_2 (μs)
XP	4.24	8.48	5.00	6.08	27.5	45.2	13.34	11.66	25.3	33.8	103.04	100.18	24.3	28.9
XM	4.24	8.48	3.60	6.08	22.8	45.2	7.62	11.66	6.2	33.8	97.05	100.18	4.3	28.9
YP(YM)	4.24	8.48	4.36	6.08	25.3	45.2	10.86	11.66	17.0	33.8	100.09	100.18	14.4	28.9
XPYP(XPYM)	5.20	10.40	5.83	6.08	33.4	51.6	13.67	11.66	29.6	40.2	103.09	100.18	27.6	35.3
XMYM(XMYP)	5.20	10.40	4.69	6.08	29.6	51.6	8.18	11.66	11.3	40.2	97.09	100.18	7.6	35.3
ZD	-	12.00	-	12.04	-	76.8	-	15.62	-	58.7	-	100.72	-	42.4
ZHXP	3.00	7.24	3.16	7.21	17.2	44.8	10.44	14.32	11.5	38.5	100.04	103.17	10.1	34.7
ZHXM	3.00	7.24	3.16	6.32	17.2	41.9	10.44	9.22	11.5	21.5	100.04	97.18	10.1	14.7
ZHYP(ZHYM)	3.00	7.24	3.16	6.78	17.2	43.4	10.44	12.04	11.5	30.9	100.04	100.22	10.1	24.9
XPZT	-	6.71	-	7.21	-	43.1	-	14.32	-	36.8	-	103.17	-	32.9
XMZT	-	6.71	-	6.32	-	40.1	-	9.22	-	19.8	-	97.18	-	13.0
YPZT(YMZT)	-	6.71	-	6.78	-	41.6	-	12.04	-	29.2	-	100.22	-	23.1

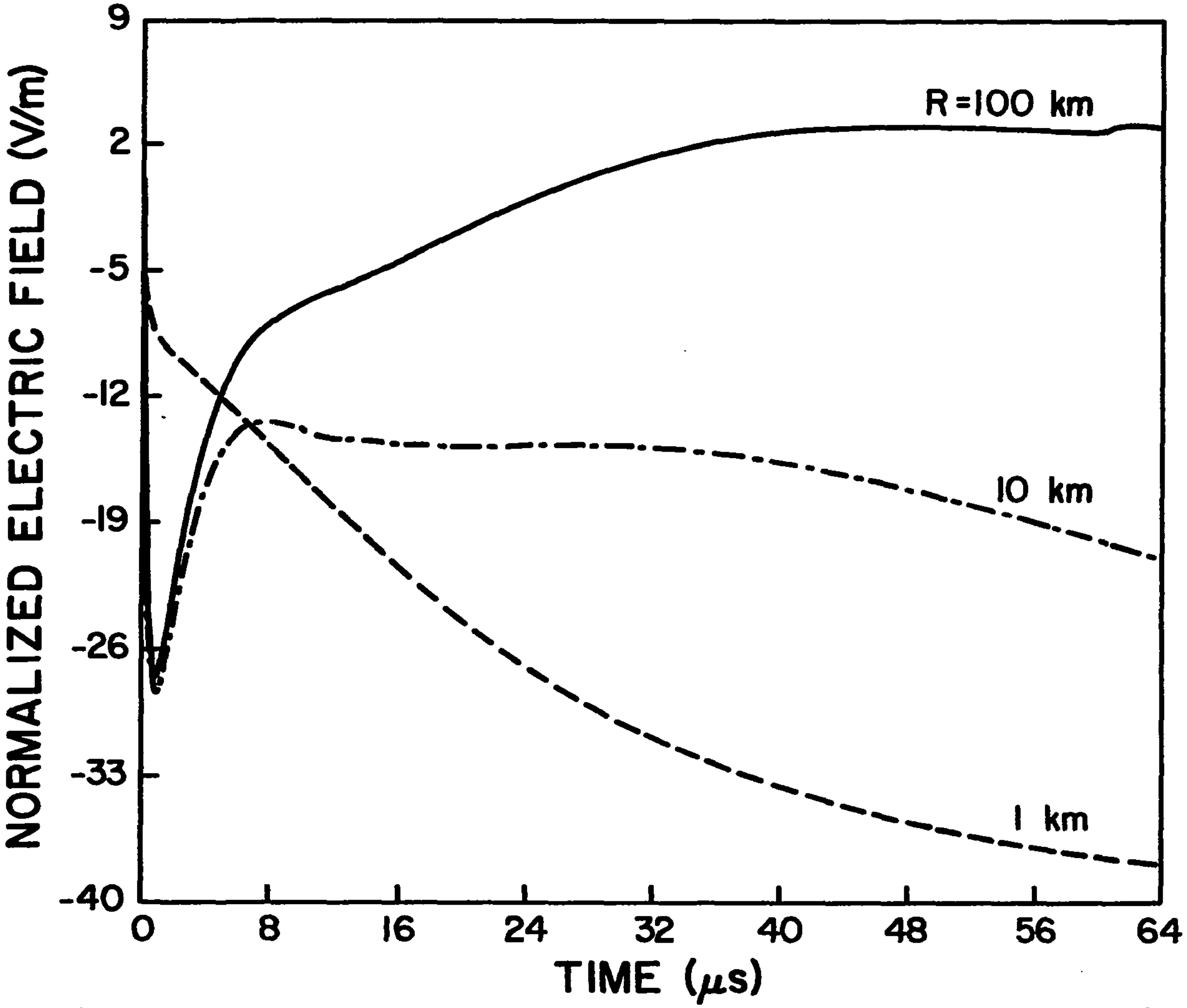

Figure 4.4 Reference case for the modified current model of Lin et al.: calculated electric fields for a vertical channel of 6 km high. A vertical scaling factor of 1/40 and 10 is used to show the electric fields at R = 1 km and R = 100 km, respectively.

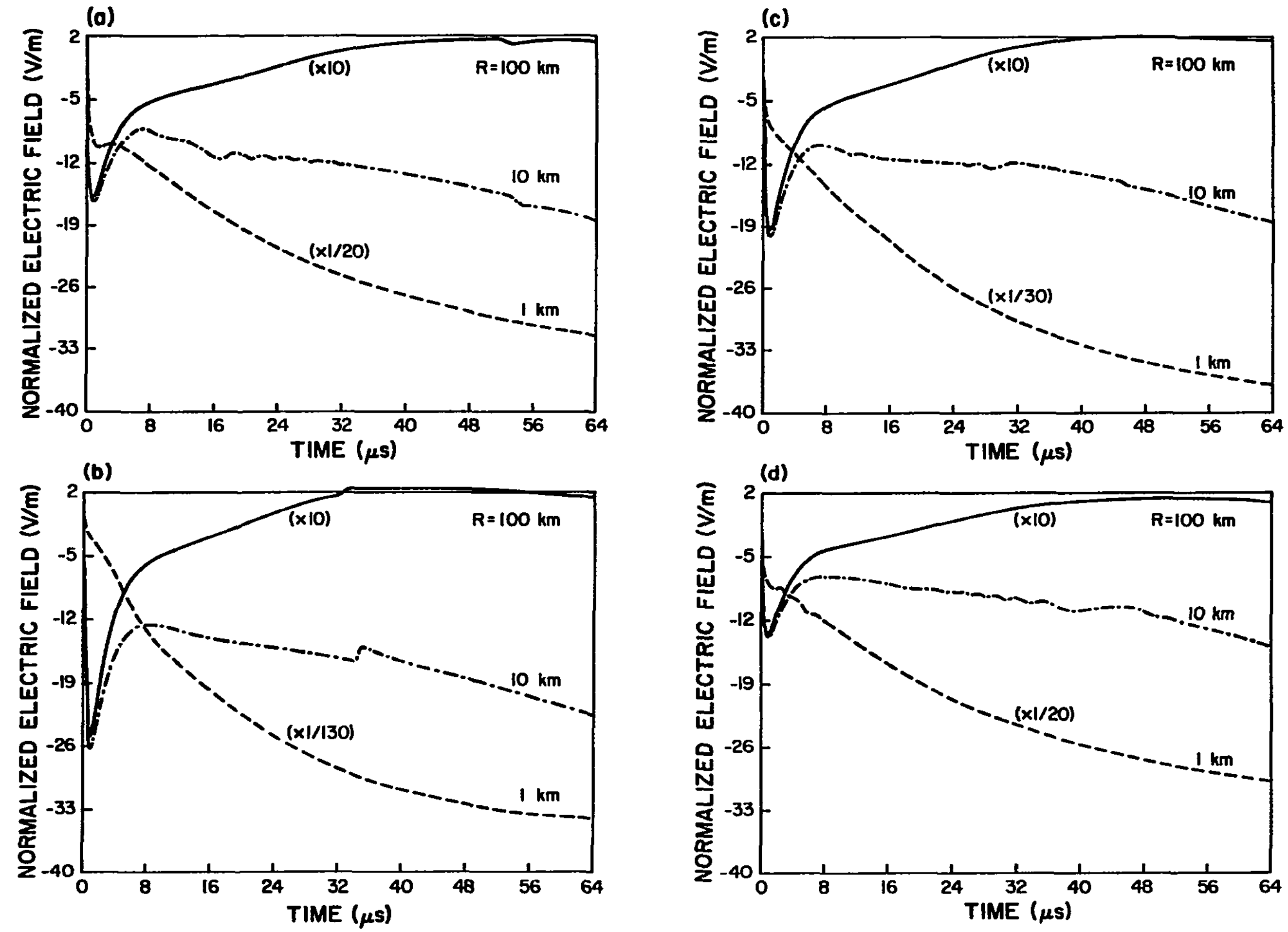

Figure 4.5.a Calculated electric fields for designed tortuous channels using the modified current model of Lin et al. Note that electric fields are shown with different scaling factors for R = 1 km and R = 100 km. (a) XP (b) XM (c) YP(YM) (d) XPYP(XPYM).

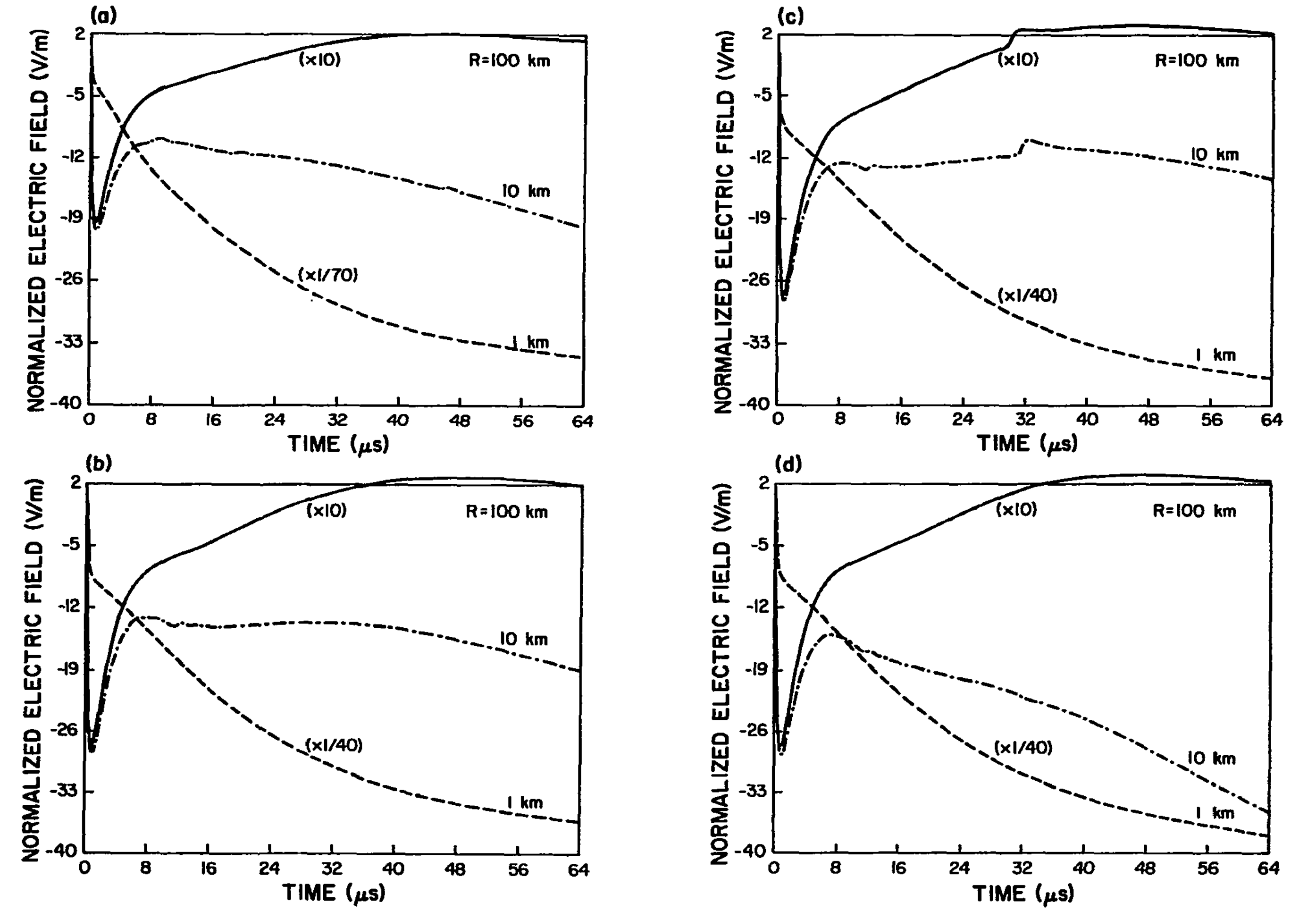

Figure 4.5.b Calculated electric fields for designed tortuous channels using the modified current model of Lin et al. Note that electric fields are shown with different scaling factors for R = 1 km and R = 100 km. (a) XMYM(XMYP) (b) ZD (c) ZHXP (d) ZHXM.

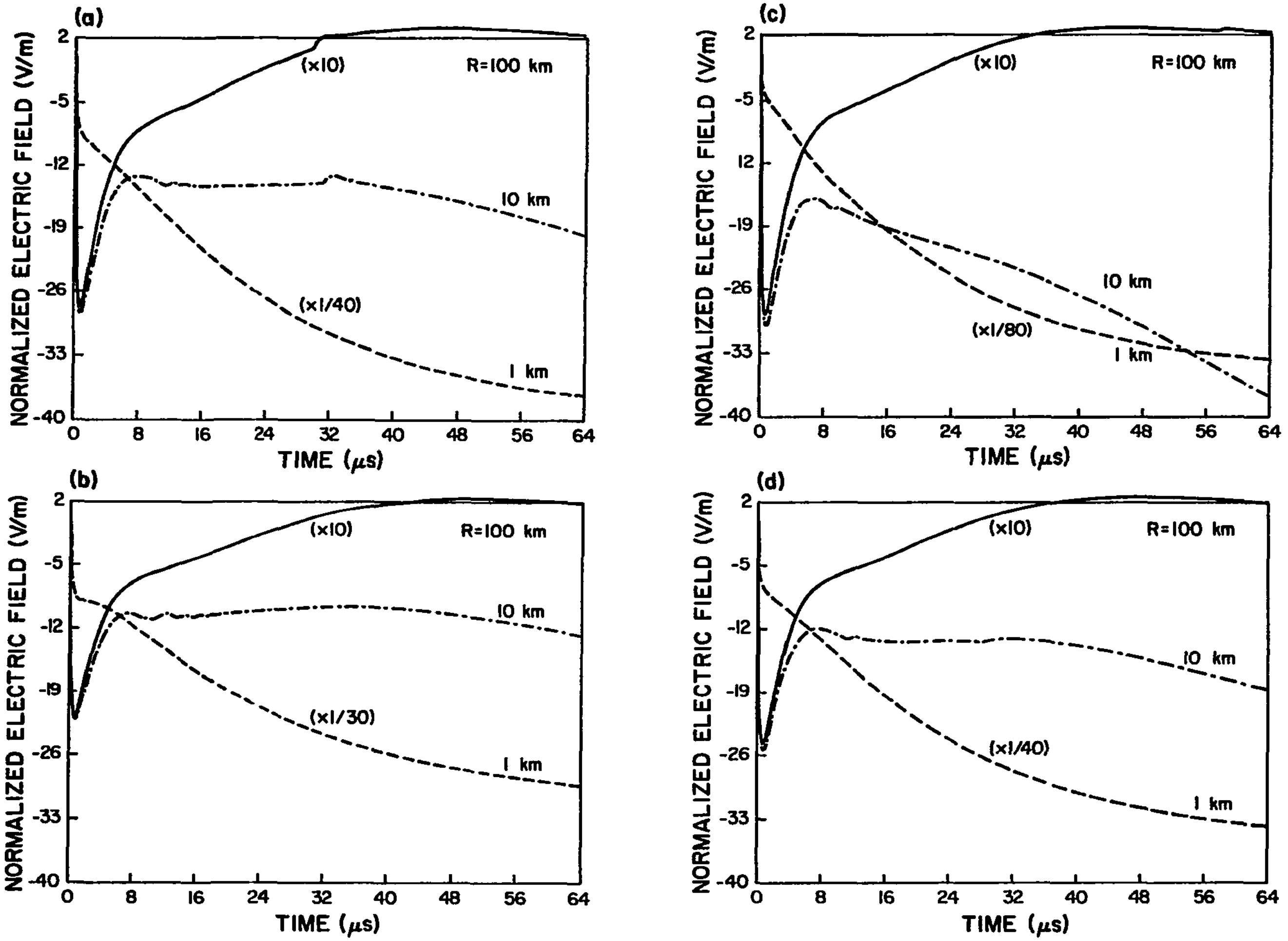

Figure 4.5.c Calculated electric fields for designed tortuous channels using the modified current model of Lin et al. Note that electric fields are shown with different scaling factors for R = 1 km and R = 100 km. (a) ZHYP(ZHYM) (b) XPZT (c) XMZT (d) YPZT(YMZT).

field changes at 1 km and 100 km are shown with different scaling factors as shown in each figure. In this model, the breakdown wavefront is assumed to propagate at one third the speed of light. The times t_1 and t_2 in the calculated waveforms corresponding to the channel tortuosity can be calculated again by Equations 4.1 and 4.2. The results are shown in Table 4.3.

By comparing the waveforms of the 17 tortuous channels and the vertical reference case, one sees that with the modified model of Lin et al., channel tortuosity has a smaller effect. Only minor perturbations in ΔE are observed at the major turning points. This is a significant contrast to the effects of tortuosity when the compound exponential transmission line model is used (Section 4.3.1). Nevertheless, the magnitude of the calculated electric field does depend on the channel geometry and the range to the field point. Since both the breakdown and corona currents decay with height, it is not surprising that the effects of channel tortuosity are less than that in the compound exponential model. The radiation field for all channel geometries at far distances resembles the current waveshape. This is not the case in the previous model where the radiation waveform is significantly different from the current waveform due to channel tortuosity.

4.4 Study Using Complex Channel Geometry

The calculations incorporating simple channel tortuosity reported in previous sections are relatively easy to analyze and have elucidated several fundamental aspects of the effects of channel tortuosity on calculated electric field waveforms. Nevertheless, such

TABLE 4.3. Calculated Times, t_1 and t_2, and Associated Parameters for 12 Channel Geometries Using the Modified Model of Lin et al. ($v = 1 \times 10^8$ m/s)

Channel Type	ℓ_1 (km)	ℓ_2 (km)	R_0 = 1 km				R_0 = 10 km				R_0 = 100 km			
			R_1 (km)	R_2 (km)	t_1 (μs)	t_2 (μs)	R_1 (km)	R_2 (km)	t_1 (μs)	t_2 (μs)	R_1 (km)	R_2 (km)	t_1 (μs)	t_2 (μs)
XP	4.24	8.48	5.00	6.08	55.7	101.7	13.34	11.66	53.5	90.3	103.04	100.18	52.5	85.4
XM	4.24	8.48	3.60	6.08	51.1	101.7	7.62	11.66	34.5	90.3	97.05	100.18	32.6	85.4
YP(YM)	4.24	8.48	4.36	6.08	53.6	101.7	10.86	11.66	45.3	90.3	100.09	100.18	42.7	85.4
XPYP(XPYM)	5.20	10.40	5.83	6.08	68.1	120.9	13.67	11.66	64.2	109.5	103.09	100.18	62.3	104.6
XMYM(XMYP)	5.20	10.40	4.69	6.08	64.3	102.9	8.18	11.66	45.9	109.5	97.09	100.18	42.3	104.6
ZD	-	12.00	-	12.04	-	156.8	-	15.62	-	138.7	-	100.72	-	122.4
ZHXP	3.00	7.24	3.16	7.21	37.2	93.1	10.44	14.32	31.5	86.8	100.04	103.17	30.1	83.0
ZHXM	3.00	7.24	3.16	6.32	37.2	90.1	10.44	9.22	31.5	69.8	100.04	97.18	30.1	63.0
ZHYP(ZHYM)	3.00	7.24	3.16	6.78	37.2	91.7	10.44	12.04	31.5	79.2	100.04	100.22	30.1	73.1
XPZT	-	6.71	-	7.21	-	87.8	-	14.32	-	81.5	-	103.17	-	77.7
XMZT	-	6.71	-	6.32	-	84.8	-	9.22	-	64.5	-	97.18	-	57.7
YPZT(YMZT)	-	6.71	-	6.78	-	86.4	-	12.04	-	73.9	-	100.22	-	67.8

simplified channel geometries are neither representative nor realistic of most naturally occurring lightning. They are either over simplified or greatly exaggerated as compared to lightning photographs. It is possible that some of the findings using simplified geometries are not valid in general. Therefore, it is prudent to extend this study to include complex channel geometry, which is more representative of real lightning.

The tortuous channel shown in Figure 3.9 was chosen. It was constructed by connecting randomly oriented segments to form a piecewise linear chain. The individual element lengths and orientation were chosen by a Monte Carlo simulation (LeVine and Meneghini, 1978). The calculated electric field waveforms from the compound exponential transmission line model at ranges of 1, 10, and 100 km were shown earlier in Figure 3.8 to confirm the validity of the EMFIELD code. These solutions are repeated in Figure 4.6.a to facilitate comparison with the solutions obtained from the modified current mode of Lin et al. for the same channel geometry, which is shown in Figure 4.6.b.

By comparing the results from linear and tortuous channels using the compound exponential current model (Figures 4.2 and 4.6.a), one sees that channel tortuosity introduces many large fluctuations in the calculated ΔE waveforms, especially at distant ranges. Every sharp turn in the waveform can be correlated to a major turning point in the lightning channel. Furthermore, these calculated ΔE waveforms indicate that the channel tortuosity increases the higher frequency radiations as expected.

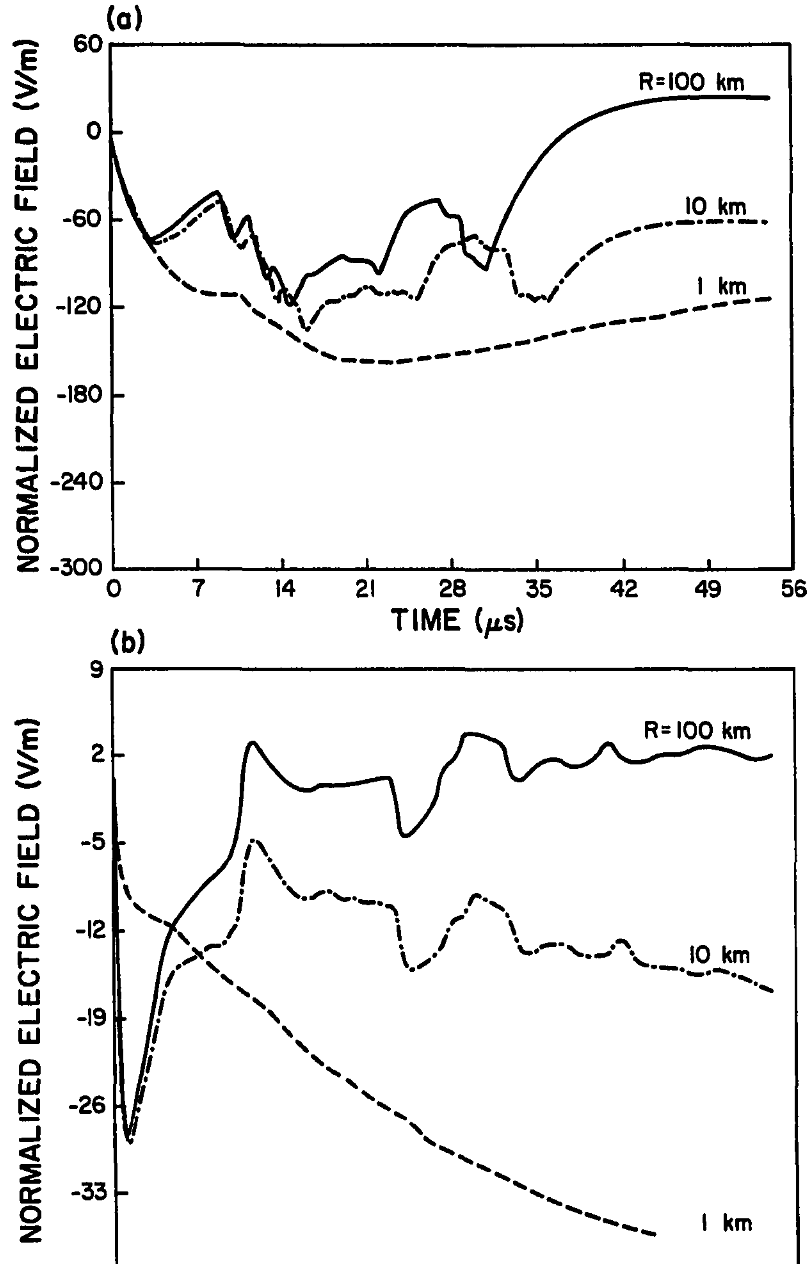

Figure 4.6 Calculated electric fields for simulated tortuous channel using a) compound exponential current model (vertical scaling factors are 1/10 and 10 for R = 1 km and R = 100 km, respectively), b) modified current model of Lin et al. (vertical scaling factors are 1/40 and 10 for R = 1 km and R = 100 km, respectively).

By comparing the results from linear and tortuous channels using the modified current model of Lin et al. (Figures 4.4 and 4.6.b), one sees that a tortuous channel introduces only small perturbations in the ΔE waveform obtained with a linear channel. Due to the height-dependent nature of this current model, tortuosity in the lower portion of the channel tends to introduce larger fluctuations in the calculated electric field than does tortuosity at greater heights. At close range, channel tortuosity has a smaller effect on the calculated waveform since only the static field is dominant. The high frequency fluctuations caused by channel tortuosity are relatively small and may not be measurable.

4.5 Conclusions

Based on the study performed in this chapter, the following conclusions are obtained:

1. The effects of channel tortuosity on the calculated electric field during a return stroke depend on the current model being used. Significant effects are observed in the compound exponential transmission line model, while only small effects are found in the modified model of Lin et al.

2. The times t_1 and t_2 associated with turning points in the ΔE waveforms are directly correlated to channel geometry and can be calculated precisely in both models. In the compound exponential transmission line model, these times are very prominent and easily identifiable; while in the modified model of Lin et al., they are less clear. However, if the turning points occur in the lower part of the channel,

the effect of tortuosity on the modified model of Lin et al. would be enhanced because of the height dependence of this model. If the major turning points caused by channel geometry are truly observable, simultaneously measured electric fields at several sites are potentially useful to reconstruct channel geometry. It may also be possible to estimate the return stroke wavefront speed.

3. The waveform of the calculated electric field depends strongly on the range to the field point in both models. Its dependency on channel tortuosity is greater in the first model than in the second.

4. The interpretation of rise time of the ΔE waveforms becomes ambiguous for tortuous channels when using compound exponential transmission line model. However, the rise time of the initial peak in ΔE calculated with the modified model of Lin et al. is not sensitive to channel tortuosity or the range to the field point.

CHAPTER V

COMPARISON OF CALCULATED VERSUS MEASURED ELECTRIC FIELD CHANGES USING RECONSTRUCTED CHANNEL GEOMETRIES

5.1 Introduction

The analyses described in Chapter IV have elucidated several basic features of the impacts of channel tortuosity on calculated electric fields for return strokes. They provide a foundation for further investigation and understanding of this issue in a more realistic way. Since the channel geometries being analyzed in Chapter IV were artificially designed, the calculated ΔE waveforms cannot be verified by experimental results. In order to evaluate the effects of tortuosity on radiated fields from natural lightning, simultaneously recorded electric fields and channel geometries are needed. As stated in Chapter I, the major thrust of this dissertation research is to compare the calculated and measured electric field changes using reconstructed channel geometries. It is a very challenging task in that one has to obtain good quality data on both electric field changes and channel geometry of a lightning flash, which is usually highly unpredictable in time and space as discussed in Chapter II.

Channel reconstruction using the ray tracing technique from acoustic data was originally planned and conducted in this research.

The results, as described in Chapter II, indicate only the gross features of the channel geometry. Fine details of the channel tortuosity and the time sequence of events cannot be obtained from this technique. Furthermore, the portion of the channel below about 1 km cannot be reconstructed accurately because of the reflection of thunder signals by the terrain. In view of these deficiencies and realizing the importance of the lower portion of the channel in the model of Lin et al., it was subsequently decided that photographic channel data should also be considered. These two types of data will complement each other since photographic data cover the channel below the cloud base while the acoustic data adequately describe the higher, in-cloud channels. Unfortunately, there are no dual-station, photographic data available in conjunction with thunder data obtained at NSSL. Multistation television (TV) video data recorded at the University of Florida Lightning Research Laboratory were provided by Dr. Martin Uman and Dr. William Beasley along with the associated ΔE waveforms. This set of data not only meets the need of this research but also broadens the scope of it. In the following sections, detailed analysis of channel tortuosity for selected flashes from these two sets of data and the significance of the tortuosity will be presented.

5.2 Analysis of University of Florida Data

5.2.1 Channel Reconstruction from Two-Station TV Data

Two-station TV pictures of two lightning flashes recorded at Gainesville, Florida during the summer of 1979 were selected. The first flash, labelled GNV1, occurred on July 15 and the second flash, GNV2, occurred on July 18. The video system consisted of four TV cameras at different locations. The camera locations and viewing angles are shown in Figure 5.1. The two flashes analyzed here were within the viewing angle of both cameras 1 and 2, and therefore it is possible to reconstruct their channel geometries. The procedure for reconstruction is as follows:

1. Find the azimuth angle Θ of the ground strike point on the picture from each station by dividing the viewing angle uniformly across the screen.

2. Find the position of the ground strike point by intersecting two lines drawn from each TV camera using the corresponding azimuth angle.

3. Determine the distance R from the ground strike point to each camera.

4. Find the elevation angle ϕ for every major turning point of the channel in one picture by dividing uniformly the vertical viewing angle.

5. Calculate the height z of these turning points using

$$z = R \tan \phi \tag{5.1}$$

6. Find the corresponding points on the other picture. Generally these points in one picture are also major turning points in the other picture. The above two steps can be iterated until a completely consistent set of turning points is obtained.

7. Find the positions of these major turning points using the same steps (1 and 2) as that for the ground point.

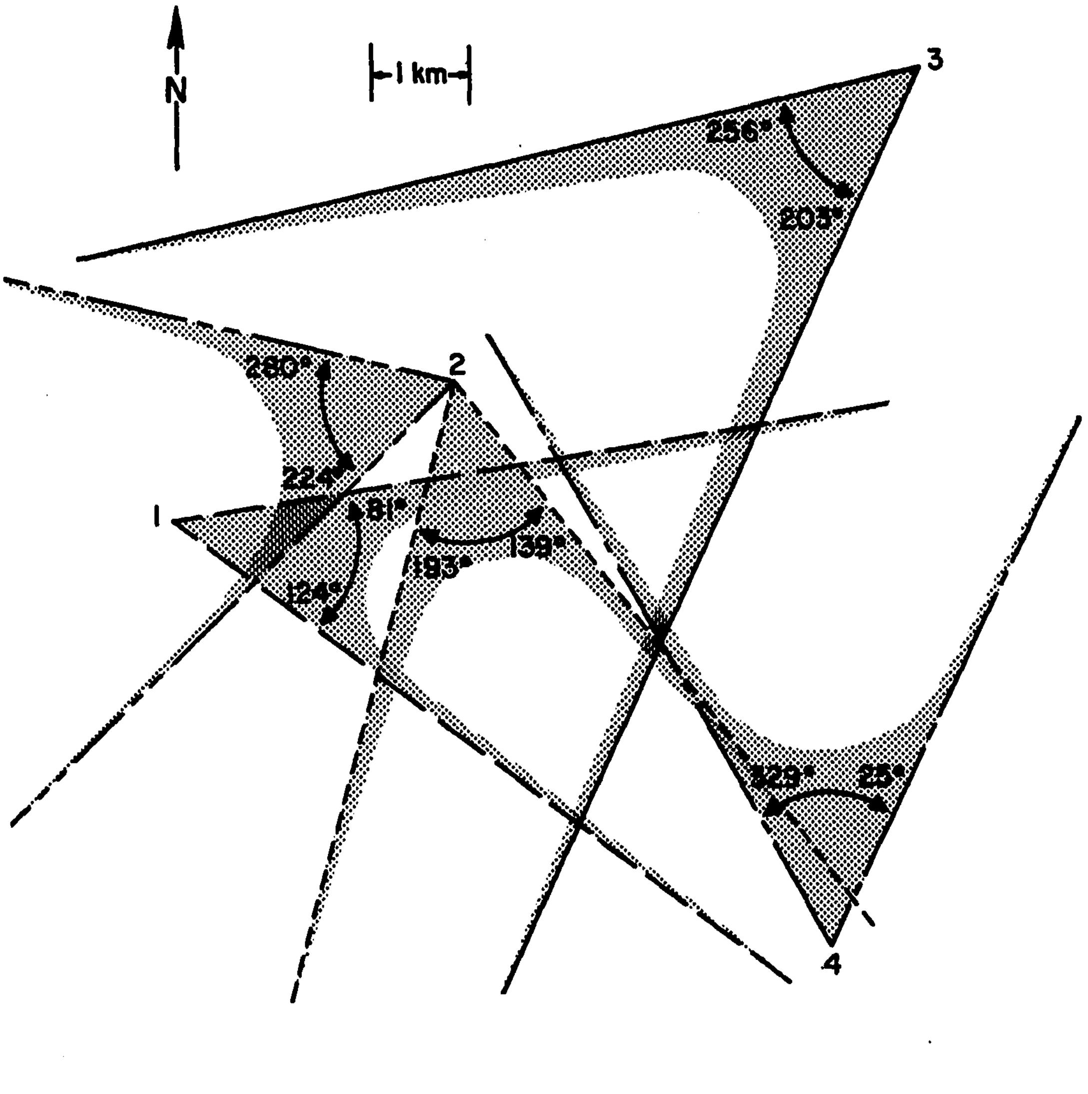

Figure 5.1 Relative locations and viewing angles of the multistation TV camera network used by the University of Florida Lightning Research Laboratory.

Figure 5.2 shows the TV pictures of the first flash, GNV1, reproduced from the original data; the corresponding major turning points from each camera are identified. Figure 5.3 shows similar features for the second flash, GNV2. The coordinates of the channel geometries obtained from the TV data are listed in Table 5.1 for GNV1 and Table 5.2 for GNV2. The origin of the coordinates is set at camera 1 where the electric field sensor was located.

There are two major sources of errors in the coordinates obtained from two-station TV data. First, since each camera only projects the channel onto the focal plane, the relative viewing angle between the two cameras with respect to the channel should be 90° in order to obtain accurately the three-dimensional coordinates. Otherwise, one needs three independent, simultaneous views. The relative viewing angles of the ground strike points from these two cameras are about 40° for both flashes; therefore some of the actual channel tortuosity may not be fully revealed and thus cannot be determined. Due to the random orientation of lightning channels, it is impossible to quantify the uncertainty arising from the relative viewing angle. Secondly, there are small errors in the measurement of angles due to the resolution of TV pictures and in the distance measurements on the map. The estimated error in the measurement of angles is within ±1°, and causes a 2% uncertainty in the range R. The final calculated coordinates will then have an error within 2.8%.

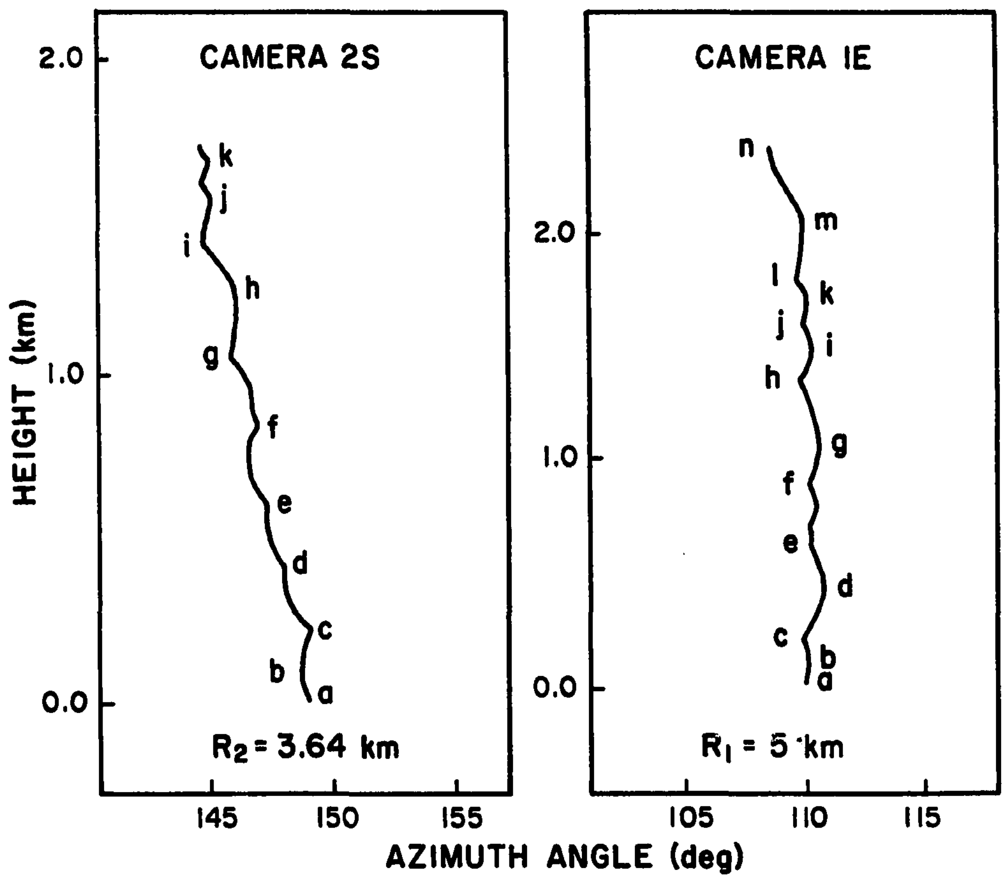

Figure 5.2 Reproduction of TV images of flash GNV1, 15 July 79, 1902:14 EST. Corresponding turning points identified from each camera are labelled with the same letter.

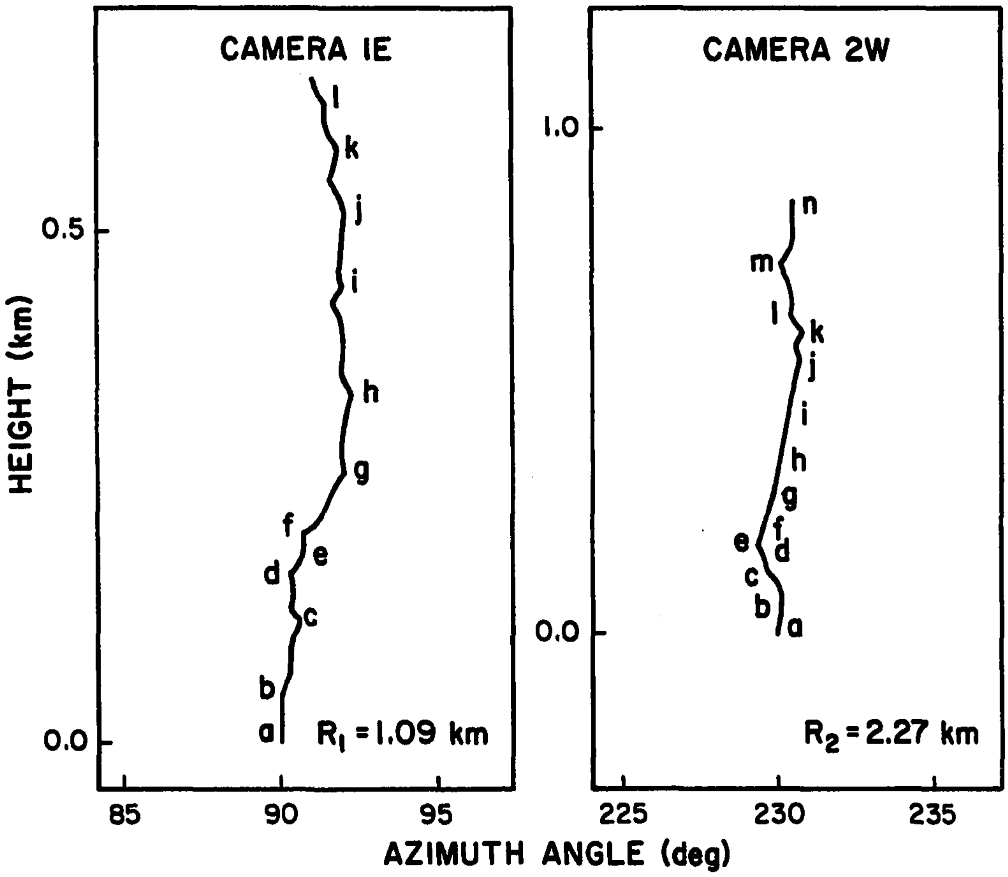

Figure 5.3 Reproduction of TV images of flash GNV2, 18 July 79, 1846:00 EST. Corresponding turning points identified from each camera are labelled with the same letter.

TABLE 5.1. Measured Azimuth Angles, Distances from Electric Field Sensor, and the Reconstructed Channel Coordinates of Flash GNV1 Obtained from Two-Station TV Pictures

Point	Azimuth Angle from Picture of Camera 1 θ_1 (°)	Azimuth Angle from Picture of Camera 2 θ_2 (°)	Distance from Electric Field Sensor R (km)	x (km)	y (km)	z (km)
a	110.0	149.0	5.00	4.70	-1.71	0.0
b	110.0	148.6	5.04	4.75	-1.72	0.09
c	110.0	149.2	5.00	4.70	-1.71	0.21
d	110.6	148.2	5.18	4.85	-1.82	0.39
e	110.0	147.5	5.18	4.87	-1.77	0.59
f	110.0	147.0	5.27	4.95	-1.80	0.82
g	110.3	146.0	5.36	5.03	-1.86	1.05
h	109.5	146.3	5.27	4.97	-1.76	1.28
i	110.0	144.7	5.55	5.22	-1.90	1.45
j	109.8	145.3	5.44	5.12	-1.84	1.55
k	110.0	145.2	5.44	5.11	-1.86	1.71
l	109.4	144.7*	5.55	5.23	-1.84	1.80
m	109.7	144.7*	5.45	5.13	-1.83	2.08
n	108.5	144.7*	5.55	5.26	-1.76	2.38

*The last three points (l, m, n) are out of the picture frame of camera 2; the numbers here are estimated.

Note: The xyz coordinate origin is at camera 1 (same location as Electric Field Sensor); +x direction is east; +y direction is north.

TABLE 5.2. Measured Azimuth Angles, Distances from Electric Field Sensor, and the Reconstructed Channel Coordinates of Flash GNV2 Obtained from Two-Station TV Pictures

Point	Azimuth Angle from Picture of Camera 1 θ_1 (°)	Azimuth Angle from Picture of Camera 2 θ_2 (°)	Distance from Electric Field Sensor R (km)	x (km)	y (km)	z (km)
a	90.0	230.0	1.09	1.09	0.00	0.00
b	90.0	230.0	1.09	1.09	0.00	0.05
c	90.5	229.6	1.13	1.13	-0.01	0.11
d	90.3	229.6	1.11	1.11	-0.01	0.15
e	90.7	229.2	1.09	1.09	-0.01	0.16
f	90.8	229.4	1.10	1.10	-0.01	0.18
g	91.8	229.8	0.91	0.91	-0.03	0.25
h	92.1	230.0	0.91	0.91	-0.03	0.32
i	91.8	230.7	0.86	0.86	-0.03	0.43
j	91.8	230.8	0.82	0.82	-0.03	0.51
k	91.5	230.8	0.84	0.84	-0.02	0.55
l	91.4	230.6	0.84	0.84	-0.02	0.64
m	91.4*	230.0	1.01	1.01	-0.03	0.73
n	91.4*	230.4	0.95	0.95	-0.02	0.86

*The last two points (m, n) are out of the picture frame of camera 1; the numbers here are estimated.

Note: The xyz coordinate origin is at camera 1 (same location as Electric Field Sensor); +x direction is east; +y direction is north.

5.2.2 Comparison of Measured and Calculated Electric Fields

5.2.2.a Flash GNV1. The recorded electric field waveform of GNV1 is reproduced in Figure 5.4. The general waveform consists of a very sharp initial peak of 73.6 V/m at 3 μs, a transition region about 10 μs wide, and a linear ramp with a slope of -0.8 V/m per μs. This waveform exhibits many features typical of a return stroke at a distance of about 5 km (Tiller et al., 1976). High frequency (~1 MHz) oscillations with amplitude of about 10-15 V/m p-p are observed in the data. The source of the periodic noise is unknown, but it is unlikely that it was generated by the lightning.

Electric field waveforms were calculated with EMFIELD using the modified current model of Lin et al. Two calculations were made: one with reconstructed channel geometry and the other with a vertical linear channel. To fit the experimental data, the current model contains these parameters in the first calculation: I_0 = 31 kA for breakdown current and I_u = 5.1 kA for the uniform current, and the rest of the current model parameters remain the same as for the second benchmark problem in Section 3.3.3. Channel geometry above the top of the TV pictures of GNV1 is assumed to be vertical up to a height of about 7 km. The total channel length of GNV1 is then about 7.5 km.

The calculated ΔE using the reconstructed channel fits satisfactorily with the experimental data as can be seen in Figure 5.4. The calculated ΔE has several prominent turning points that occur at the times associated with the major turns in the TV pictures. After the first 10 μs, the turning points in the recorded waveform cannot be

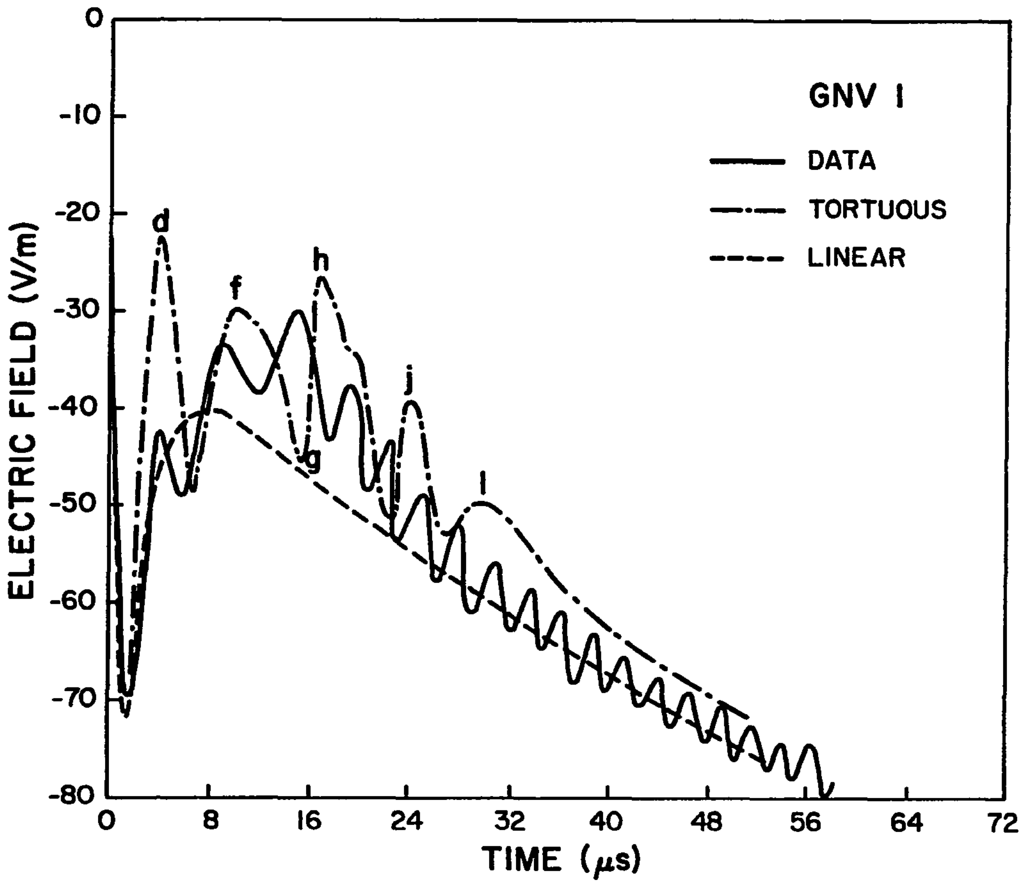

Figure 5.4 Calculated and measured electric field changes for flash GNV1. The results labelled tortuous and linear refer to ΔE calculated with the reconstructed tortuous and the equivalent vertical channel, respectively.

confidently identified with channel tortuosity due to the noise oscillation.

In the second calculation, the channel geometry is assumed to be vertical with a height of 7.5 km, which is equivalent to the total channel length in the first calculation. This linear channel is also assumed to be located at the same ground strike point (R = 5 km) as the tortuous one. In order to fit the experimental data, the current model contains the same assumed parameters as in the previous calculation except that I_u had to be changed to 3.1 kA. The results for this case are also shown in Figure 5.4 for comparison. A reasonably good fit to the general trend of the measured data for the initial peak and the linear ramp portion are obtained. However, the transition region in the calculated results is narrower than in the experimental data. One can, of course, modify the parameters for the corona current to improve the agreement for this portion.

5.2.2.b Flash GNV2. The measured electric field change for flash GNV2 is reproduced in Figure 5.5. There is a very sharp initial rapid decrease to -434 V/m at 3 μs, followed immediately by an almost linearly varying transition region that is 24 μs wide and has a slope of about -40 V/m per μs; then there is linear ramp with a slope of -20 V/m per μs. This waveform exhibits many features of a typical return stroke at a distance of approximately 1 km. Again high frequency (~1 MHz) oscillations similar to those in GNV1 are observed in the original data. The amplitude of the oscillation is about 100-250 V/m p-p. Although the relative amplitude of noise in this case is smaller than the previous

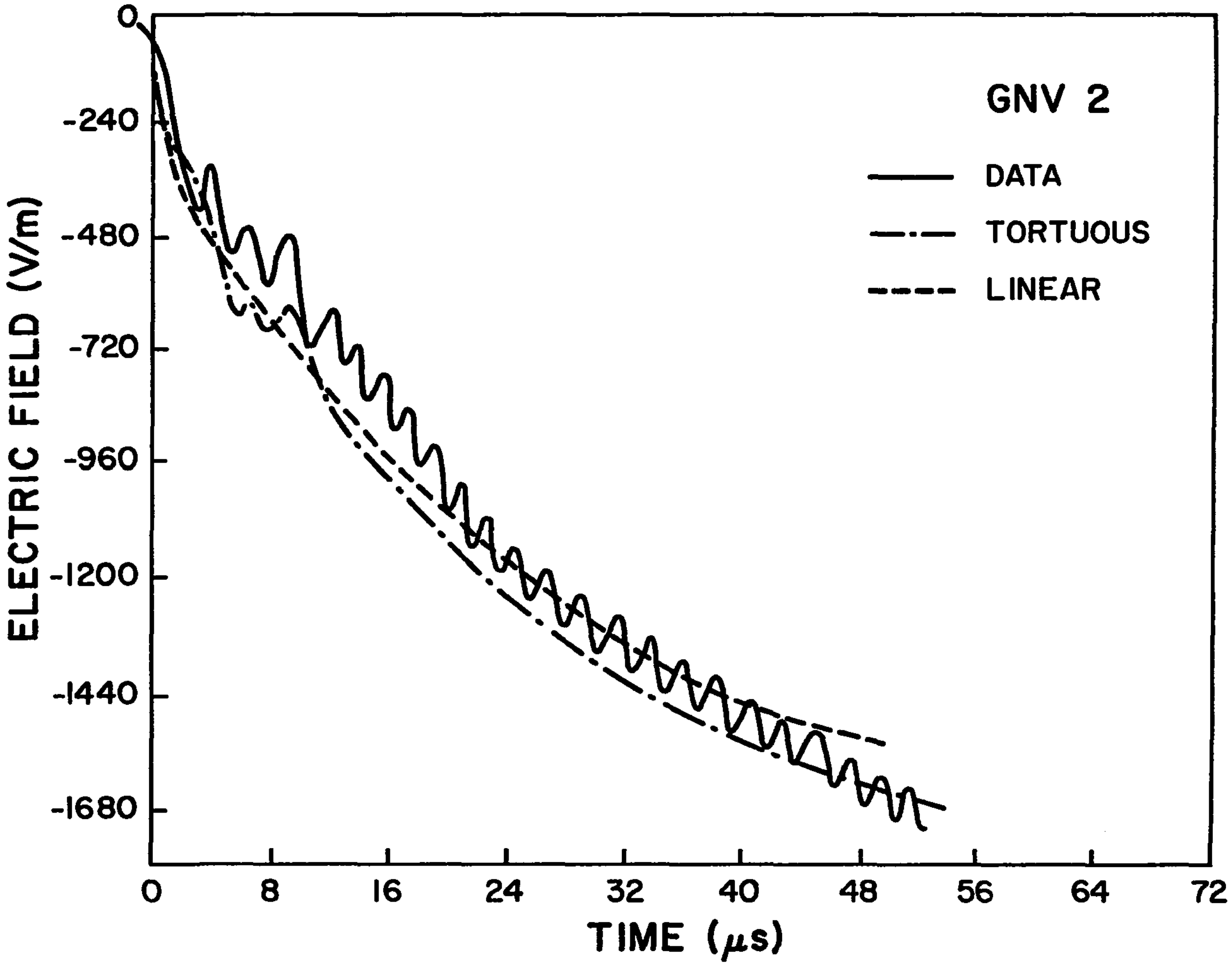

Figure 5.5 Calculated and measured electric field changes for flash GNV2. The results labelled tortuous and linear refer to ΔE calculated with the reconstructed tortuous and the equivalent vertical channel, respectively.

one, it is still difficult to associate the oscillations with the channel tortuosity.

Results of calculated electric field changes using the reconstructed channel as well as the vertical channel are also shown in Figure 5.5. In the tortuous case, the current model has the same parameters as the second benchmark problem in Section 3.3.3. Again the channel geometry above the TV picture is assumed to be vertical up to a height of 7.2 km. This makes the total channel length of GNV2 7.5 km. The calculated waveform using the reconstructed channel agrees very well with the experimental data as can be seen in the figure. Two minor fluctuations due to channel tortuosity are observed in the calculated waveform as well as in the experimental data. Since the range of this flash was about 1 km from the field sensor, the effect of channel geometry on the calculated waveform should be small as indicated by the analyses in Chapter IV.

The calculated electric field change for GNV2 using a vertical linear channel is also shown in Figure 5.5. The current model parameters are the same as for the previous one. In order to obtain agreement with experimental data, the length of the linear channel is assumed to be 7.5 km. The channel should be closer to the electric sensor since the actual flash was slanted slightly toward it. Use of an equivalent range of 0.95 km gives a good fit of the calculated to the experimental waveforms.

From the analysis of flashes GNV1 and GNV2, the following can be concluded: (1) Results of calculations for tortuous and linear channels using the same current model do not always agree with each other. If different parameters in the current model are assumed, both calculations can reproduce the measured ΔE reasonably well. (2) Channel tortuosity produces fluctuations that can barely be seen in the experimental data. The noise levels in the measured waveforms are comparable to the calculated signal fluctuations due to small channel tortuosity. The degrees of tortuosity of channel geometries for GNV1 and GNV2 are relatively small; therefore only minor differences were found in the calculations with tortuous and vertical channels. One can certainly expect such a disparity to widen as the magnitude of the channel tortuosity increases.

5.3 Analysis of NSSL Data

5.3.1 Antenna Circuit Response to an Electric Field Change

The output voltage $V_o(t)$ obtained from the fast antenna can be related to the electric field change at the sensing plate during return strokes. The relationship between the field strength $E(t)$ and measured voltage $V_o(t)$ depends on the characteristics of the electronic circuit, especially its decay time constant $R_f C_f$. A schematic diagram depicting the fast (and slow) antenna electronics is shown in Figure 2.5.

A change in the electric field of ΔE at the sensing plate will change the induced charge on the plate by an amount

$$\Delta Q = - \varepsilon K A \Delta E \qquad (5.2)$$

where ε is the atmospheric permittivity and K is the form factor and other electronic gains in the system. The value of K has been determined by instrument calibration using known input signals and simultaneous recordings of field changes from distant lightning detected with flush-mount and elevated antennas (the antennas were normally mounted above the ground to achieve higher sensitivity).

The input current i_{in} can be written as

$$i_{in} = \frac{dQ}{dt} = -\ \varepsilon K\ A\ \frac{dE}{dt} \tag{5.3}$$

Kirchhoff's point rule at the summing point S gives

$$i_{in} + i_R + i_c = 0 \tag{5.4}$$

For an ideal operational amplifier in the inverting mode,

$$i_R = \frac{V_o}{R_f},\ i_c = C_f\ \frac{dV_o}{dt} \tag{5.5}$$

By substituting Equations 5.3 and 5.4 into Equation 5.5, one gets

$$\frac{dV_o}{dt} + \frac{1}{R_f C_f}\ V_o = \frac{\varepsilon_o\ A\ K}{C_f}\ \frac{dE}{dt} \tag{5.6}$$

This is a first order, inhomogeneous differential equation, and it can be solved by the method of integrating factor. The solution is

$$\begin{aligned} V_o(t) = V_o(0)\ e^{-\frac{t}{R_f C_f}} &- \frac{\varepsilon_o\ A\ K}{C_f}\ E(0)\ e^{-\frac{t}{R_f C_f}} + \frac{\varepsilon_o\ A\ K}{C_f}\ E(t) \\ &- \frac{\varepsilon_o\ A\ K}{R_f C_f^{\,2}}\ e^{-\frac{t}{R_f C_f}} \int_0^t E(t')\ e^{\frac{t'}{R_f C_f}}\ dt' \end{aligned} \tag{5.7}$$

If the output voltage $V_o(t)$ is measured with respect to its initial value $V_o(0)$, the output signal becomes

$$\Delta V_o(t) = V_o(t) - V_o(0) = V_o(0)\ [e^{-t/R_fC_f} - 1] +$$

$$\frac{\varepsilon_o\ A\ K}{C_f} \left[E(t) - E(0)\ e^{-\frac{t}{R_fC_f}} - \frac{1}{R_fC_f}\ e^{-\frac{t}{R_fC_f}} \right.$$

$$\left. \cdot \int_o^t E(t')\ e^{\frac{t'}{R_fC_f}}\ dt' \right] \qquad (5.8)$$

When the time constant R_fC_f is very large relative to the duration of the field change of interest, the first term vanishes and the last term in Equation 5.8 is small and therefore can be neglected. The output signal becomes

$$\Delta V_o(t) = \frac{\varepsilon_o\ A\ K}{C_f}\ \Delta E(t),\ \text{with}\ \Delta E(t) = E(t) - E(0) \qquad (5.9)$$

This result is exactly the formula used by Krehbiel, et al. (1979) for the analysis of multistation slow antenna data.

In the above derivations, it is assumed that the rise time of the circuit is zero. For the completeness of the circuit analysis, one needs to consider the effect of a finite rise time. If the rise time is t_r, then the output signal should be modified as

$$\Delta V_o(t) = [\Delta V_o(t)]_{t_r=0}\ (1 - e^{-t/t_r}) \qquad (5.10)$$

According to Equation 5.8, the output voltage $\Delta V_o(t)$ is complicated by the initial output voltage $V_o(0)$ from the circuit (i.e. the voltage when the return stroke starts). When the time constant R_fC_f

is small, the first term of Equation 5.8 approaches an asymptotic value $-V_o(0)$ rapidly. The output voltage is thus shifted by a DC level. On the other hand, if R_fC_f is large, the first term becomes vanishingly small and the effect of $V_o(0)$ then will be negligible. Since the time constant R_fC_f for fast antenna circuit used at NSSL is 100 μs, it is necessary to include the effect of $V_o(0)$ on the measured field changes. The rise time t_r for the circuit is about 1 μs, which is quite small and will only alter the output voltage slightly.

5.3.2 Comparison of Measured and Calculated Electric Fields

5.3.2.a Flash NSSL9. There are five return strokes in flash NSSL9 as indicated by the slow antenna record shown in Figure 2.6. Among them, the second, the fourth, and the fifth return stroke have high quality fast antenna waveforms. These three measured waveforms are shown in Figures 5.6, 5.7, and 5.8, respectively. The general shape of the waveforms consists of a very sharp initial peak at about 3 μs, followed by a decay down to an almost constant level (~5 V). High frequency oscillations (~0.5 MHz) of amplitude 1-2 V p-p are seen. The range of the reconstructed channel in Figure 2.3 is about 2.5 km. At this range, according to the model calculation, a typical waveform (as shown in Figure 5.6) for the second return stroke has a linear ramp portion with a negative slope starting at about 10 μs. However, such a downward trend does not exist in the measured data until after 60 μs. There are several possibilities for this apparent discrepancy: (1) the range of the channel reconstructed from thunder is in error, (2) the antenna electronics filter out the electrostatic field, or (3) the

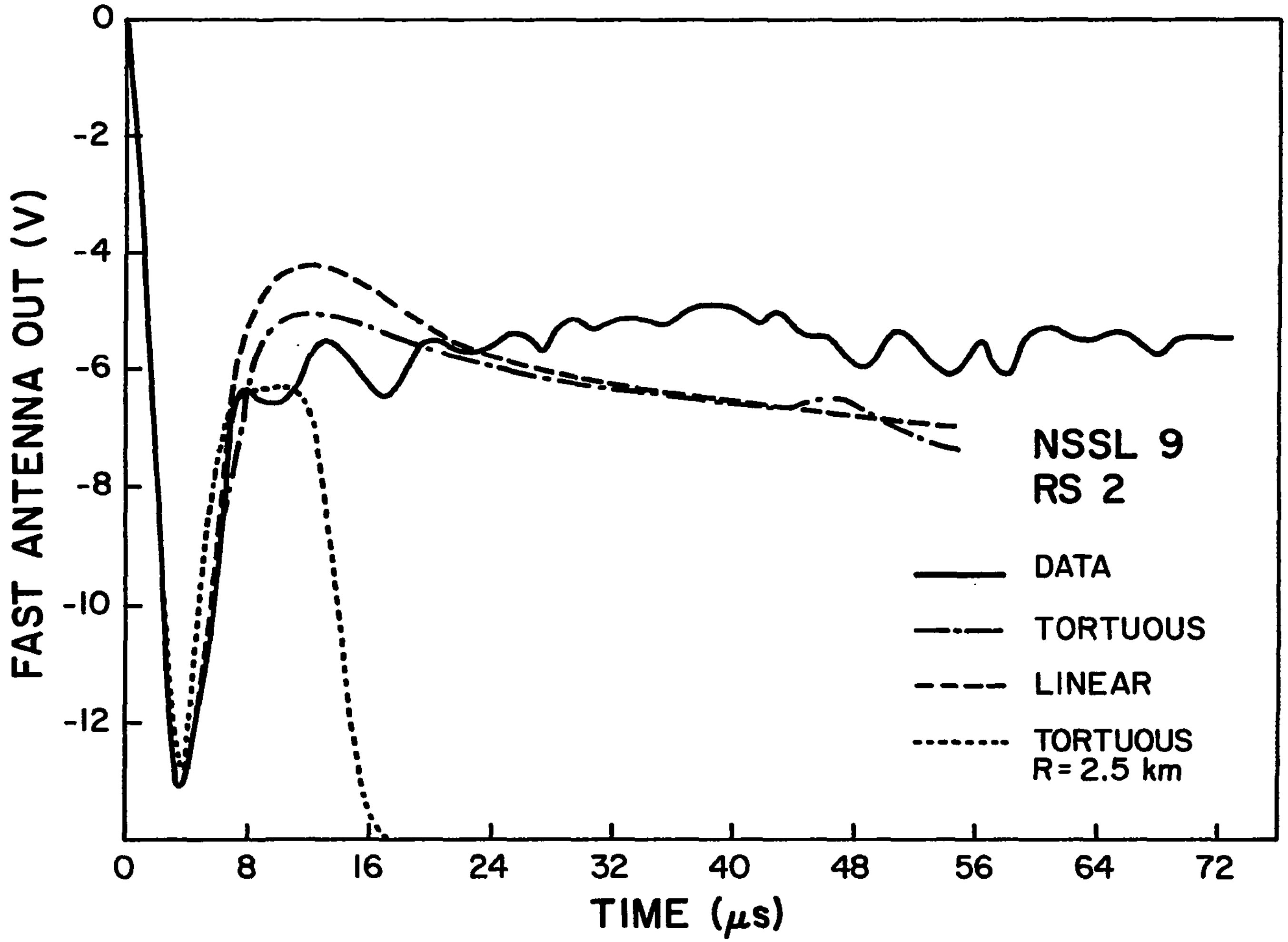

Figure 5.6 Calculated and measured electric field changes for flash NSSL9, R2. The results labelled tortuous and linear refer to ΔE calculated with the reconstructed tortuous and the equivalent vertical channel, respectively.

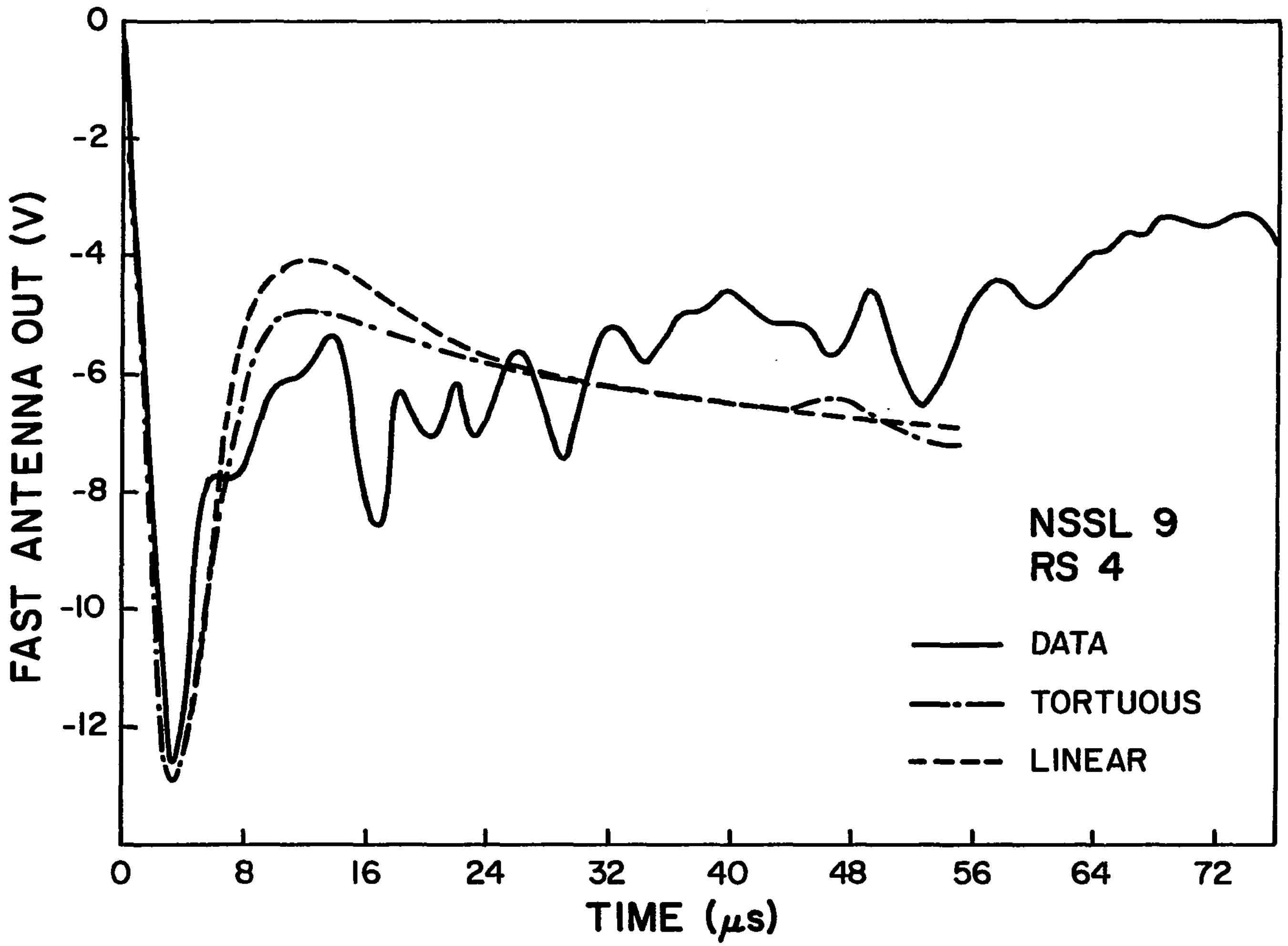

Figure 5.7 Calculated and measured electric field changes for flash NSSL9, R4. The results labelled tortuous and linear refer to ΔE calculated with the reconstructed tortuous and the equivalent vertical channel, respectively.

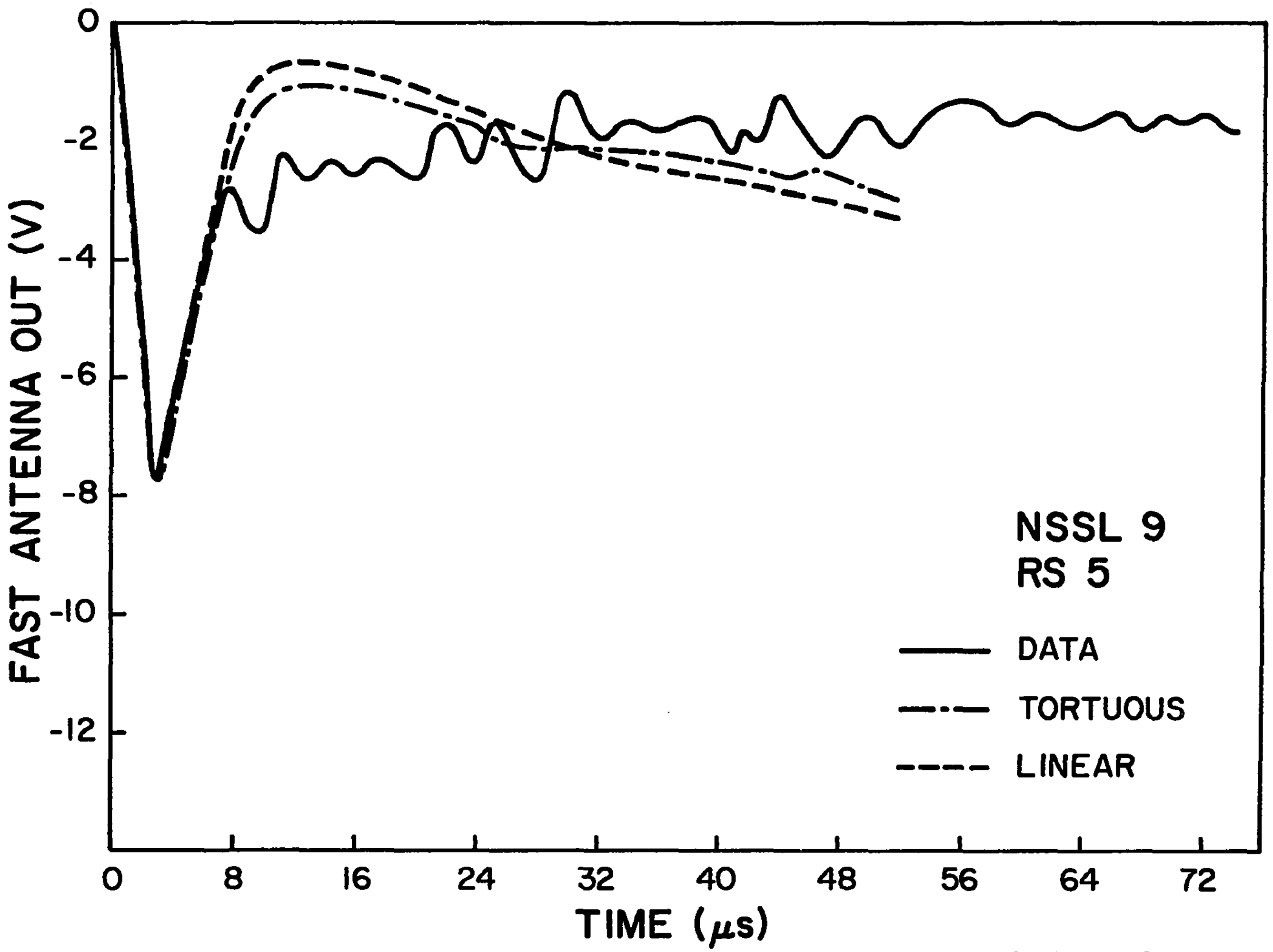

Figure 5.8 Calculated and measured electric field changes for flash NSSL9, R5. The results labelled tortuous and linear refer to ΔE calculated with the reconstructed tortuous and the equivalent vertical channel, respectively.

equivalent circuit analyzed in the previous section is oversimplified. The second and third possibilities cannot be verified without extensive circuit testing and analysis, an effort which is beyond the scope of this research. It is likely that the first possibility that the reconstructed channel is not associated with this particular flash is the source of error.

The direction of the leader electric field change proceeding the return stroke (Figure 2.6) indicates that the range of flash NSSL9 should be less than 5 km. However, starting time of the linear ramp portion of the fast antenna waveform suggests that the range should be greater than 10 km (Tiller et al., 1976). Using the reconstructed channel at 2.5 km (Figure 2.3), there is no way to fit the measured data no matter how the current parameters are chosen. It is therefore concluded that this reconstructed channel probably is not associated with the recorded electric field data.

After reexamining the acoustic data, it was found that another possible channel with a range of about 5 km can be associated with this flash. This channel geometry is shown in Figure 5.9. The electric field change calculated with this new channel agrees much better with the measured data as indicated in Figure 5.6. Consequently, this channel will be used hereafter for the analysis of NSSL9. The calculated results are shown with experimental data in Figures 5.6, 5.7, and 5.8 for comparison. Due to the lack of data for the initial voltage output $V_o(0)$ of the fast antenna circuit, the calculated voltage output $V_o(t)$ is arbitrarily adjusted by a DC level such that a good overall agreement with the measured waveform is obtained.

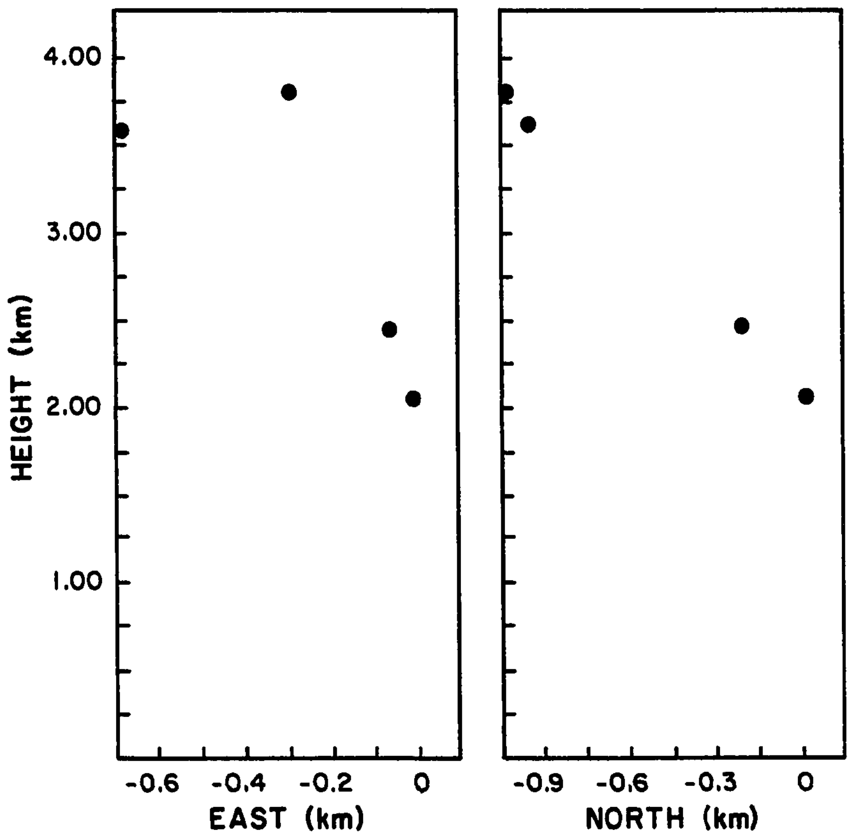

Figure 5.9 Another possible acoustic sources reconstructed from thunder data for NSSL flash 9, 8 June 79, 1537:41 CST. The origin is located at the ground strike point.

For the second and the fourth return strokes, the calculated results are obtained with the same current model parameters, i.e. I_0 = 15 kA, I_1 = 8 A/m, I_u = 0.05 kA. The agreement between the calculated and the measured data is fair. Some departure in the transition region and the linear ramp portion can be seen. The difference between $V_o(t)$ calculated with tortuous and linear channels is quite small for the initial peak and the linear ramp portion, but some significant departure can be found in the transition region. The linear channel gives a higher and narrower waveform for the transition region.

For the fifth return stroke, the initial peak is only about half the value of the previous two strokes. Therefore the current model parameters are adjusted to I_0 = 12 kA, I_1 = 5.5 A/m, and I_u = 0.05 kA. The agreement in the initial peak and the linear ramp portion is acceptable when the tortuous channel is used. Quite large differences are seen in the transition region. For the linear vertical channel, the overall agreement with measurement is not quite as good as that of the tortuous channel.

5.3.2.b Flash NSSL10. There are at least five return strokes in flash NSSL10 as indicated by the slow antenna output (Figure 2.7). However, only the fourth and fifth return strokes have good fast antenna data. The recorded fast antenna waveforms of these two return strokes are shown in Figures 5.10 and 5.11. The general waveform is very similar to the typical characteristics of a return stroke at a range of 10 km. It consists of a sharp initial peak at about 3 μs, followed by a rather broad transition region of about 40 μs and then a linear ramp.

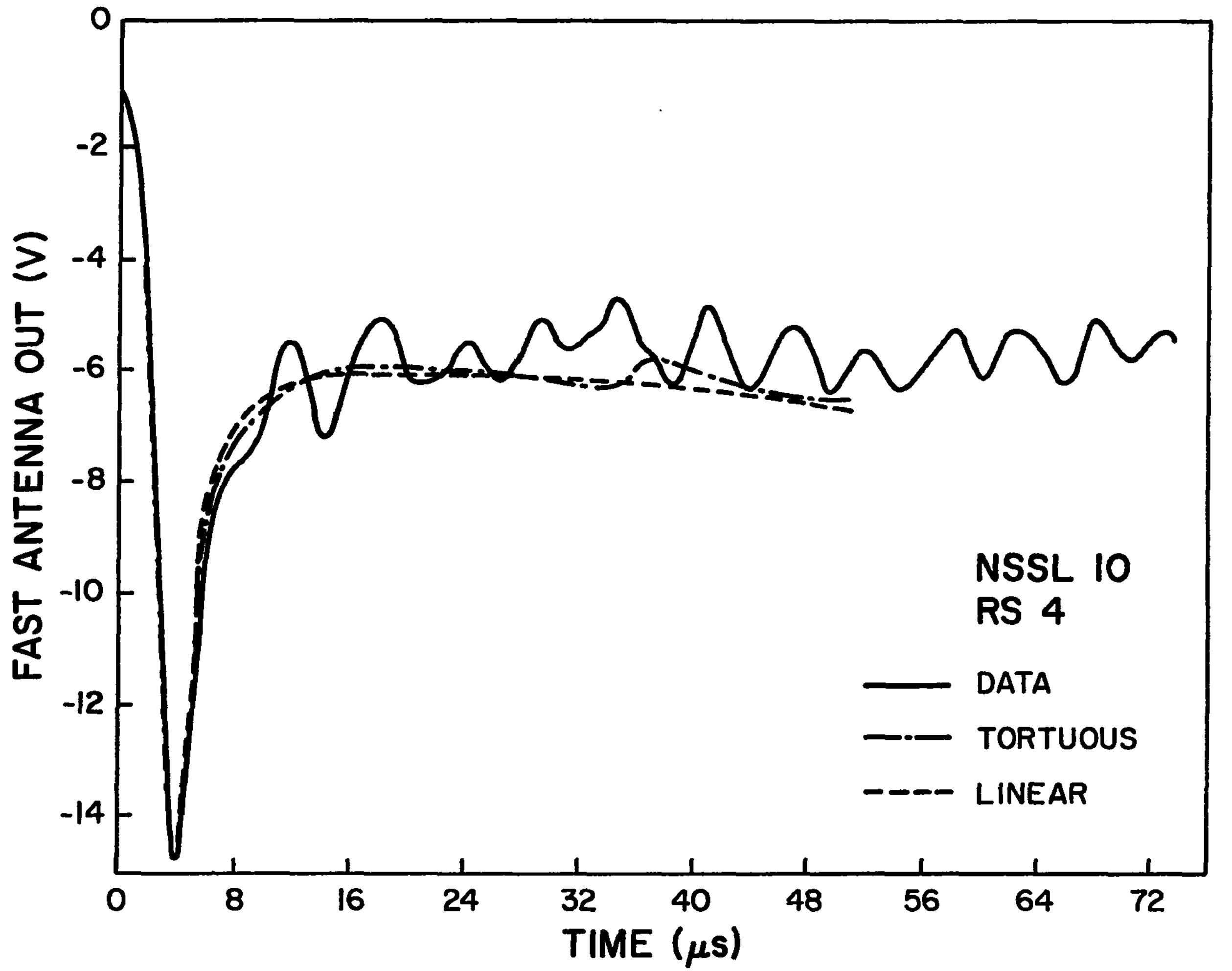

Figure 5.10 Calculated and measured electric field changes for flash NSSL10, R4. The results labelled tortuous and linear refer to ΔE calculated with the reconstructed tortuous and the equivalent vertical channel, respectively.

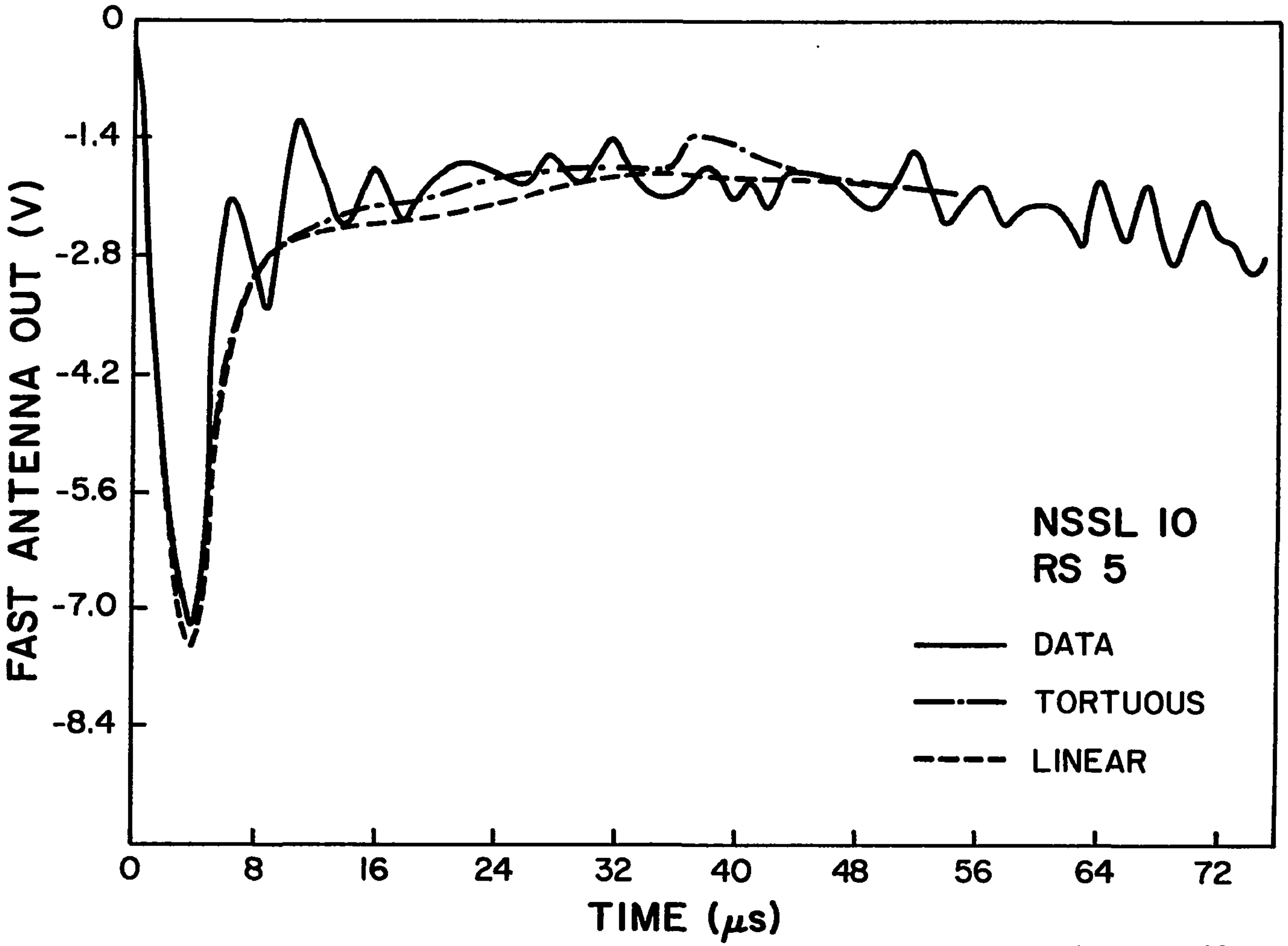

Figure 5.11 Calculated and measured electric field changes for flash NSSL10, R5. The results labelled tortuous and linear refer to ΔE calculated with the reconstructed tortuous and the equivalent vertical channel, respectively.

For the fourth return stroke, the calculated results are obtained with current model parameters of $I_0 = 35$ kA, $I_1 = 21$ A/m, $I_u = 2.5$ kA. The agreement between the calculated and measured data is very good. The difference between $V_o(t)$ calculated with tortuous and linear channels is very minor except for the hump at 36 μs due to channel tortuosity.

For the fifth return stroke, the initial peak is only about half the value of the previous one. Therefore the current model parameters are adjusted to $I_0 = 25$ kA, $I_1 = 21$ A/m, and $I_u = 2.5$ kA. Again the agreement between the calculated and measured data is very good. The difference between $V_o(t)$ calculated with tortuous channel and linear channel is very minor except for the same hump due to channel tortuosity.

From the analysis of flashes NSSL9 and NSSL10, the following can be concluded:

1. The impacts of channel tortuosity on the calculated waveforms are almost negligible because channels reconstructed with acoustic ray tracing do not provide information for the lower portion, which is most significant in the modified model of Lin et al. Furthermore, the acoustic ray tracing technique does not provide fine structure in the channel geometry, which is responsible for the high frequency oscillations.

2. As experienced in the analysis of flash NSSL9, it is possible to have more than one channel for a particular flash reconstructed from the acoustic data. Without additional corroborating data, it is impossible to resolve the ambiguity of these reconstructed channels.

3. According to the circuit analysis in Section 5.3.1, the adjustment of the calculated results by a DC level of $V_o(0)$ is legitimate only if the R_fC_f time constant of the fast antenna circuit is sufficiently large compared to the time duration of a return stroke. The time constant of the NSSL fast antenna is 100 μs, which is not long enough. Consequently, some deformation in the waveform is expected but was not incorporated in the analysis. Had a larger value, such as 1-3 ms been used, the output waveform would then have been unaffected by $V_o(0)$, and a direct comparison with the calculated electric field change would be possible.

5.4 Calculated Return Stroke Charge Transfer

Charge transferred by the return stroke in the first 100 μs can be calculated by integrating with respect to time the current at the ground. Using the three components of the current I_b, I_c, and I_u, one can calculate their separate contributions to the total charge transfer as follows:

$$Q_b = \int_o^T I_b \, dt = I_0 \left[\frac{1}{\alpha} - \frac{1}{\beta} - \frac{e^{-\alpha T}}{\alpha} + \frac{e^{-\beta T}}{\beta}\right] \tag{5.11}$$

$$Q_c = \int_o^T I_c \, dt = \frac{I_1}{C_1} \left\{\left(-\alpha' + \frac{C_1}{\frac{1}{v} + \frac{1}{c}}\right)^{-1} \left[e^{\left(-\alpha' + \frac{C_1}{\frac{1}{v} + \frac{1}{c}}\right)(T - t_{on})} - e^{\left(-\alpha' + \frac{C_1}{\frac{1}{v} + \frac{1}{c}}\right)(- t_{on})}\right]\right\} - \frac{I_1}{C_2} \left\{\left(-\beta' + \frac{C_2}{\frac{1}{v} + \frac{1}{c}}\right)^{-1} \left[e^{\left(-\beta' + \frac{C_2}{\frac{1}{v} + \frac{1}{c}}\right)(T - t_{on})} - e^{\left(-\beta' + \frac{C_2}{\frac{1}{v} + \frac{1}{c}}\right)(- t_{on})}\right]\right\} \tag{5.12}$$

$$Q_u = \int_0^T I_u \, dt = I_u T \tag{5.13}$$

where T = 100 μs, $C_1 = \frac{\alpha'}{v} + \frac{\alpha'}{c} - \frac{1}{\lambda}$, $C_2 = \frac{\beta'}{v} + \frac{\beta'}{c} - \frac{1}{\lambda}$ and all other parameters are those which were used in the previous sections to give the best fit to the data. Table 5.3 shows the calculated charge transfer for GNV1, GNV2, NSSL9, and NSSL10.

For the University of Florida data, charges transferred by the breakdown currents for both return strokes are comparable with the mean value of 0.093 C obtained by Lin et al. (1980). Charges transferred by the corona currents for both return strokes are the same and also comparable with the mean value of 0.56 C (Lin et al., 1980). Charge transferred by the uniform current for GNV1 depends on the channel geometry being used since a different uniform current is required to fit the data. This is not the case for GNV2 where the same current model fits both linear and tortuous channels. This is consistent with the conclusion that channel tortuosity has greater impact on distant flashes as indicated earlier in Chapter IV. The total charge transferred by each return stroke is also comparable with the mean value of 0.97 C obtained by Brook et al. (1962).

For the NSSL data, the charges transferred by flash NSSL9 are very small, and the contribution of the uniform-current was especially small. It is possible that this particular flash had unusually low current or the range of the reconstructed channel is in error. As mentioned before, the fast antenna waveform of NSSL9 indicates the range

TABLE 5.3. Calculated Charges Transferred by the Return Strokes During First 100 μs

Flash		Geometry	I_0 (kA)	I_1 (A/m)	I_u (kA)	Q_b (C)	Q_c (C)	Q_u (C)	Q_t (C)
GNV1		Tortuous	31	21	5.1	0.08	0.67	0.51	1.26
		Linear	31	21	3.1	0.08	0.67	0.31	1.06
GNV2		Tortuous	25	21	3.1	0.06	0.67	0.31	1.05
		Linear	25	21	3.1	0.06	0.67	0.31	1.05
NSSL9	R2	Tortuous or Linear	15	8	0.05	0.04	0.26	0.005	0.305
	R4	Tortuous or Linear	15	8	0.05	0.04	0.26	0.005	0.305
	R5	Tortuous or Linear	12	5.5	0.05	0.03	0.18	0.005	0.215
NSSL10	R4	Tortuous or Linear	35	21	2.5	0.09	0.67	0.25	1.01
	R5	Tortuous or Linear	25	21	2.5	0.06	0.67	0.25	0.98

should be greater than 10 km; nevertheless, the observed data were fitted with a channel at about 5 km; hence a rather small current was chosen. The charges transferred by NSSL10 are comparable with those calculated for the University of Florida data. Since only the upper portion of channel tortuosity was obatained for NSSL flashes, it has a small impact on the calculated electric waveform. Therefore there is no difference in the calculated charge transferred by the tortuous and linear channels.

CHAPTER VI

CONCLUSIONS AND RECOMMENDATIONS

The impact of channel tortuosity on radiated electric field changes during return strokes has been the focus of this research. Both theoretical analyses and experimental investigations were performed in order to gain new insights into this problem and to resolve some fundamental issues regarding lightning return stroke current models. The results obtained in this study and the experience gained during this research will be summarized and discussed here.

6.1 Conclusions

Channel tortuosity has direct and significant effects on radiated electric field waveforms. Major turning points in the radiation waveforms can be directly correlated to channel geometry for the current models being examined in this research. The degree of importance of channel tortuosity depends heavily upon the particular current model being adopted and the range of the lightning flash to the field point. In the compound exponential transmission line model, the calculated waveforms reflect clearly the tortuosity of the channel even though the current waveform is simple and smooth. On the contrary, using the more complex modified model of Lin et al., the impacts of channel tortuosity become smaller. But even then the impact is still quite significant, especially at large distances and if the tortuosity occurs in the lower portion of the channel. Using the modified current model of Lin et al., experimental data from both NSSL and University of Florida can be fitted reasonably well with theoretical results. It is difficult, if not impossible, to obtain acceptable agreement between calculated and measured data using the compound exponential transmission line model.

Differences in the calculated radiation waveforms can be seen between calculations using a tortuous channel and its equivalent linear vertical channel. After a very sharp initial peak, a rather smooth waveform is obtained when a linear vertical channel is used, while a tortuous channel introduces perturbations to the otherwise smooth waveform. The magnitude and the frequency of the fluctuations depend upon the degree and the height of channel tortuosity and the range to the field point. Channels with more tortuosity in the lower portion produce many high frequency oscillations in the radiation waveforms. A range dependence was also observed, i.e. a given channel tortuosity will have more significant impact on the ΔE waveform for field points at larger distances. Furthermore, different current model parameters will have to be used for the equivalent linear channel in order to fit the same measured data. This would result in a different total charge transferred by a given return stroke. Such a discrepancy depends upon the range of the field point and the degree of the channel tortuosity. Obviously, a very slanted or a highly tortuous channel cannot be made equivalent to any linear vertical channel.

Since channel tortuosity is important in analyzing radiation waveforms of return strokes, the techniques used for channel reconstruction should be evaluated with care and selected for best results. The two methods used in this research, i.e. acoustic ray tracing and multistation photography, each have their advantages and deficiencies. The greatest advantage of multistation photography is its ability to provide fine details in channel tortuosity, both in time and in space. However, it can only provide information for channels below the cloud base, which often is quite low (<2 km). Moreover, one needs at least two independent views of the lightning flash in order to obtain its channel coordinates. Since one cannot predict the location and time of occurrence of a lightning, this greatly reduces the possibility of obtaining usable channel geometry from multistation photographs. On the other hand, the acoustic ray tracing technique has the advantage of providing lightning channel information within the cloud. However, this technique gives fewer details of the channel, and it is extremely difficult to reconstruct lower portion (<1 km) of the channel (MacGorman, 1978). The accuracy of this technique depends on the knowledge of atmospheric conditions during the lightning flash, which may not be available. When lightning activity is intense and several flashes occur at almost the same time, it is impossible to associate the thunder signature with a particular flash, such as the situation encountered in the analysis of flash NSSL 9.

6.2 Recommendations for Future Research

According to the results obtained in this research, tortuosity in the lower portion of the channel is much more important than in the upper portion. Consequently, it is essential to have details of the lower portion of the channel, which can be provided by multistation photography but not by acoustic reconstruction. An ideal situation would be using both systems simultaneously. Such an experiment will allow mutual verification between these two techniques and can therefore provide more accurate channel geometry.

Instrument calibration and a knowledge of circuit responses are essential in analyzing quantitatively measured radiation waveforms. To insure that essential information arising from channel tortuosity will not be lost in the recorded data, the fast antenna system needs to be carefully calibrated with respect to output gain, waveform distortion, frequency response, etc. The instrument should also be placed in a low-noise environment.

Simultaneous measurements of other components of radiation fields from the return stroke will provide much more useful information for the study of the impacts of channel tortuosity. For instance, horizontal electric field changes above the ground (ΔE_x and ΔE_y) or vertical magnetic field changes (ΔB_z) can provide information about channel tortuosity because, in principal, a vertical linear channel would have zero values for these field components. The techniques of measuring these forementioned components of radiation from a return stroke may not be straightfoward, but should be worth further investigation.

There are two areas of future research along the lines of this study that are very promising. The first is to calculate field components other than ΔE_z for a return stroke. According to the mathematical algorithm developed in Chapter III, only minor modification of the EMFIELD code is required. The second area is to assess the impact of channel tortuosity on the accuracy of lightning direction finders. Two different techniques are presently being used for lightning direction finding; one uses the initial peaks (Krider et al., 1976) of the magnetic fields, and the other uses magnetic fields at a fixed-frequency (Horner, 1954, 1957). According to the results of this dissertation, it is found that the initial peak usually is not very sensitive to channel tortuosity. It is therefore speculated (Uman, 1982) that the initial peak method may yield more accurate results. This issue can be resolved by calculating the relative sensitivity of the initial peak and the fixed-frequency field amplitude to the tortuosity of the lightning channel.

REFERENCES

Brook, M., N. Kitagawa, and F.J. Workman, Quantitative Study of Strokes and Continuing Currents in Lightning Discharges to Ground, J. Geophys. Res., 67, 649-659, 1962.

Brook, M., Lightning Measurements and Instrumentation, Conference on Lightning and Static Electricity, Las Vegas, Nevada, 1972.

Bruce, C.E.R., and R.H. Golde, The Lightning Discharge, J. Inst. Elec. Eng., 88, 487-520, 1941.

Chameides, W.L., D.H. Stedman, R.R. Dickerson, D.W. Rusch, and R.J. Cicerone, NO_x Production in Lightning, J. Atmos. Sci., 34, 143-149, 1977.

Cohen, Ed. I.B., Benjamin Franklin's Experiments, Harvard University Press, 1941.

Dennis, A.S., and E.T. Pierce, The Return Stroke of the Lightning Flash to Earth as a Source of VLF Atmospherics, Radio Science, J. Res. Nat. Bur. Stand., 68D, 777-794, 1964.

DISSPLA User's Manual Version 8.2, Display Integrated Software System and Plotting Language, Integrated Software Systems Corporation, San Diego, California, 1978.

Doviak, R.J., D.S. Zrnic, and D.S. Sirmans, Doppler Weather Radar, Proc. IEEE, 67, 1522-1553, 1979.

Few, A.A., Jr., Thunder, Ph.D. Thesis, Rice University, Houston, Texas, 1968.

Few, A.A., Power Spectrum of Thunder, J. Geophys. Res., 74, 6926-6934, 1969.

Few, A.A., Lightning Channel Reconstruction from Thunder Measurements, J. Geophys. Res., 75, 7517-7523, 1970.

Few, A.A., Thunder Signatures, E⊕S Trans. AGU, 55, 508-514, 1974.

Few, A.A., Thunder, Scientific American, 233, 80-91, 1975.

Few, A.A., A.J. Dessler, D.J. Latham, and M. Brook, A Dominant 200-Hertz Peak in the Acoustic Spectrum of Thunder, J. Geophys. Res., 72, 6149-6154, 1967.

Few, A.A., and T.L. Teer, The Accuracy of Acoustic Reconstructions of Lightning Channels, J. Geophys. Res., 79, 5007-5011, 1974.

Fowler, R.G., Nonlinear Electron Acoustic Waves, Part I and Part II, Advances in Electronics and Electron Physics, 41, Academic Press, 1976.

Fröberg, C.E., Introduction to Numerical Analysis, University of Lund, Sweden, 1964.

Griffiths, R.F., and C.T. Phelps, A Model for Lightning Initiation Arising from Positive Corona Streamer Development, J. Geophys. Res., 81, 3671-3676, 1976.

Hill, R.D., Analysis of Irregular Paths of Lightning Channels, J. Geophys. Res., 73, 1897-1906, 1968.

Hill, R.D., Thunder, in Lightning, Vol. 1, Physics of Lightning, ed. by R.H. Golde, Academic Press, N.Y., 385-408, 1977.

Hill, R.D., and R.G. Rinker, Production of Nitrate Ions and Other Trace Species by Lightning, J. Geophys. Res., 86, 3203-3206, 1981.

Jordan, D.J., and M.A. Uman, Variations of Light Intensity with Height and Time from Subsequent Return Strokes, EOS Trans. AGU, 61, 977, 1980.

Kittagawa, N., and M. Brook, A Comparison of Intracloud and Cloud-to-Ground Lightning Discharges, J. Geophys. Res., 65, 1189-1201, 1960.

Krehbiel, P.R., M. Brook, and R.A. McCrory, An Analysis of the Charge Structure of Lightning Discharges to Ground, J. Geophys. Res., 84, 2432-2456, 1979.

Krider, E.P., R.C. Noggle, and M.A. Uman, A Gated, Wideband Magnetic Direction Finder for Lightning Return Strokes, J. Appl. Meteor., 15, 301-306, 1976.

LeVine, D.M., and R. Meneghini, Electromagnetic Fields Radiated from a Lightning Return Stroke: Application of an Exact Solution to Maxwell's Equations, J. Geophys. Res., 83, 2377-2384, 1978.

LeVine, D.M., and R. Meneghini, Simulation of Radiation from Lightning Strokes: The Effects of Tortuosity, Radio Sci., 13, 801-809, 1978.

Lin, Y.T., M.A. Uman, and R.B. Standler, Lightning Return Stroke Models, J. Geophys. Res., 85, 1571-1583, 1980.

Little, P.F., Transmission Line Representation of a Lightning Return Stroke, J. Phys. D, 11, 1893-1910, 1978.

Little, P.F., The Effect of Altitude on Lightning Hazards to Aircraft, Proceedings of the 15th European Conference on Lightning Protection, Vol. 2, Institute of High Voltage Research, Uppsala University, Sweden, 1979.

MacGorman, D.R., Lightning Location in a Colorado Thunderstorm, M.S. Thesis, Rice University, Houston, Texas, 1977.

MacGorman, D.R., Lightning Location in a Storm with Strong Wind Shear, Ph.D. Thesis, Rice University, Houston, Texas, 1978.

Master, M.J., M.A. Uman, Y.T. Lin, and R.B. Standler, Calculations of Lightning Return Stroke Electric and Magnetic Fields Above Ground, J. Geophys. Res., 86, 12127-12132, 1981.

McLain, D.K., and M.A. Uman, Exact Expression and Moment Approximation for the Electric Field Intensity of the Lightning Return Stroke, J. Geophys. Res., 76, 2101-2105, 1971.

Nasser, E., Fundamentals of Gaseous Ionization and Plasma Electronics, Wiley-Interscience, 1971.

Price, G.H., and E.T. Pierce, The Modeling of Channel Current in the Lightning Return Stroke, Radio Sci., 12, 381-338, 1977.

Salanave, L.E., Lightning and Its Spectrum, The University of Arizona Press, 1980.

Schonland, B.F.J., The Lightning Discharge, Handbuch der Physik, 22, 576-628, Berlin, 1956.

Strawe, D.F., Non-Linear Modeling of Lightning Return Strokes, Proceedings of the FAA/FIT Workshop on Grounding and Lightning Technology, 6-8 March 1979, Melbourne, Florida, Report FAA-RD-79-6, pp. 9-15.

Taylor, W.L., A VHF Technique for Space-Time Mapping of Lightning Discharge Processes, IAGA/IAMAP, Seattle, Washington, August 22 - September 3, 1977.

Teer, T.L., Acoustic Profiling--A Lightning Reconstruction Technique, M.S. Thesis, Rice University, Houston, Texas, 1972.

Teer, T.L., Lightning Channel Structure Inside an Arizona Thunderstorm, Ph.D. Thesis, Rice University, Houston, Texas, 1973.

Uman, M.A., Lightning, McGraw-Hill, New York, 1969.

Uman, M.A., Lightning Return Stroke Models, 6th International Conference on Atmospheric Electricity, Manchester, England, July 1980.

Uman, M.A., and D.K. McLain, Magnetic Field of Lightning Return Stroke, J. Geophys. Res., 74, 6899-6909, 1969.

Uman, M.A., and D.K. McLain, Lightning Return Stroke Current from Magnetic and Radiation Field Measurements, J. Geophys. Res., 75, 5143-5147, 1970.

Uman, M.A., and D.K. McLain, R.J. Fisher, and E.P. Krider, Electric Field Intensity of the Lightning Return Stroke, J. Geophys. Res., 78, 3523-3529, 1973a.

Uman, M.A., D.K. McLain, R.J. Fisher, and E.P. Krider, Currents in Florida Lightning Return Strokes, J. Geophys. Res., 78, 3530-3537, 1973b.

Viemeister, P.E., The Lightning Book, The MIT Press, 1972.

Wagner, C.F., Determination of the Wavefront of Lightning Stroke Current from Field Measurements, Trans. Amer. Inst. Elec. Eng., 79(3), 581-589, 1960.

Wagner, C.F., and A.R. Hileman, The Lightning Stroke, 11, Trans. Amer. Inst. Elec. Eng., 80(3), 622-642, 1961.

APPENDIX I

RAY TRACING METHODOLOGY

There are three steps involved in the procedures for channel reconstruction from acoustic data. The first step is determining the time difference for thunder originating from a particular mesoscale segment of the lightning channel to reach two microphones in the array. The time delays are determined by cross-correlation analysis of two random variables x,y. The cross-correlation coefficient is defined as

$$\rho_{xy} = \frac{\sigma_{xy}}{\sigma_x \sigma_y} \tag{A.1}$$

where

$$\sigma_{xy}(\tau) = \lim_{T\to\infty} \frac{1}{T} \int_o^T x(t)\, y(t + \tau)\, d\tau \tag{A.2}$$

$$\sigma_x^2(\tau) = \lim_{T\to\infty} \frac{1}{T} \int_o^T x(t)\, x(t + \tau)\, d\tau \tag{A.3}$$

$$\sigma_y^2(\tau) = \lim_{T\to\infty} \frac{1}{T} \int_o^T y(t)\, y(t + \tau)\, d\tau \tag{A.4}$$

and τ is the time delay to be determined. The maximum T allowed here is 512 ms, which is the length of two digital data records. For the particular application here, the random variables x,y are the voltage output recorded from each microphone. In principle, the relative time lag between two microphones occurs when the cross-correlation coefficient is at its maximum value, since the two waveforms are most similar then. There are two possible difficulties in this analysis: (1) the data may contain noises, such as wind and train whistles, that have amplitudes comparable to thunder signal; (2) thunder signals from two or more sources may arrive at the microphones at nearly the same time, causing interference and confusion in the cross-correlation analysis.

The second step is determining the direction of arrival after the time delay has been obtained. The azimuth ϕ and elevation angle θ of the acoustic ray associated with the signals arriving at the microphones can be calculated with the following formula derived by MacGorman (1978). For a square array, and assuming there is no wind,

$$\phi = \tan^{-1} \left(\frac{\tau_{23}}{\tau_{12}}\right) \tag{A.5}$$

$$\theta = \cos^{-1} \left(\frac{c\ \tau_{23}}{D \sin \phi}\right) \tag{A.6}$$

where τ_{ij} is the time delay between microphone i and microphone j, c is the speed of sound at the array and D is the length of the side of the array. When there is a horizontal wind near the surface, Equation 2.5 remains unchanged and Equation 2.6 becomes

$$\theta = \cos^{-1} \left[\frac{c}{D \sin \phi/\tau_{23} - u \cos (\phi - \phi')}\right] \tag{A.7}$$

where u is the speed of the wind and ϕ' is its azimuth angle. The above equations for θ and ϕ are given in terms of τ_{12} and τ_{23} only. Actually they can be calculated from any pair of the time delays because of geometrical constraints of the square array.

The third step is retracing the acoustic ray path through the atmosphere to its source point. The position of the acoustic ray at time t is determined by

$$\vec{r}(t) = \int_0^t (c\,\hat{n} + \vec{u})\,dt' \tag{A.8}$$

where $\hat{n}$ is the unit vector in the direction of ray propagation, measured in a reference frame moving with the wind $\vec{u}$. The upper limit t in the integration is the time required for thunder to propagate to the array, given by the difference in arrival times of the thunder and electric field change of lightning measured by a slow antenna near the microphones.

If the atmosphere were uniform, the ray path would be a straight line, and the integration back through the atmosphere to the source point would be simple. However, the real atmosphere is continuously varying with time and altitude, causing the ray propagation velocity to change along its path. Few (1968) developed a procedure for ray tracing in a horizontally stratified atmosphere which will be briefly described here. The atmosphere is assumed to consist of many thin layers; and the atmospheric conditions are approximated by constant parameters within each layer. The acoustic ray propagates in a straight path within each layer and bending in the ray path will occur only at the interface between two layers. Since energy and momentum of the acoustic wave must be continuous across the interface, the amount of bending of the ray path can be determined by Snell's law of refraction. This is equivalent to requiring the phase velocities along the x and y axis in two adjacent layers to be equal at the interface. If the layers are made infinitesimally thin, equations can be found for a continuously changing atmosphere. In the ray tracing program developed by MacGorman (1978), the values of horizontal wind speed and atmospheric temperature were specified at various heights. The vertical changes of these quantities were assumed to be linear between heights.

Errors in lightning channel reconstruction do exist. The sources of error arise from: (1) inaccuracy in the microphone array coordinates, (2) uncertainty of the reference timing of lightning for time lag calculations, (3) uncertainty in time lags calculated by the cross-correlation method, and (4) departure of the model atmosphere from the real world. Each of these sources of error has been examined in detail by MacGorman (1978).

APPENDIX II

A. LISTING OF EMFIELD CODE

```
C*****PROGRAM EMFIELD
C*****THIS PROGRAM IS WRITTEN FOR SOLVING MAXWELL'S EQUATIONS DURING
C*****LIGHTNING RETURN STROKES. CURRENT VERSION OF THIS CODE CAN ONLY
C*****CALCULATE Z-COMPONENT OF THE ELECTRIC FIELDS. IT IS DEVELOPED
C*****AT ARGONNE NATIONAL LABORATORY BY MARY Y.P. LIAW WITH TECHNICAL
C*****ASSISTANCE OF J.R. LIAW UNDER IBM 370/3033 ENVIRONMENT.
C*****THIS CODE IS FIXED DIMENSIONED FOR 6500 SPATIAL POINTS AND 1200
C*****TIME STEPS. LOGICAL UNIT FOR INPUT IS 5 AND GENERAL OUTPUT IS 6.
C*****LOGICAL UNIT 8 IS USED FOR FINAL CALCULATED ELECTRIC FIELD
C*****OUTPUT AND UNIT 16 AND 26 ARE FOR CURRENT OUTPUTS AT Z=0 AND
C*****Z=1.5KM ABOVE THE GROUND. GRAPHIC OUTPUTS FROM DISSPLA WILL BE
C*****ALSO CREATED DURING THE RUN.
      IMPLICIT REAL*8(A-H,O-Z)
      REAL*8 LT
      REAL*8 LABEL,CASE,KASE
      REAL*4 X2,Y2,Z2
      DIMENSION EZ(1200),X(6500),Y(6500),Z(6500),LT(6500),X1(300),
     *Y1(300),Z1(300),X2(300),Y2(300),Z2(300),
     *ECONA(1200),ECONB(1200),ECOND(1200),ECONE(1200),
     *CASE(10),LABEL(8),KASE(10)
      COMMON/FLASH/DELT,TPULSE,RFG,TMAX,NT,IRTD,K1,K2,K3
      COMMON/CONSTS/C1,C2,C3,C4,C5,C6,C7,C8,TPC,IPZH
      COMMON/SPEED/V,C
      COMMON/CHANEL/X,Y,Z,LT,DLI,FZO,MAX,LIN,KNT,IBUG,ICUR,IDB
      COMMON/PLOT/TMAXP,EMIN,EMAX,MARK
      COMMON/ECONS/ECONA,ECONB,ECOND,ECONE
      DATA KASE(2)/8H CHANNEL/
      DATA KASE(3)/8H GEOMETR/
      DATA KASE(4)/8HY$'     /
C*****START CASE ANALYSIS
      C=3.0D+8
11111 CONTINUE
C*****INPUT SOLUTION SPECIFICATIONS
      READ(5,5) (CASE(I),I=1,9)
    5 FORMAT(9A8)
      WRITE(6,6) (CASE(I),I=1,9)
    6 FORMAT(1H1,'***** ',9A8,' *****',//)
      READ(5,10) IFLASH,IDATE,MAXIP,IEZ,IEX,IEY,IBX,IBY,IBZ,KNT,IBUG,
```

```
     *IRTD,ICUR,ISCA
   10 FORMAT(14I5)
      WRITE(6,11) IFLASH,IDATE,MAXIP,IEZ,IEX,IEY,IBX,IBY,IBZ,KNT,IBUG,
     *IRTD,ICUR,ISCA
   11 FORMAT(1H0,'***** SOLUTION SPECIFICATIONS *****',//,
     *I12,'  IFLASH=NUMBER OF RETURN STROKES TO BE CALCULATED',/,
     *I12,'  IDATE=TIME AND DATE OF THE RETURN STROKES ANALIZED',/,
     *I12,'  MAXIP=INPUT POINTS FOR CHANNEL GEOMETRY MINIMUM=2',/,
     *I12,'  IEZ=FLAG FOR EZ CALCULATION 1/0 FOR YES/NO',/,
     *I12,'  IEX=FLAG FOR EX CALCULATION 1/0 FOR YES/NO',/,
     *I12,'  IEY=FLAG FOR EY CALCULATION 1/0 FOR YES/NO',/,
     *I12,'  IBX=FLAG FOR BX CALCULATION 1/0 FOR YES/NO',/,
     *I12,'  IBY=FLAG FOR BY CALCULATION 1/0 FOR YES/NO',/,
     *I12,'  IBZ=FLAG FOR BZ CALCULATION 1/0 FOR YES/NO',/,
     *I12,'  KNT=FLAG FOR CURRENT MODEL DEBUG ONLY 1/0 FOR YES/NO',/,
     *I12,'  IBUG=FLAG FOR GENERAL DEBUG ONLY 1/0 FOR YES/NO',/,
     *I12,'  IRTD=FLAG FOR RETARDED TIME IN CURRENT 1/0=YES/NO',/,
     *I12,'  ICUR=FLAG FOR LIN CURRENT AT GROUND AND 1500 METER',/,
     *I12,'  ISCA=FLAG FOR SELF-SCALING PLOT OF EZ  1/0=YES/NO',/)
C*****IF ICUR=1 WRITE CURRENT COMPONENTS AT Z=DLI AND C8 METERS
      IF(ICUR.EQ.0) GO TO 23
      WRITE(16,5) (CASE(I),I=1,9)
      WRITE(16,13)
   13 FORMAT(1H0,//,2X,'L',4X,'I',5X,'TIME',9X,'IB',9X,'IC',9X,'IU',/)
      WRITE(26,5) (CASE(I),I=1,9)
      WRITE(26,13)
   23 CONTINUE
C*****INPUT CONSTANT PARAMETERS FOR CURRENT MODEL
      READ(5,20) C1,C2,C3,C4,C5,C6,C7,V,C8,IPZH
   20 FORMAT(9D8.2,I2)
C*****TPC IS THE TIME TO PEAK IN BREAKDOWN PULSE WHEN CORONA STARTED
      TPC=1.1D-6
      WRITE(6,21) C1,C2,C3,C4,C5,C6,C7,V,C8,TPC,IPZH
   21 FORMAT(1H0,'***** CONSTANT PARAMETERS *****',//,
     *1PD12.2,'  C1=I0 AMPERE IN BREAKDOWN PULSE CURRENT',/,
     *1PD12.2,'  C2=I1 AMPERE/METER IN CORONA CURRENT MODEL',/,
     *1PD12.2,'  C3=ALPHA TIME CONSTANT IN BREAKDOWN PULSE MODEL',/,
     *1PD12.2,'  C4=BETA TIME CONSTANT IN BREAKDOWN PULSE MODEL',/,
     *1PD12.2,'  C5=ALPHA TIME CONSTANT IN CORONA CURRENT MODEL',/,
     *1PD12.2,'  C6=BETA TIME CONSTANT IN CORONA CURRENT MODEL',/,
     *1PD12.2,'  C7=IU AMPERE UNIFORM CURRENT IN CHANNEL',/,
     *1PD12.2,'  V=SPEED OF BREAKDOWN PULSE FRONT PROPAGATION',/,
     *1PD12.2,'  C8=CORONA OR BREAKDOWN CURRENT DECAY HALF-HEIGHT',/,
     *1PD12.2,'  TPC=TIME TO PEAK IN BREAKDOWN FOR CORONA INITIATION',/,
     *I12,    '  IPZH=1/0 FOR YES/NO BREAKDOWN PULSE DECAY WITH Z',/)
C*****INPUT FIELD POINT AND NUMERICAL SCALES
      READ(5,30) FX,FY,FZ,DXYZ,DLI,DELT,TPULSE,RFG
   30 FORMAT(8D8.2)
      WRITE(6,31) FX,FY,FZ,DXYZ,DLI,DELT,TPULSE,RFG
   31 FORMAT(1H0,'***** FIELD POINT AND NUMERICAL SCALES *****',//,
     *1PD12.2,'  FX=X VALUE OF FILED POINT',/,
```

```
     *1PD12.2,'  FY=Y VALUE OF FIELD POINT',/,
     *1PD12.2,'  FZ=Z VALUE OF FIELD POINT',/,
     *1PD12.2,'  DXYZ=DX/DY/DZ FOR SPATIAL DERIVATIVE',/,
     *1PD12.2,'  DLI=DL FOR CHANNEL SEGMENTS USED IN INTEGRATION',/,
     *1PD12.2,'  DELT=DT FOR TIME INTERVALS IN FIELD EVALUATION',/,
     *1PD12.2,'  TPULSE=TOTAL TIME RANGE IN FIELD CALCULATION',/
     *1PD12.2,'  RFG=SHORTEST DISTANCE BETWEEN CHANNEL AND FIELD',/)
C*****INPUT FLAGS FOR PLOTS
      READ(5,35) XMIN,XMAX,ZMIN,ZMAX,TMAXP,EMIN,EMAX,MARK,IPCG
   35 FORMAT(7D8.2,2I5)
      WRITE(6,36) XMIN,XMAX,ZMIN,ZMAX,TMAXP,EMIN,EMAX,MARK,IPCG
   36 FORMAT(1H0,'***** LIMITS FOR PLOTS *****',//,
     *1PD12.2,'  XMIN=MINIMUM X/Y VALUE FOR GEOMETRY PLOTS',/,
     *1PD12.2,'  XMAX=MAXIMUM X/Y VALUE FOR GEOMETRY PLOTS',/,
     *1PD12.2,'  ZMIN=MINIMUM Z VALUE FOR GEOMETRY PLOTS',/,
     *1PD12.2,'  ZMAX=MAXIMUM Z VALUE FOR GEOMETRY PLOTS',/,
     *1PD12.2,'  TMAXP=MAXIMUM TIME FOR FIELD CHANGE PLOTS',/,
     *1PD12.2,'  EMIN=MINIMUM ELECTRIC FIELD IN PLOTS',/,
     *1PD12.2,'  EMAX=MAXIMUM ELECTRIC FIELD IN PLOTS',/,
     *I12,'  MARK=CURVE AND SYMBOL SELECTION -1/0/1',/,
     *I12,'  IPCG=FLAG FOR CHANNEL GEOMETRY PLOT 1/0=YES/NO',/)
      NT=TPULSE/DELT
      NT=NT+1
C*****INPUT CHANNEL GEOMETRY
C*****LIN=1/0 IS THE FLAG FOR LINEAR/ZIGZAG CHANNEL GEOMETRY
      READ(5,39) LIN
   39 FORMAT(I5)
      WRITE(6,37) LIN
   37 FORMAT(1H0,I12,'  LIN=1/0 IS THE FLAG FOR LINEAR/ZIGZAG')
      WRITE(6,38)
   38 FORMAT(1H1,'***** INPUT CHANNEL GEOMETRY *****',//,
     *2X,'I',5X,'X',9X,'Y',9X,'Z',/)
      DO 50 I=1,MAXIP
      READ(5,40) IP,X1(I),Y1(I),Z1(I)
C*****THE ACTUAL COORDINATES OF CHANNEL DEPENDS ON THE REFERENCE
C*****ORIGION OF FIELD AND SOURCE POINTS
      X1(I)=X1(I)
      Y1(I)=Y1(I)
      WRITE(6,40) IP,X1(I),Y1(I),Z1(I)
   40 FORMAT(I3,3F10.2)
   50 CONTINUE
      L1=1
C*****X,Y,Z ARE THE FINE MESH POINTS AND X1,Y1,Z1 ARE INPUT CHANNEL
      X(1)=X1(1)
      Y(1)=Y1(1)
      Z(1)=Z1(1)
      NI1=MAXIP-1
      WRITE(6,52)
   52 FORMAT(1H0,'***** CHANNEL SEGMENT LENGTH *****',//,
     *5X,'DX',10X,'DY',10X,'DZ',9X,'DL',9X,'IC',/)
      DO 80 I=1,NI1
```

```
      I1=I+1
      DX=X1(I1)-X1(I)
      DY=Y1(I1)-Y1(I)
      DZ=Z1(I1)-Z1(I)
      DL=DSQRT(DX*DX+DY*DY+DZ*DZ)
      IC=DL/DLI
      IF(IC.LT.1) IC=1
      WRITE(6,55) DX,DY,DZ,DL,IC
   55 FORMAT(4D12.5,I5)
      DX=DX/IC
      DY=DY/IC
      DZ=DZ/IC
      DO 75 J=1,IC
      L=L1
      L1=L+1
      X(L1)=X(L)+DX
      Y(L1)=Y(L)+DY
      Z(L1)=Z(L)+DZ
      IF(IBUG.EQ.1) X(L1),Y(L1),Z(L1)
   65 FORMAT(I5,3D12.5)
   75 CONTINUE
      IF(X(L1).LT.X1(I1)) X(L1)=X1(I1)
      IF(Y(L1).LT.Y1(I1)) Y(L1)=Y1(I1)
      IF(Z(L1).LT.Z1(I1)) Z(L1)=Z1(I1)
   80 CONTINUE
      MAX=L1
      LT(1)=0.D0
      MAX1=MAX-1
C*****CALCULATE LENGTH LI FROM GROUND TO THE ITH SEGMENT FOR EACH I
      DO 100 I=1,MAX1
      I1=I+1
      DX=X(I1)-X(I)
      DY=Y(I1)-Y(I)
      DZ=Z(I1)-Z(I)
      LT(I1)=DSQRT(DX*DX+DY*DY+DZ*DZ)
      LT(I1)=LT(I1)+LT(I)
  100 CONTINUE
C*****CALCULATE TIME FOR CURRENT FRONT TO REACH CLOUD BASE
      TOPC=LT(I1)/C
      TOPV=LT(I1)/V
      VOC=V/C
      RANGE=DSQRT((FX-X(1))**2+(FY-Y(1))**2+(FZ-Z(1))**2)
C*****SHIFT RFG BY DXYZ SO THAT THE RETARDED TIME IS MININUM FOR
C*****BOTH FILED POINT AND ITS 6 NEIGHBOR POINTS
C*****AVOID USING TOO LAGRE DXYZ TO MINIMIZE PROPAGATION TIME EFFECT
C*****ON THE FILED EVALUATION PROCESS
      RFG=RANGE-DXYZ
      TRTD=RANGE/C
      K1=2.0E-6/DELT+1
      K2=TOPC/DELT+1
      K3=TOPV/DELT+1
```

```
      WRITE(6,105) VOC,TOPC,TOPV,RANGE,TRTD,K1,K2,K3,NT
  105 FORMAT(1H0,'***** FLASH TIME CHARACTERISTICS *****',//,
     *1PD12.2,'  VOC=CURRENT FRONT SPEED/SPEED OF LIGHT',/,
     *1PD12.2,'  TOPC=TIME FOR CURRENT FRONT TO REACH TOP',/,
     *1PD12.2,'  TOPV=TIME FOR CURRENT FRONT TO REACH TOP FOR V',/,
     *1PD12.2,'  RANGE=DISTANCE BETWEEN CHANNEL GROUND AND FIELD',/,
     *1PD12.2,'  TRTD=RETARDING TIME FROM CHANNEL GROUND TO FIELD',/,
     *I12,'  K1=TIME STEP WHEN TIME IS 2.0 MICRO SEC',/,
     *I12,'  K2=TIME STEP WHEN TIME IS TOPC SEC',/,
     *I12,'  K3=TIME STEP WHEN TIME IS TOPV SEC',/,
     *I12,'  NT=TOTAL TIME STEP USED IN TPULSE SEC',/)
C*****OUTPUT CHANNEL GEOMETRY
      WRITE(6,110)
  110 FORMAT(1H1,15X,'CHANNEL GEOMETRY',/,5X,'I          X           Y',
     *'           Z           LT',/)
      WRITE(6,120) (I,X(I),Y(I),Z(I),LT(I),I=1,MAX,10)
  120 FORMAT(1H ,I5,4F12.2)
C*****INITIATE DISSPLA PLOTTING ROUTINES
      CALL STRTPL
      CALL BGNPL(-1)
      CALL NOBRDR
C*****START PLOT CHANNEL GEOMETRY
      IF(IPCG.EQ.0) GO TO 299
C*****X2,Y2,Z2 ARE COORDINATES FOR INPUT CHANNEL REFERENCED TO GROUND
      DO 130 I=1,MAXIP
      X2(I)=X1(I)-X1(1)
      Y2(I)=Y1(I)-Y1(1)
      Z2(I)=Z1(I)-Z1(1)
  130 CONTINUE
      XSTEP=(XMAX-XMIN)/6.0
      ZSTEP=(ZMAX-ZMIN)/9.0
      KASE(1)=CASE(1)
      CALL TITLE(KASE,100,
     *           'EAST$',100,
     *           'ATTITUDE$',100,
     *           6.0,9.0)
      CALL GRAF(XMIN,XSTEP,XMAX,ZMIN,ZSTEP,ZMAX)
      CALL SCLPIC(0.5)
      CALL FRAME
      CALL GRID(2,2)
      CALL CURVE(X2,Z2,MAXIP,MARK)
      CALL ENDPL(0)
      CALL TITLE(KASE,100,
     *           'NORTH$',100,
     *           'ATTITUDE$',100,
     *           6.0,9.0)
      CALL GRAF(XMIN,XSTEP,XMAX,ZMIN,ZSTEP,ZMAX)
      CALL FRAME
      CALL SCLPIC(0.5)
      CALL GRID(2,2)
      CALL CURVE(Y2,Z2,MAXIP,MARK)
```

```
      CALL ENDPL(0)
      CALL TITLE(KASE,100,
     *           'NORTH$',100,
     *           'EAST$',100,
     *           6.0,6.0)
      CALL GRAF(XMIN,XSTEP,XMAX,XMIN,XSTEP,XMAX)
      CALL FRAME
      CALL SCLPIC(0.5)
      CALL GRID(2,2)
      CALL CURVE(X2,Y2,MAXIP,MARK)
      CALL ENDPL(0)
  299 CONTINUE
C*****CHECK THE POSSIBILITY OF USING EXP DATA BANK TO SAVE TIME
      IDB=1
      TEXM=C4*TPULSE
      IF(TEXM.GE.174) IDB=0
      IF(IDB.EQ.0) GO TO 3952
C*****CALCULATE ECON(L) FOR EXPONENTIAL MODIFICATION IN SUBSEQUENT
C*****USE OF THE CURRENT MODEL DATA IN EACH TIME STEPS
      EDELTA=DEXP(C3*DELT)
      EDELTB=DEXP(C4*DELT)
      EDELTD=DEXP(C5*DELT)
      EDELTE=DEXP(C6*DELT)
      WRITE(6,115) NT,DELT,EDELTA,EDELTB,EDELTD,EDELTE
  115 FORMAT(1H0,'******TIME STEP MULTIPLIER IN CURRENT MODEL******',/
     *I12,' NT=TOTAL NUMBER OF TIME STEPS USED',/
     *1PD12.5,' DELT=TIME STEP INCREMENT',/
     *1PD12.5,' EDELTA=MULTIPLIER FOR AR(I) AND AI(I)',/
     *1PD12.5,' EDELTB=MULTIPLIER FOR BR(I) AND BI(I)',/
     *1PD12.5,' EDELTD=MULTIPLIER FOR DR(I) AND DI(I)',/
     *1PD12.5,' EDELTE=MULTIPLIER FOR ER(I) AND EI(I)',/
     *///,2X,'L     K',6X,'ECONA',7X,'ECONB',6X,'ECOND',7X,'ECONE',/)
      IF(IBUG.EQ.0) WRITE(6,1599)
 1599 FORMAT(1H0,'***** DEBUG PRINT OUT CAN BE TURNED ON BY SETTING',
     *' IBUG=1 *****',/)
      DO 200 L=1,NT
      K=NT-L
      ECONA(L)=EDELTA**K
      ECONB(L)=EDELTB**K
C*****ECOND(L) AND ECONE(L) ARE NOT NEEDED IN CORONA CURRENT EVALUATIONS
      ECOND(L)=0.D0
      ECONE(L)=0.D0
      IF(IBUG.EQ.1) WRITE(6,195) L,K,ECONA(L),ECONB(L),ECOND(L),ECONE(L)
  195 FORMAT(1H ,2I5,4(1PD12.5))
  200 CONTINUE
 3952 CONTINUE
C*****CALCULATE ELECTRIC FIELDS
      CALL EFIELD(EZ,FX,FY,FZ,DXYZ,CASE,ISCA)
C*****CHECK TO SEE THIS IS THE FINAL CASE TO BE ANALYZED
      READ(5,389) LAST
  389 FORMAT(I5)
```

```
      IF(LAST.EQ.1) GO TO 399
      GO TO 11111
  399 CONTINUE
      CALL DONEPL
      CALL EXIT
      STOP
      END
      SUBROUTINE CURCUI(RCHAN,RIMAGE)
      IMPLICIT REAL*8(A-H,O-Z)
      REAL*8 LT
      DIMENSION RCHAN(6500),RIMAGE(6500),AR(6500),BR(6500),DR(6500),
     *ER(6500),AI(6500),BI(6500),DI(6500),EI(6500),LT(6500),
     *X(6500),Y(6500),Z(6500)
      COMMON/CHANEL/X,Y,Z,LT,DLI,FZO,MAX,LIN,KNT,IBUG,ICUR,IDB
      COMMON/FLASH/DELT,TPULSE,RFG,TMAX,NT,IRTD,K1,K2,K3
      COMMON/SPEED/V,C
      COMMON/CONSTS/C1,C2,C3,C4,C5,C6,C7,C8,TPC,IPZH
      COMMON/BANKS/AR,BR,DR,ER,AI,BI,DI,EI
C*****CALCULATE CUR AND CUI AT TIME=TMAX FOR ALL SEGMENTS(REAL AND
C*****IMAGE) AND STORE THEM AS CURRENT MODEL DATA BANK FOR LATER USE
C*****THIS WAY SAVE THE COMPUTING TIME FOR EVALUATING EXPONENTIALS
C*****BOTH TCHAN AND TIMAG ARE CALCULATED FOR BREAKDOWN PULSE TIME
C*****AS REFERENCE,THE CORONA CURRENT AT (Z,T) IS EVALUATED  AT
C*****THIS TIME FRAME IN SUBROUTINE CORONA
      WRITE(6,15) MAX,TPULSE,TMAX,LT(MAX)
   15 FORMAT(1H0,'**********LEVINE CURRENT MODEL DATA BANK******',/
     *I12,' MAX=TOTAL NUMBER OF CHANNEL SEGMENTS',/
     *1PD12.5,' TPULSE=TOTAL TIME OF CURRENT PULSE ANALIZED',/
     *1PD12.5,' TMAX=MAX SOURCE TIME IN CURRENT MODEL CALCULATED',/
     *1PD12.5,' LT(MAX)=TOTAL CHANNEL LENGTH USED',/
     *///,5X,'I',4X,'TCHAN',7X,'TIMAGE',9X,'AR',10X,'BR',10X,'DR',
     *10X,'ER',10X,'AI',10X,'BI',10X,'DI',10X,'EI',/)
      IF(IBUG.EQ.0) WRITE(6,1599)
 1599 FORMAT(1H0,'***** DEBUG PRINT OUT CAN BE TURNED ON BY SETTING',
     *' IBUG=1 *****',/)
      DV1=1.D0/V
      DC1=1.D0/C
      TCHAN1=TMAX
      TIMAG1=TMAX
      DO 100 I=2,MAX
      I1=I-1
      TCHAN2=TMAX-LT(I)*DV1+(RFG-RCHAN(I))*DC1
      IF(IRTD.EQ.0) TCHAN2=TMAX-LT(I)*DV1-RCHAN(I)*DC1
      TCHAN=(TCHAN1+TCHAN2)*0.5D0
      T=TCHAN
      IF(T.LT.0.D0.OR.T.GT.TMAX) GO TO 20
      AR(I1)=DEXP(-C3*T)
      BR(I1)=DEXP(-C4*T)
C*****ER(I1) AND DR(I1) ARE NOT USED IN CORONA CURRENT EVALUATION
      DR(I1)=0.D0
      ER(I1)=0.D0
```

```
      GO TO 25
   20 CONTINUE
      AR(I1)=0.D0
      BR(I1)=0.D0
      DR(I1)=0.D0
      ER(I1)=0.D0
   25 CONTINUE
      TIMAG2=TMAX-LT(I)*DV1+(RFG-RIMAGE(I))*DC1
      IF(IRTD.EQ.0) TIMAG2=TMAX-LT(I)*DV1-RIMAGE(I)*DC1
      TIMAG=(TIMAG1+TIMAG2)*0.5D0
      T=TIMAG
      IF(T.LT.0.D0.OR.T.GT.TMAX) GO TO 30
      AI(I1)=DEXP(-C3*T)
      BI(I1)=DEXP(-C4*T)
C*****EI(I1) AND DI(I1) ARE NOT USED IN CORONA CURRENT EVALUATION
      DI(I1)=0.D0
      EI(I1)=0.D0
      GO TO 35
   30 CONTINUE
      AI(I1)=0.D0
      BI(I1)=0.D0
      DI(I1)=0.D0
      EI(I1)=0.D0
   35 CONTINUE
      IF(IBUG.EQ.1) WRITE(6,50) I,TCHAN,TIMAG,AR(I1),BR(I1),DR(I1),
     *ER(I1),AI(I1),BI(I1),DI(I1),EI(I1)
   50 FORMAT(1H ,I5,10(1PD12.5))
      TCHAN1=TCHAN2
      TIMAG1=TIMAG2
  100 CONTINUE
  110 CONTINUE
      RETURN
      END
      SUBROUTINE ASET(ARRAY,FX,FY,FZ,KEY,ADIR)
      IMPLICIT REAL*8(A-H,O-Z)
      REAL*8 ARRAY,FX,FY,FZ,KEY,XKEY,YKEY,ZKEY,LT
      DIMENSION RCHAN(6500),RIMAGE(6500),ARRAY(1200),X(6500),Y(6500),
     *Z(6500),LT(6500),AR(6500),BR(6500),DR(6500),ER(6500),AI(6500),
     *BI(6500),DI(6500),EI(6500),ECONA(1200),ECONB(1200),ECOND(1200),
     *ECONE(1200),KTR(1200),KTI(1200)
      COMMON/CHANEL/X,Y,Z,LT,DLI,FZO,MAX,LIN,KNT,IBUG,ICUR,IDB
      COMMON/FLASH/DELT,TPULSE,RFG,TMAX,NT,IRTD,K1,K2,K3
      COMMON/SPEED/V,C
      COMMON/CONSTS/C1,C2,C3,C4,C5,C6,C7,C8,TPC,IPZH
      COMMON/BANKS/AR,BR,DR,ER,AI,BI,DI,EI
      COMMON/ECONS/ECONA,ECONB,ECOND,ECONE
      DATA XKEY/1HX/,YKEY/1HY/,ZKEY/1HZ/
C*****IF LIN=1 FOR STRAIGHT LINE CHANNEL,THE VECTOR POTENTIAL AX AND
C*****AY RAE ZERO. THEN BYPASS ASET ROUTINE
      IF(LIN.EQ.1.AND.KEY.EQ.XKEY) GO TO 444
      IF(LIN.EQ.1.AND.KEY.EQ.YKEY) GO TO 444
```

```
      WRITE(6,5) ADIR,FX,FY,FZ
    5 FORMAT(1H0,25X,'******',A3,' AT ( ',3F12.2,' ) ******',//)
C*****WRITE CURRENTS AT CHANNEL SEGMENT MAXHO CORESPONDING TO C8
      MAXHO=C8/DLI
      DO 10 I=1,MAX
      RCHAN(I)=DSQRT((FX-X(I))**2+(FY-Y(I))**2+(FZ-Z(I))**2)
      RIMAGE(I)=DSQRT((FX-X(I))**2+(FY-Y(I))**2+(FZ+Z(I))**2)
   10 CONTINUE
C*****WRITE CHANNEL SEGMENTS TO FIELD POINT DISTANCES
      WRITE(6,22)
   22 FORMAT(1H0,3(3X,'I',8X,'RCHAN',10X,'RIMAGE      '),/)
      IF(IBUG.EQ.1) WRITE(6,33) (I,RCHAN(I),RIMAGE(I),I=1,MAX)
   33 FORMAT(3(I5,1X,2(1PD16.10,1X)))
      IF(IBUG.EQ.0) WRITE(6,1599)
 1599 FORMAT(1H0,'***** DEBUG PRINT OUT CAN BE TURNED ON BY SETTING',
     *' IBUG=1 *****',/)
      TMAX=TPULSE
      IF(IDB.EQ.0) GO TO 1806
C*****CALL CURCUI TO EVALUATE CURRENT MODEL DATA BANK AT TMAX
C*****THIS DATA BANK CAN BE USED FOR LATER CURRENT VALUES AT BOTH
C*****REAL AND IMAGE CHANNEL SEGMENTS IN SUBSEQUENT TIME STEPS
C*****CALCULATE TMAX FOR CURRENT MODEL DATA BANK AT TMAX AT FIELD
C*****POINT OF INTEREST USING GROUND RFG AS REFERENCE TO CALCULATE TIME
C*****TMAX IS THE MAX TIME IN CURRENT EVALUATION SUCH THAT THE RADIATION
C*****EMITTED THEN WILL BE DETECTED AT FIELD POINT AT TPULSE SEC
      CALL CURCUI(RCHAN,RIMAGE)
 1806 CONTINUE
C*****EXESSIVE OUTPUTS FOR DEBUG RUN ONLY OTHERWISE SET KNT=0
      IF(KNT.NE.1.AND.KEY.EQ.ZKEY) WRITE(6,316)
  316 FORMAT(1H0,20X,'***** CURRENT DISTRIBUTION FOR DEBUG ONLY*****',
     *//,' TIME',' CHAN',6X,'TCHAN',10X,'TIMAGE',9X,
     *'RCHAN',10X,'RIMAGE',9X,'REAL I',8X,'IMAGE I',
     *7X,'SUM FOR A',9X,'TIME',/1H0,'***** DEBUG PRINT OUT CAN BE',
     *' TURNED ON BY SETTING KNT=1 AND ZKEY=Z *****',/)
      DO 100 K=1,NT
      L=NT-K+1
      IZR=0
      IZI=0
      KTR(L)=0
      KTI(L)=0
      IF(KNT.EQ.1.AND.KEY.EQ.ZKEY) WRITE(6,31)
   31 FORMAT(1H0,20X,'***** CURRENT DISTRIBUTION FOR DEBUG ONLY*****',
     *//,' TIME',' CHAN',6X,'TCHAN',10X,'TIMAGE',9X,
     *'RCHAN',10X,'RIMAGE',9X,'REAL I',8X,'IMAGE I',
     *7X,'SUM FOR A',9X,'TIME',/)
      SUM=0.D0
      FK=DFLOAT(K-1)
      TIME=TMAX-FK*DELT
      TCHAN1=TIME
      TIMAG1=TIME
      CORZ1=1.0D0
```

```
      IUR=0
      IUI=0
      DO 140 I=2,MAX
C*****CALCULATE BREAKDOWN CURRENT DECAY FACTOR CORZ IN LIN MODEL
      CORZ2=DEXP(-LT(I)/C8)
      I1=I-1
C*****TCHAN AND TIMAGE ARE TIMES TO BE USED IN CURRENT MODEL
C*****ACCORDING TO LEVINE THE RETARDED TIME RO/C CAN BE USED
C*****THIS WILL CAUSE THE OBSERVED FIELD CHANGES NOT TO LAG BEHIND
C*****WHICH IS EQUIVALENT TO  SHIFTING TIME ORIGIN BY RO/C
      DV1=1.DO/V
      DC1=1.DO/C
      IF(IRTD.EQ.1) GO TO 321
      TCHAN2=TIME-LT(I)*DV1-RCHAN(I)*DC1
      TIMAG2=TIME-LT(I)*DV1-RIMAGE(I)*DC1
      GO TO 123
C*****IF RETARDED TIME IS REGUIRED THEN USE THE FOLLOWING STATEMENTS
  321 CONTINUE
      TCHAN2=TIME-LT(I)*DV1+(RFG-RCHAN(I))*DC1
      TIMAG2=TIME-LT(I)*DV1+(RFG-RIMAGE(I))*DC1
  123 CONTINUE
      CORZB=(CORZ1+CORZ2)*0.5DO
C*****TCHAN AND TIMAG ARE TIME VARIABLES USED IN EVALUATING BREAKDOWN
C*****PULSE CURRENTS
      TCHAN=(TCHAN1+TCHAN2)*0.5DO
      TIMAG=(TIMAG1+TIMAG2)*0.5DO
C*****CHECK TIME TO INITIATE UNIFORM CURRENT
      IF(I.GT.2) GO TO 138
      IF(TCHAN.GT.0.DO) IUR=1
      IF(TIMAG.GT.0.DO) IUI=1
  138 CONTINUE
      RCHANI=(RCHAN(I)+RCHAN(I1))*0.5DO
      RIMAGI=(RIMAGE(I)+RIMAGE(I1))*0.5DO
C*****USE AND/OR IN THE FOLLOWING TEST FOR MATCHING CONTRIBUTIONS
C*****FROM REAL AND IMAGE CHANNEL(NO/YES)
      IF(TCHAN.LT.0.DO.AND.TIMAG.LT.0.DO) GO TO 40
      IF(TCHAN.GT.TIME.AND.TIMAG.GT.TIME) GO TO 40
C*****CALCULATE CURRENT ON CHANNEL SEGMENT DLI
      IF(TCHAN.LT.0.DO.OR.(TCHAN.GT.TIME)) GO TO 36
      KTR(L)=KTR(L)+1
      IF(IDB.EQ.0) GO TO 3581
      CURLB=C1*(AR(I1)*ECONA(L)-BR(I1)*ECONB(L))
      GO TO 3583
 3581 CONTINUE
      TMIN=C4*TCHAN
      IF(TMIN.GE.180.0) GO TO 3582
      CURLB=C1*(DEXP(-C3*TCHAN)-DEXP(-C4*TCHAN))
      GO TO 3583
 3582 CURLB=C1*DEXP(-C3*TCHAN)
 3583 CONTINUE
      IF(IPZH.EQ.1) CURLB=CURLB*CORZB
```

```
C*****CALCULATE CORONA CURRENT ACCORDING TO LIN'S MODEL
      ZC=LT(I)
      ZH=LT(MAX)
C*****USE CORRECTED TIME FOR CORONA CURRENT
      ZCOV=(LT(I)+LT(I1))*DV1*0.5D0
      TCORR=TCHAN+ZCOV
      CALL CORONA(TCORR,ZC,ZH,CUR,I)
      CURC=CUR
      GO TO 38
   36 CONTINUE
      CURLB=0.D0
      CURC=0.D0
   38 CONTINUE
      IF(TIMAG.LT.0.D0.OR.(TIMAG.GT.TIME)) GO TO 37
      KTI(L)=KTI(L)+1
      IF(IDB.EQ.0) GO TO 4581
      CUILB=C1*(AI(I1)*ECONA(L)-BI(I1)*ECONB(L))
      GO TO 4583
 4581 CONTINUE
      TMIN=C4*TIMAG
      IF(TMIN.GE.180.0) GO TO 4582
      CUILB=C1*(DEXP(-C3*TIMAG)-DEXP(-C4*TIMAG))
      GO TO 4583
 4582 CUILB=C1*DEXP(-C3*TIMAG)
 4583 CONTINUE
C*****WRITE FOR DEBUG
      IF(IBUG.EQ.1)WRITE(6,3638)L,I,AR(I1),AI(I1),BR(I1),BI(I1),CUILB,
     *CURLB
 3638 FORMAT(1H ,2I5,6(1PE12.5))
      IF(IPZH.EQ.1) CUILB=CUILB*CORZB
C*****CALCULATE CORONA CURRENT ACCORDING TO LIN'S MODEL
      ZC=LT(I)
      ZH=LT(MAX)
C*****USE CORRECTED TIME FOR CORONA CURRENT
      ZCOV=(LT(I)+LT(I1))*DV1*0.5D0
      TCORI=TIMAG+ZCOV
      CALL CORONA(TCORI,ZC,ZH,CUR,I)
      CUIC=CUR
      GO TO 39
   37 CONTINUE
      CUILB=0.D0
   39 CONTINUE
C*****CHECK CURLB AND CUILB FOR POSITIVE VALUES
      IF(CURLB.GT.0.D0) GO TO 5005
      CURLB=0.D0
      KTR(L)=KTR(L)-1
      IZR=IZR+1
      IF(IBUG.EQ.1) WRITE(6,5007) L,IZR,KTR(L),KTI(L)
 5007 FORMAT(4I5,' ****** CURLB=0.0 SENSED ******')
 5005 CONTINUE
      IF(CUILB.GT.0.D0) GO TO 5095
```

```
      CUILB=0.D0
      KTI(L)=KTI(L)-1
      IZI=IZI+1
      IF(IBUG.EQ.1) WRITE(6,5008) L,IZI,KTR(L),KTI(L)
 5008 FORMAT(4I5,' ****** CUILB=0.0 SENSED ******')
 5095 CONTINUE
      GO TO 3302
   40 CONTINUE
C*****BOTH IB AND IC ARE ABSENT, ONLY IU EXISTS ON CHANNEL
      CURLB=0.D0
      CUILB=0.D0
      CURC=0.D0
      CUIC=0.D0
 3302 CONTINUE
C*****UNIFORM CURRENT SHOULD BE ADDED AT TIME WHEN BREAKDOWN STARTED
C*****CHECK RFG AND ACTUAL BREAKDOWN TIME AND IRTD FOR CONSISTENCY
      CURU=C7
      IF(IUR.EQ.0.AND.IUI.EQ.0) CURU=0.D0
      CUIU=C7
      IF(IUR.EQ.0.AND.IUI.EQ.0) CUIU=0.D0
      IF(KEY.EQ.XKEY) DCHAN=X(I)-X(I-1)
      IF(KEY.EQ.YKEY) DCHAN=Y(I)-Y(I-1)
      IF(KEY.EQ.ZKEY) DCHAN=Z(I)-Z(I-1)
      DIMAGE=DCHAN
      IF(KEY.EQ.ZKEY) DIMAGE=-DCHAN
C*****ADDING THREE COMPONENTS CURRENT TO GET TOTAL VALUE
      CURL=CURLB+CURC+CURU
      CUIL=CUILB+CUIC+CUIU
      SUM=SUM+CURL*DCHAN/RCHANI-CUIL*DIMAGE/RIMAGI
C*****WRITE CURRENT COMPONENT FOR PLOTTING AND DEBUGGING
      IF(KEY.NE.ZKEY.AND.FZ.NE.FZO) GO TO 3334
      LTIC=LT(I)/DLI
      IF(ICUR.EQ.1.AND.LTIC.EQ.2) GO TO 3323
      GO TO 3331
 3323 CONTINUE
      WRITE(16,3327) L,I,TIME,CURLB,CURC,CURU
 3327 FORMAT(1H ,2I5,4(1PE11.4))
 3331 IF(ICUR.EQ.1.AND.LTIC.EQ.MAXHO) GO TO 3338
      GO TO 3334
 3338 CONTINUE
      WRITE(26,3327) L,I,TIME,CURLB,CURC,CURU
 3334 CONTINUE
C*****WRITE CHANNEL CURRENT DISTRIBUTION FOR EACH TIME STEP FOR DEBUG
      IF(KNT.NE.1) GO TO 314
C     IF(KEY.EQ.ZKEY.AND.(L.EQ.K1.OR.L.EQ.K2.OR.L.EQ.K3.OR.L.EQ.NT))
      WRITE(6,35)L,I,TCHAN,TIMAGE,RCHAN(I),RIMAGE(I),CURL,CUIL,SUM,TIME
   35 FORMAT(2I5,8(3X,1PD12.5))
  314 CONTINUE
      CORZ1=CORZ2
      TCHAN1=TCHAN2
      TIMAG1=TIMAG2
```

```
  140 CONTINUE
   50 ARRAY(L)=0.0000001D0*SUM
      IF(KTR(L).NE.KTI(L).AND.IBUG.EQ.1) WRITE(6,4345) L,KTR(L),KTI(L)
 4345 FORMAT(1H ,3I5,'****KTR(L) NOT EQUAL TO KTI(L)****')
  100 CONTINUE
C*****WRITE VECTOR POTENTIAL ARRAY
      WRITE(6,443) ADIR,FX,FY,FZ
  443 FORMAT(1H0,25X,'******',A3,' AT ( ',3F12.2,' ) ******',//,
     *3('  L    KTR    KTI            ARRAY         '),/)
      IF(IBUG.EQ.0) WRITE(6,1599)
      IF(IBUG.EQ.1) WRITE(6,120) (L,KTR(L),KTI(L),ARRAY(L),L=1,NT)
  120 FORMAT(3(3I5,1X,1PD20.13))
      GO TO 565
  444 CONTINUE
      WRITE(6,5) ADIR,FX,FY,FZ
      WRITE(6,446)
  446 FORMAT(1H ,'****** LINEAR CHANNEL AX(I)=AY(I)=0.0 *****')
      DO 555 L=1,NT
      ARRAY(L)=0.D0
  555 CONTINUE
  565 CONTINUE
      KNT=0
      RETURN
      END
      SUBROUTINE CORONA(TIME,Z,H,CUR,I)
      IMPLICIT REAL*8(A-H,O-Z)
      COMMON/FLASH/DELT,TPULSE,RFG,TMAX,NT,IRTD,K1,K2,K3
      COMMON/CONSTS/C1,C2,C3,C4,C5,C6,C7,C8,TPC,IPZH
      COMMON/SPEED/V,C
      AD=C5/V+C5/C-1.0/C8
      BD=C6/V+C6/C-1.0/C8
      IF(TIME.LT.0.D0) GO TO 71
      TD=TIME-TPC+Z/C
      ZM=TD/(1.0/V+1.0/C)
      IF(ZM.LE.Z) GO TO 66
      IF(ZM.GE.H) ZM=H
      COR1=C2*(DEXP(AD*ZM-C5*TD)-DEXP(AD*Z-C5*TD))/AD
      COR2=C2*(DEXP(BD*ZM-C6*TD)-DEXP(BD*Z-C6*TD))/BD
      GO TO 69
   66 CONTINUE
      COR1=0.0
      COR2=0.0
   69 CONTINUE
      CUR=COR1-COR2
      IF(CUR.LT.0.D0) CUR=0.D0
      GO TO 77
   71 CONTINUE
      CUR=0.0
   77 CONTINUE
      RETURN
      END
```

```
      SUBROUTINE PHISET(FZO,PHI,FX,FY,FZ,DXYZ)
      IMPLICIT REAL*8(A-H,O-Z)
      REAL*8 PHI,FX,FY,FZ,XKEY,YKEY,ZKEY,LT
      DIMENSION PHI(1200),AXP(1200),AXM(1200),AYP(1200),AYM(1200),
     *AZP(1200),AZM(1200),X(6500),Y(6500),Z(6500),LT(6500),TIME(1200),
     *AZ(1200)
      COMMON/CHANEL/X,Y,Z,LT,DLI,FZO,MAX,LIN,KNT,IBUG,ICUR,IDB
      COMMON/FLASH/DELT,TPULSE,RFG,TMAX,NT,IRTD,K1,K2,K3
      COMMON/SPEED/V,C,AZ
      DATA XKEY/1HX/,YKEY/1HY/,ZKEY/1HZ/
      DATA HAXP/3HAXP/,HAXM/3HAXM/,HAYP/3HAYP/,HAYM/3HAYM/,
     *     HAZP/3HAZP/,HAZM/3HAZM/
C*****IF FZ=0.0 I.E. ON THE GROUND, THE POTENTIAL IS ALWAYS ZERO.
C*****IF THE CHANNEL IS LINEAR AND FZ NOT 0.0, ONLY PHIZ IS NOT ZERO.
      FXP=FX+DXYZ
      FXM=FX-DXYZ
      FYP=FY+DXYZ
      FYM=FY-DXYZ
      FZP=FZ+DXYZ
      FZM=FZ-DXYZ
      IF(FZ.EQ.0.D0) GO TO 355
      IF(FZ.NE.0.D0.AND.LIN.EQ.1) GO TO 35
      GO TO 95
   35 CONTINUE
      DO 93 I=1,NT
      AXP(I)=0.D0
      AXM(I)=0.D0
      AYP(I)=0.D0
      AYM(I)=0.D0
   93 CONTINUE
      IF(FZP.EQ.FZO) GO TO 661
      CALL ASET(AZP,FX,FY,FZP,ZKEY,HAZP)
      GO TO 671
  661 CONTINUE
      CALL AZPM(AZP,FX,FY,FZP,HAZP)
  671 CONTINUE
      IF(FZM.EQ.FZO) GO TO 681
      CALL ASET(AZM,FX,FY,FZM,ZKEY,HAZM)
      GO TO 691
  681 CONTINUE
      CALL AZPM(AZM,FX,FY,FZM,HAZM)
  691 CONTINUE
      GO TO 99
   95 CONTINUE
      CALL ASET(AXP,FXP,FY,FZ,XKEY,HAXP)
      CALL ASET(AXM,FXM,FY,FZ,XKEY,HAXM)
      CALL ASET(AYP,FX,FYP,FZ,YKEY,HAYP)
      CALL ASET(AYM,FX,FYM,FZ,YKEY,HAYM)
      IF(FZP.EQ.FZO) GO TO 663
      CALL ASET(AZP,FX,FY,FZP,ZKEY,HAZP)
      GO TO 673
```

```
  663 CONTINUE
      CALL AZPM(AZP,FX,FY,FZP,HAZP)
  673 CONTINUE
      IF(FZM.EQ.FZO) GO TO 683
      CALL ASET(AZM,FX,FY,FZM,ZKEY,HAZM)
      GO TO 693
  683 CONTINUE
      CALL AZPM(AZM,FX,FY,FZM,HAZM)
  693 CONTINUE
   99 CONTINUE
      CTD2=C*C*DELT/(2.D0*DXYZ)
      AP1=AXP(1)+AYP(1)+AZP(1)
      AM1=AXM(1)+AYM(1)+AZM(1)
      DIA1=AP1-AM1
      IF(AP1.EQ.0.D0.OR.AM1.EQ.0.D0) DIA1=0.D0
      PHI(1)=-CTD2*DIA1*0.5D0
      DO 100 I=2,NT
      API=AXP(I)+AYP(I)+AZP(I)
      AMI=AXM(I)+AYM(I)+AZM(I)
      DIAI=API-AMI
      IF(API.EQ.0.D0.OR.AMI.EQ.0.D0) DIAI=0.D0
      PHI(I)=PHI(I-1)-CTD2*(DIAI+DIA1)*0.5D0
      DIA1=DIAI
  100 CONTINUE
C*****WRITE SCALAR POTENTIAL PHI
      WRITE(6,110) FX,FY,FZ
  110 FORMAT(1H1,20X,'****** POTENTIAL PHI AT (',3F12.2,' )******',
     *//,3X,'L',10X,'AXP',14X,'AXM',14X,'AYP',14X,'AYM',
     *11X,'AZP',14X,'AZM',14X,'PHI',/)
      DO 155 L=1,NT
      WRITE(6,120) L,AXP(L),AXM(L),AYP(L),AYM(L),AZP(L),AZM(L),
     *PHI(L)
  120 FORMAT(I5,7(1X,1PD16.9))
  155 CONTINUE
      GO TO 665
  355 CONTINUE
      WRITE(6,357) FX,FY,FZ
  357 FORMAT(1H0,'******POTENTIAL PHI AT (',3F12.2,' )*****',
     */,'  PHI(I)=0.0 AT FZ=0.0 BY BOUNDARY CONDITION')
      DO 455 L=1,NT
      PHI(I)=0.D0
  455 CONTINUE
  665 CONTINUE
      RETURN
      END
      SUBROUTINE AZPM(AZO,FX,FY,FZ,ADIR)
      IMPLICIT REAL*8(A-H,O-Z)
      DIMENSION AZO(1200),AZ(1200)
      COMMON/FLASH/DELT,TPULSE,RFG,TMAX,NT,IRTD,K1,K2,K3
      COMMON/SPEED/V,C,AZ
C*****THIS SUBROUTINE ASSIGN AZ(L) VALUES TO EITHER AZP(L) OR AZM(L)
```

```
C*****WHENEVER THE FIELD POINTS ARE THE SAME (FX,FY,FZ)
      WRITE(6,443) ADIR,FX,FY,FZ
  443 FORMAT(1H0,25X,'******',A3,' AT ( ',3F12.2,' ) ******',/)
      WRITE(6,15)
   15 FORMAT(1H0,'****** SUBROUTINE AZPM HAS BEEN CALLED TO ',
     *'ASSIGN AZ(L) TO AZP(L) OR AZM(L) ******',/)
      DO 100 L=1,NT
      AZO(L)=AZ(L)
  100 CONTINUE
      RETURN
      END
      SUBROUTINE EFIELD(E,FX,FY,FZ,DXYZ,CASE,ISCA)
      IMPLICIT REAL*8(A-H,O-Z)
      REAL*8 FX,FY,ZKEY,LT
      REAL*8 LABEL,CASE,KASE
      REAL*4 TIME,YS,YR,YT
      DIMENSION E(1200),PHIP(1200),PHIM(1200),AZ(1200),X(6500),Y(6500),
     *Z(6500),LT(6500),STAE(1200),RADE(1200),TIME(1200),YS(1200),
     *YR(1200),YT(1200),CASE(10),LABEL(8),KASE(10),IPAK(150)
      COMMON/CHANEL/X,Y,Z,LT,DLI,FZO,MAX,LIN,KNT,IBUG,ICUR,IDB
      COMMON/FLASH/DELT,TPULSE,RFG,TMAX,NT,IRTD,K1,K2,K3
      COMMON/SPEED/V,C,AZ
      COMMON/PLOT/TMAXP,EMIN,EMAX,MARK
      DATA ZKEY/1HZ/,HAZO/3HAZO/
      KASE(1)=CASE(1)
      KASE(2)=CASE(2)
      KASE(3)=CASE(3)
      KASE(4)=CASE(4)
      KASE(5)=CASE(5)
      KASE(6)=CASE(6)
      KASE(7)=CASE(7)
      KASE(9)=CASE(9)
      KASE(8)=CASE(8)
      FZO=FZ
      FZP=FZ+DXYZ
      FZM=FZ-DXYZ
      CALL ASET(AZ,FX,FY,FZ,ZKEY,HAZO)
      CALL PHISET(FZO,PHIP,FX,FY,FZP,DXYZ)
      IF(FZ.EQ.0.D0) GO TO 1555
      CALL PHISET(FZO,PHIM,FX,FY,FZM,DXYZ)
      GO TO 1665
 1555 CONTINUE
      DO 1650 I=1,NT
      PHIM(I)=-PHIP(I)
 1650 CONTINUE
 1665 CONTINUE
      DXYZ2=0.5D0/DXYZ
      DELT2=0.5D0/DELT
      STAE(1)=-(PHIP(1)-PHIM(1))*DXYZ2
      IF(PHIP(1).EQ.0.D0.OR.PHIM(1).EQ.0.D0) STAE(1)=0.D0
      RADE(1)=-(AZ(2)-AZ(1))/DELT
```

```
      IF(AZ(1).EQ.0.DO.OR.AZ(2).EQ.0.DO) RADE(1)=0.DO
      E(1)=STAE(1)+RADE(1)
C*****NT1 IS THE MAX TIME STEP WHERE FILED CHANGES CAN BE EVALUATED
C*****DUE TO THE CENTRAL DIFFERENCE FOR TIME DERIVATIVE OF PHI
      NT1=NT-1
      DO 100 I=2,NT1
      I1=I-1
      I2=I+1
C*****STAE IS STATIC FIELD AND RADE IS THE RADIATION FILED
      STAE(I)=-(PHIP(I)-PHIM(I))*DXYZ2
      IF(PHIP(I).EQ.0.DO.OR.PHIM(I).EQ.0.DO) STAE(I)=0.DO
      RADE(I)=-(AZ(I2)-AZ(I1))*DELT2
      IF(AZ(I).NE.0.DO.AND.AZ(I2).NE.0.DO.AND.AZ(I1).EQ.0.DO) RADE(I)
     *=-(AZ(I2)-AZ(I))*DELT2*2.DO
      IF(AZ(I1).EQ.0.DO.AND.AZ(I).EQ.0.DO) RADE(I)=0.DO
      E(I)=STAE(I)+RADE(I)
  100 CONTINUE
C*****LAST POINT FOR PLOTTING PURPOSE
      E(NT)=E(NT-1)
      STAE(NT)=STAE(NT-1)
      RADE(NT)=RADE(NT-1)
C*****WRITE FIELD CHANGE E(I)
      WRITE(6,110) FX,FY,FZ
  110 FORMAT(1H1,25X,'******CALCULATED FIELDS AT (',3F12.2,' )*****',/)
      WRITE(6,111)
  111 FORMAT(1H0,'  L',9X,'PHIP',13X,'PHIM',13X,'STAE',13X,'RADE',
     *13X,' AZ',14X,' EZ',14X,'TIME',/)
C*****OUTPUT FINAL SOLUTION KEY PARAMETERS TO UNIT 8 ON WYLBUR
      WRITE(8,1821) (CASE(I),I=1,9)
 1821 FORMAT(9A8)
C*****FIND EMAX AND EMIN FOR FIELD PLOTS
      IF(ISCA.EQ.1) CALL MAXMIN(STAE,RADE,E,NT,EMAX,EMIN)
      WRITE(8,1305) NT,MARK,ISCA,EMIN,EMAX,TMAXP
 1305 FORMAT(3I5,3E8.2)
      WRITE(8,8)
    8 FORMAT(1H ,//,3X,'I',6X,'STAE',8X,'RADE',11X,'EZ',10X,'TIME')
      DO 50 I=1,NT
      TIME(I)=(I-1)*DELT
      WRITE(6,1) I,PHIP(I),PHIM(I),STAE(I),RADE(I),AZ(I),E(I),TIME(I)
    1 FORMAT(1X,I4,7(2X,1PE15.8))
      WRITE(8,3) I,STAE(I),RADE(I),E(I),TIME(I)
    3 FORMAT(1X,I3,4(1X,1PD12.5))
   50 CONTINUE
C*****START PLOT RADIATION FIELDS
      YR(1)=0.0
      YS(1)=0.0
      YT(1)=0.0
      DO 130 I=1,NT
      J=I+1
      TIME(I)=TIME(I)*1.0E6
      YS(J)=STAE(I)
```

```
      YR(J)=RADE(I)
      YT(J)=E(I)
  130 CONTINUE
      CALL TITLE(KASE,-100,
     *           'TIME IN MICRO SEC$',100,
     *           'ELECTRIC FIELD IN V/M$',100,
     *           8.0,5.0)
      TSTEP=(TMAXP/8.0)*1.0E6
      ESTEP=(EMAX-EMIN)/5.0
      CALL INTAXS
      CALL GRAPH(0.0,TSTEP,EMIN,ESTEP)
      CALL FRAME
      CALL BLNK1(6.3,7.90,0.2,1.2,2)
      CALL SCLPIC(0.5)
      CALL GRID(2,2)
      IDUMMY=LINEST(IPAK,150,80)
      CALL LINES('TOTAL$',IPAK,1)
      CALL LINES('DA/DT$',IPAK,2)
      CALL LINES('GRAD PHI$',IPAK,3)
      CALL CURVE(TIME,YT,NT,MARK)
      CALL CURVE(TIME,YR,NT,MARK)
      CALL CURVE(TIME,YS,NT,MARK)
      CALL RESET('BLNKS')
      CALL SCLPIC(1.0)
      CALL LEGEND(IPAK,3,6.4,0.3)
      CALL ENDPL(0)
      RETURN
      END
      SUBROUTINE MAXMIN(STAE,RADE,E,NT,EMAX,EMIN)
      IMPLICIT REAL*8(A-H,O-Z)
      DIMENSION STAE(1200),RADE(1200),E(1200)
C*****THIS SUBROUTINE FIND MAX AND MIN FIELD FOR SELF-SCALING PLOT
      STAE1=0.0
      STAE2=0.0
      RADE1=0.0
      RADE2=0.0
      E1=0.0
      E2=0.0
C*****FIND MAX AND MIN FOR SELF SCALING FILED PLOTS
      DO 50 I=1,NT
      IF(STAE(I).GE.STAE1) STAE1=STAE(I)
      IF(RADE(I).GE.RADE1) RADE1=RADE(I)
      IF(E(I).GE.E1) E1=E(I)
      IF(STAE(I).LT.STAE2) STAE2=STAE(I)
      IF(RADE(I).LT.RADE2) RADE2=RADE(I)
      IF(E(I).LT.E2) E2=E(I)
   50 CONTINUE
      EMAX=DMAX1(STAE1,RADE1,E1)
      EMAX=EMAX+4.9
      EMAX=IDINT(EMAX/5)*5
      EMIN=DMIN1(STAE2,RADE2,E2)
```

```
      EMIN=EMIN-4.9
      EMIN=IDINT(EMIN/5)*5
      WRITE(8,100) STAE1,RADE1,E1,EMAX,STAE2,RADE2,E2,EMIN
  100 FORMAT(1H ,'EMAX ',4E12.5,/1H ,'EMIN ',4E12.5)
      RETURN
      END
```

APPENDIX II

B. IBM JCL AND SAMPLE INPUT

```
//NSSLTHOR JOB USER=B32258,PASSWORD=LIAW,REGION=1250K,CLASS=W,
//          TIME=60
//*MAIN LINES=50,CARDS=999
//*MAIN ORG=ANLOS.PRO
//*       3   8      3   8      3   8      3   8      3   8
//*        2 5        2 5        2 5        2 5        2 5
//*     3 2 2 5 8  3 2 2 5 8  3 2 2 5 8  3 2 2 5 8  3 2 2 5 8
//*        2 5        2 5        2 5        2 5        2 5
//*       3   8      3   8      3   8      3   8      3   8
//* ***************************************************************
//* ***************************************************************
//* ****NSSLTHOR CALCULATES EZ FOR EXP.9 & EXP.10 THUNDER DATA*7/31/82*
//* ******USING MASTER'S BENCHMARK CURRENT FOR ZIGZAG CHANNELS*********
//* ******IMPROVED LIN'S CURRENT MODEL EVALUATING PROCEDURES***********
//* ***************************************************************
//* ***************************************************************
//*FORMAT PR,DDNAME=JESI0002,DEST=PRO
//*FORMAT PR,DDNAME=FT06F001,DEST=PRO
//*FORMAT PR,DDNAME=SYSMSG,DEST=PRO
//*FORMAT PU,DDNAME=STEP2.SYSUT2,DEST=ANLVM.B32258
//S1 EXEC FXECLG,OPTIONS='XREF',PRELIB='SYS1.DISLIB'
//SYSIN DD *
      (EMFIELD SOURCE DECK)
/*
//GO.FT08F001 DD DSN=B32258.NSSLTHOR.DFT08,UNIT=TSTEMP,DISP=(NEW,
//     CATLG),SPACE=(TRK,(15,5)),DCB=(RECFM=FB,LRECL=80,BLKSIZE=2960)
//GO.FT16F001 DD DSN=B32258.NSSLTHOR.DFT16,UNIT=TSTEMP,DISP=(NEW,
//     CATLG),SPACE=(TRK,(15,5)),DCB=(RECFM=FB,LRECL=80,BLKSIZE=2960)
//GO.FT26F001 DD DSN=B32258.NSSLTHOR.DFT26,UNIT=TSTEMP,DISP=(NEW,
//     CATLG),SPACE=(TRK,(15,5)),DCB=(RECFM=FB,LRECL=80,BLKSIZE=2960)
//GO.GRAPHICS DD PLOTTER=G1DATA,DSN=C116.B32258.NSSLTHOR.DG1DATA,
//        SPACE=(TRK,(30,5)),DISP=(NEW,CATLG),UNIT=TEMP
//GO.SYSIN DD *
NSSL.1 EXP.9 ZIGZAG  R=1KM V=C/3 DELT=.35US DL=2M DXYZ=10M$
   82  725   16    1    0    0    0    0    0    0    0    1    1    1
 2.50E+4 2.10E+1 3.20E+5 2.00E+6 1.00E+5 3.00E+6 0.50E+3 1.00E+8 1.50E+3
 1.57E+2 8.10E+1 0.00E+0 1.00E+1 0.20E+1 3.50E-7 4.80E-5
-3.60E+3 3.60E+3 0.00E+0 6.75E+3 5.60E-5-2.00E+3 0.40E+3    2    0
```

```
   0
 1 -436.32    1503.62   0.0
 2 -436.32    1503.62   893.83
 3 -482.89    1378.77   1053.00
 4 -930.94    2129.98   1158.50
 5 -1059.50   1887.85   1245.43
 6 -1338.99   -596.79   2261.18
 7 -1295.20   -399.66   2332.30
 8 -1026.97   -450.24   2452.59
 9 -541.22    -138.46   2844.22
10 -502.33    112.48    2952.61
11 -1470.84   61.21     3168.45
12 -1100.87   223.74    4154.4
13 -815.47    202.64    4528.06
14 -1410.86   322.97    5218.44
15 -989.42    228.50    5316.13
16 -1487.46   406.82    5712.43
   1
/*
//STEP2 EXEC SDSKVM,INDSN='C116.B32258.NSSLTHOR.DG1DATA'
//STEP3 EXEC POSTPLOT,INDSN='C116.B32258.NSSLTHOR.DG1DATA',
//   PLOTTER=VERS11,OPTIONS='PLOT(1-99)'
/* END OF FILE
```

APPENDIX II

C. FLOW CHART OF EMFIELD